The properties of antikaons in hot and dense matter

Laura Tolós Rigueiro

Departament d'Estructura i
Constituents de la Matèria
Universitat de Barcelona

The properties of antikaons in hot and dense matter

Memòria presentada per
Laura Tolós Rigueiro
per optar al títol de
Doctora en Ciències Físiques.

Barcelona, 2003.

Programa del Departament
d'Estructura i Constituents
de la Matèria. Bienni 98-00.
Universitat de Barcelona.

Directors de Tesi

Àngels Ramos Gómez.
Artur Polls Martí.

The properties of antikaons in hot and dense matter

L.Tolós

Departament d'Estructura i Constituents de la Matèria

Universitat de Barcelona, Maig 2003

A mi familia, mi fuerza interior

Contents

Agraïments

Una vegada acabada la feinada que suposa juntar tot el teu coneixement en una tesi, i amb la satisfacció d'una feina ben feta, és moment d'agrair l'ajut i la confiança de tots aquells que han estat al meu costat en els bons i els mals moments. Sense ells aquesta tesi de ben segur no hauria estat possible.

Voldria començar agraint als meus "jefes", Àngels i Artur, l'haver estat al meu costat ajudant-me i ensenyant-me com ha de ser una bona científica. Vull agrair a la meva "mamà " i "papà " científics l'ensenyar-me que la física i el ser persona no són termes oposats. Així mateix, una menció especial a l'Assum, la meva "germaneta" gran, amb qui he compartit rialles, gossips i moltes coses més, i a l'Isaac, mi "hermano" mayor, amante de la buena comida y del Camino de Santiago, y que a pesar de la distancia está siempre presente con su ironía y humor característicos. Gracies també al meu "germà petit", Jordi, per aguantar-me a mi i ser tan bon nano, i al meu nou germanet, l'Arnau, qui, juntament amb el Jordi, fan de l'oficina un lloc agradable per treballar-hi. Voldria també recordar a l'Agustí, l'abduit, el Manel, el cinèfil, els quals em van acollir i cuidar quan jo era una novata al grup, a la Muntsa, mamà dintre de poquet i a la Marta, l'Enric, la Dolors i d'altres companys del departament que ja han passat per l'aventura que suposa escriure una tesi.

También quisiera recordar a mis "amiguitos salmantinos", a quienes a pesar de la distancia y gracias al e-mail y las escapadas puedo calificar de buenos amigos. Salmantinos porque todo comenzó en mi primera salida a Salamanca y continuó con la escuela de Sevilla. Gracias a todos ellos por enseñarme que los físicos son también seres so-

ciables. Gracias a Cris, mi amiguita de Lepe, por ser tan echá palante y tan buena gente y a Fernandito, la marmota melillense y, como él se describe, majo por naturaleza. Gracias también a Javi, amigo de sus amigos y el madrileño más encantador que conozco y a Bruno, amante de las mujeres y de la buena física. Gracias a Rafa, el de Alcalá, dulce como pocos, a David, el madrileño reconvertido a francés y a la parejita de enamorados Maria y Santi. Gracias por los buenos ratos pasados y futuros que espero seguir disfrutando con vosotros.

Ahora llega el turno de mi gente más cercana, de recordar a mis "amigas del cole", una amistad que empezó hace ahora casi 10 años y que espero que dure otros 100 más: a Gema y Susi, mis coleguillas desde primero de BUP, con las que compartí entre resúmenes de libros de historia y trabajos diversos, muchos momentos inolvidables y a Sandrita y Anahí, amigas inseparables, con las cuales he disfrutado de la noche barcelonina en muchas ocasiones y con las cuales sé que puedo contar en todo momento. Gracias a todas por ser mis amigas y que sepais que podeis contar conmigo aún en la distancia. And last but not least I would also like to thank Robert for being close to me whenever I need him. Ich wünsche mir, dass wir immer gute Freunde bleiben.

Llegado este punto, es momento de recordar a mi familia que ha sido mi motor durante todos estos años y sin la cual no soy nadie. Voldria recordar la meva iaieta, Paquita, dona de gran caràcter a qui m'hagués agradat conèixer millor, a mi abuelita, Celsa, mujer fuerte de un inmenso corazón y lista como hay pocas y a mi yayo Antonio, hombre hecho a si mismo que lo haría todo por sus nietas. Y, sobretodo, quisiera decir unas palabras sobre lo más importante en mi vida, mis papis y mi hermanilla. A mi hermanilla, el pequeño monstruito, gracias por ser mi mejor amiga y por ser muchas veces mi hermana mayor aguantándome en mis momentos difíciles. Gracias a mi papi, per estar sempre amb mi i donar-me consells i estimar-me tant. Gracias a mi mami, por pasar noches conmigo repasando la lección, haciendo los mapas de sociales o los trabajos de pretecnología, gracias por estar siempre a mi lado. Gracias, en definitiva, por apoyarme y quererme tanto. Sin vosotros no habría llegado donde estoy.

Introduction

Understanding the behavior of matter under extreme conditions of density and temperature has been a matter of debate over the last years in order to gain insight into fundamental aspects of the strong interaction, such as the partial restoration of chiral symmetry [Bro02, Mos99, Wam02], as well as a variety of astrophysical phenomena, e.g, the dynamical evolution of supernovas and the composition of neutron stars [Hei00]. The experimental programs at SIS-GSI, SPS-CERN, RHIC-BNL and the forthcoming operation of LHC [Exp00s] are being developed to clarify the present situation, providing information about the properties of hadrons in hot and dense matter.

A particular effort has been invested in understanding the properties of antikaons due to the direct implications they have in astrophysical phenomena, especially after the speculation of the possible existence of an antikaon condensed phase [Kap86]. If the K^- meson develops sufficient attraction in dense matter it could be energetically

more favorable, after a certain critical density, to neutralize the positive charge of protons with antikaons rather than with electrons. Then, a condensed fraction of K^- would appear softening the equation-of-state and producing, among other phenomena, a substantial reduction of the maximum mass that neutron stars could sustain (see updated references in Ref. [Ram01b] and [Bro94, Li97]).

The study of exotic atoms such as kaonic atoms, in which an electron is replaced by a negatively charged antikaon, can also provide complementary information about the interaction of an antikaon with nuclear matter. There have been some attempts to extract the antikaon-nucleus potential from best-fit analysis of kaonic-atom data and some solutions, which use a phenomenological potential that includes an additional non-linear density dependent term, seem to be in agreement with very strongly attractive well depths of the order of -200 MeV at normal nuclear matter density [Fri94]. A hybrid model that combines a relativistic mean-field approach in the nuclear interior and a phenomenological density dependent potential at the surface that is fitted to K^- atomic data also favors a strongly attractive K^- potential of depth -180 MeV [Fri99a]. However, self-consistent calculations based on chiral lagrangians [Lut98a, Lut98b, Ram00, Scha00] or meson-exchange potentials [Tol01a] only predict moderate attractive depths of -50 to -80 MeV. In addition, studies of kaonic atoms using the chiral $\bar{K}N$ amplitudes of Ref. [Ose98] show that it is indeed possible to find a reasonable reproduction of the data with a relatively shallow antikaon-nucleus potential [Hir00], albeit adding an additional moderate phenomenological piece [Bac00]. This has been recently corroborated by a calculation [Cie01], where a good fit to both scattering K^-p data and kaonic-atom data only required to modify slightly the parameters of the chiral meson-baryon interaction model of Ref. [Kai95]. With the aim of disentangling between different optical potentials [Bac00, Fri94, Fri99b, Ram00], some of them fitted to kaonic

atoms, a recent work [Gar02] has been performed in which the available K^--nucleus scattering data for ^{12}C, ^{40}Ca and ^{208}Pb is compared to the theoretical predictions coming from these potentials. The lesson learned from all these works is that kaonic atom data do not really provide a suitable constraint on the antikaon-nucleus potential at normal nuclear matter density.

Heavy-ion collisions at energies around $1 - 2$ AGeV also offer the possibility of studying experimentally the properties of a dense and hot nuclear system [Oes02, Sen01, Stu02]. In particular, a considerable amount of information about strange particles like antikaons is available. In order to analyze the experimental data, two approaches are commonly followed, namely, transport models that study the evolution and the dynamics of the heavy-ion collision or statistical models that, assuming thermal and chemical equilibrium, account for the particle multiplicities.

Transport models trying to analyze heavy-ion collision data [Bra97, Cas03, Cas97, Eff99, Fuc01, Har98, Ko87, Sib98, Tei97] need to implement the modified properties of the hadrons in the medium where they are produced. They have shown, for instance, that the multiplicity distributions of kaons and antikaons are much better reproduced if in-medium masses rather than bare ones are used [Cas99, Li98]. Production and propagation of kaons and antikaons have been investigated with the Kaon Spectrometer (KaoS) of the SIS heavy-ion synchrotron at GSI (Darmstadt). The experiments have been performed with Au+Au, Ni+Ni, C+C at energies between 0.6 and 2.0 AGeV [Ahn97, Bes97, Cro00, Kao90s, Men00, Mis94, Rit95, Shi98, Stu01]. One surprising observation in C+C and Ni+Ni collisions [Kao90s, Men00] is that, as a function of the energy difference $\sqrt{s} - \sqrt{s}_{th}$, where $\sqrt{s}_{th}$ is the minimum energy to produce the particle (2.5 GeV for K^+ via $pp \to \Lambda K^+ p$ and 2.9 GeV for K^- via $pp \to ppK^-K^+$),

the number of K^- balanced the number of K^+ for equivalent energies in spite of the fact that in pp collisions the production cross-sections close to threshold are 2-3 orders of magnitude different. This has been interpreted to be a manifestation of the enhancement of the K^+ mass and the reduction of the K^- one in the nuclear medium, which in turn influences the corresponding production thresholds [Bra97, Cas03, Cas97, Cas99, Li97, Li98, Sib98], although a complementary explanation in terms of in-medium enhanced $\pi\Sigma \to K^- p$ production has also been suggested [Scha00]. Another interesting observation is that at incident energies of 1.8 and 1.93 AGeV, the K^- and K^+ multiplicities have the same impact parameter dependence [Kao90s, Men00]. Equal centrality dependence for K^+ and K^- and, hence, independence of centrality for the K^-/K^+ ratio is also been observed in Au+Au and Pb+Pb reactions between 1.5 AGeV and RHIC energies [Ahl90s, Dun00, For02, Har01, Men00, Ogi01]. This independence of centrality is astonishing, since at low energies one expects that as centrality increases –and with it the participating system size and the density proved– the K^-/K^+ ratio should also increase due to the increased reduction of the K^- mass together with the enhancement of the K^+ mass. In fact, the independence of the K^-/K^+ ratio on centrality has often been advocated as signaling the lack of in-medium effects. A recent interesting interpretation of this phenomenon is given in Ref. [Har03], where it is shown that the K^- are predominantly produced via πY collisions ($Y = \Lambda, \Sigma$) and, hence, the K^- multiplicity is strongly correlated with the K^+ one, since kaons and hyperons are mainly produced together via the reaction $NN \to KYN$.

Although transport model calculations show that strangeness equilibration requires times of the order of $40 - 80$ fm/c [Bra00, Koc86], surprisingly thermal or statistical models, which assume thermal and chemical equilibrium and common freeze-out parameters for all particles, are quite successful in describing particle yields including

strange particles [Cle00, Cle98a, Cle98b, Cle99a, Cle99b, Cle99c]. The kaon and antikaon yields in the statistical models are based on free masses and no medium effects are needed to describe the enhanced in-medium K^-/K^+ ratio or its independence with centrality. The increased value of the K^-/K^+ ratio is simply obtained by choosing a particular set of parameters at freeze-out, the baryonic chemical potential $\mu_B \simeq 720$ MeV and the temperature $T \simeq 70$ MeV, which also reproduce a variety of particle ratios [Cle00, Cle99c]. On the other hand, centrality independence of the K^-/K^+ ratio is automatically obtained in statistical models within the canonical or grand-canonical schemes because the terms depending on the system size drop out [Cle00]. However, including medium effects may lead to more realistic scenarios, as shown by Brown et al. in Ref. [Bro01a, Bro01b], where using the reduced in-medium K^- mass in the statistical model would force, in order to reproduce the experimental value of the K^-/K^+ ratio, a larger value of the chemical potential and hence a larger and more plausible baryonic density for strangeness production. In addition, Brown et al. introduce the concept of "broad-band equilibration" according to which the K^- mesons and the hyperons are produced in an essentially constant ratio independent of density, hence explaining also the centrality independence of the K^-/K^+ ratio but including medium effects.

All these previous scenarios, namely, neutron stars, kaonic atoms and heavy-ion collisions, show that the antikaon properties in the medium are, at present, object of an intense debate. Although it is commonly accepted that the antikaons should feel an attractive interaction when they are embedded in a nuclear environment, the size of this attraction is not clearly determined yet.

The effort done to clarify the situation from the theoretical point of view, going beyond pure phenomenology, have mainly followed two different strategies. One line

of approach is the mean-field models, built within the framework of chiral Lagrangians [Lee94, Lee95, Lee96, Li97, Mao99] or based on the relativistic Walecka model which are extended to incorporate strangeness in the form of hyperons or kaons [Scha97] or by using explicitly the quark degrees of freedom [Tsu98]. The other type of approach aims at obtaining the in-medium $\bar{K}N$ interaction microscopically [Alb76, Koc94, Lut98a, Ram00, Scha00, Sta87, Tol01a, Waa96a, Waa96b, Waa97] by incorporating the medium modifications in the $\bar{K}N$ amplitude, using chiral-based $\bar{K}N$ interaction models [Gar03, Kai95, Kai97, Koc94, Oll01, Ose98] or meson-exchange potentials [Mul90]. In fact, the dynamics of the $\bar{K}N$ interaction is particularly rich due to the presence of an isospin zero resonance, the $\Lambda(1405)$, which lies only 27 MeV below the $\bar{K}N$ threshold. This resonance is generated dynamically from a T-matrix scattering equation in coupled channels using a suitable meson-baryon potential. The coupling between the $\bar{K}N$ and πY ($Y = \Lambda, \Sigma$) channels is essential to get the right dynamical behavior in free space. As a result of the existence of this resonance, the isospin averaged $\bar{K}N$ scattering amplitude is in fact repulsive. It was soon pointed out, however, that in the medium the Pauli blocking on nucleon states moves the resonance to higher energies and the in-medium amplitude becomes attractive [Koc94, Waa96a, Waa96b, Waa97]. This particular (resonant-like) energy dependence of the $\bar{K}N$ interaction at subthreshold energies requires an especially careful treatment of all in-medium effects. In fact, when the attraction felt by the antikaon is self-consistently incorporated in the calculation [Lut98a, Lut98b, Ram00, Scha00] it compensates partly the effects induced by Pauli blocking and the Λ resonance gets broader and moves back to lower energies, around its free space location. Moreover, since an extremely important ingredient to generate the Λ resonance is the coupling of the $\bar{K}N$ system to the $\pi\Sigma$ one, the modification of the pion properties has also shown to be relevant Ref. [Ram00], with the result that

the resonance width increases further more and the peak shifts upwards to an energy slightly above the free space one. Nevertheless, most works until now have ignored this contribution [Lut98a, Scha00, Tol01a, Cie01]. On the other hand, since antikaons are produced at finite density and finite momentum in heavy-ion collisions, the chiral models have recently incorporated the partial waves beyond the $L = 0$ component of the antikaon-nucleon scattering amplitude both in free space[Car00, Jid02, Lut02a] and in the nuclear medium [Kol02, Lut02b]. The complete scenario taking into account finite density, finite momentum and finite temperature has been addressed in Refs. [Scha00, Tol02].

The purpose of this thesis is to present a proper self-consistent calculation of the antikaon properties in dense and hot matter in order to explore the typical conditions found in heavy-ion collisions at GSI, studying the posssible implications that the inclusion of the in-medium effects at finite temperature on the antikaon optical potential would have on the K^-/K^+ ratio. The outlook of this thesis is the following:

Chapter 1 presents the scattering theory for the $\bar{K}N$ system. The coupled-channel Bethe-Salpeter equation is solved taking, as a bare meson-baryon interaction, the meson-exchange potential of the Jülich group [Mul90]. The predictions for some $\bar{K}N$ scattering observables, such as the K^-p cross sections, the s-wave scattering amplitudes and several branching ratios at $\bar{K}N$ threshold are also given.

With regard to the in-medium properties of the $\bar{K}$ meson in symmetric nuclear matter, the Brueckner-Hartree-Fock approximation for the in-medium $\bar{K}N$ interaction or G-matrix is presented in Chapter 2. Two self-consistent schemes are discussed and the momentum dependence of the $\bar{K}$ optical potential together with the effect of higher partial waves of the $\bar{K}N$ interaction, beyond the $L = 0$ component, are also carefully

considered due to the fact that antikaons are produced at finite momentum in heavy-ion collisions.

Since heavy-ion collisions produce not only dense but also hot matter, the antikaon optical potential at finite temperature is studied in Chapter 3. The aim is to investigate the influence of temperature on the behavior of the antikaon potential for the experimental conditions at GSI.

Finally, Chapter 4 considers the K^-/K^+ ratio in the framework of thermal models including the in-medium properties at finite temperature of the hadrons involved and paying particular attention to the antikaons. Different approaches for the K^- self-energy are taken into account so as to analyze the effects on the determination of this ratio.

The main conclusions of this work are summarized and exposed at the end of the manuscript.

Chapter 1

Scattering observables of the $\bar{K}N$ interaction

This chapter is devoted to present the scattering theory for the $\bar{K}N$ system. Section 1.1 reviews the meson-baryon interaction introducing the Bethe-Salpeter equation and some observables obtained from meson-baryon scattering. In Section 1.2, the $\bar{K}N$ interaction is presented. The previous knowledge of the Bethe-Salpeter equation and its three dimensional reduction, the Lippman-Schwinger equation, is applied for the Jülich $\bar{K}N$ meson-exchange potential in coupled channels [Mul90]. Finally, in the last section, the results obtained within this framework for the $\Lambda(1405)$ resonance, the K^-p elastic and inelastic cross sections, the s-wave scattering amplitudes and some threshold ratios are shown.

1.1 The meson-baryon interaction

Quantum Chromodynamics (QCD) is the fundamental theory of strong interactions. Therefore, the hadron-hadron interaction (V_{hh}) is in principle completely determined by the underlying quark-gluon dynamics. However, due to our present lack of knowledge about how to treat the non-perturbative character of QCD in the low energy regime and, especially, because of the problem of the confinement mechanism, we are far away from a quantitative understanding of the hadron-hadron force from this perspective.

In order to overcome this problem, *phenomenological approaches* to V_{hh} are used, in which the experimental data are fitted. From a theoretical point of view, the intractability of low energy QCD is usually circumvented by introducing 'QCD inspired models', in which the relevant degrees of freedom are hadrons. One of these models is the *effective chiral lagrangian formalism* , which has proved to be successful in explaining the properties of the meson-meson interaction at low energies [Gas85, Mei93, Pic95], being also an excellent tool to study low energy properties of the meson-baryon interaction when the interaction is weak [Ber95, Eck95]. In this case, an expansion in powers of the typical momenta involved in the process is fully justified. A more sophisticated chiral scheme arises when resonances show up. For this problem, one needs a non-perturbative chiral scheme (see, for instance, [Gar03, Kai95, Oll01, Ose98] for $\bar{K}N$ scattering).

Another approach to the hadron-hadron interaction is the *meson-exchange models* (see, for example, Refs. [Nag73, Mac87] for nucleon-nucleon interaction). There is a solid theoretical background and a strong phenomenological evidence for this meson picture of the nuclear force. The overwhelming part of the strong force can be constructed

in terms of meson-meson-meson and baryon-meson-baryon vertices, which represent a natural and effective description of complicated multi-quark reactions. Hadron masses, coupling constants and vertex-form factors are then left to be ultimately explained by QCD. This last scheme will be the one followed in our study of the $\bar{K}N$ interaction.

1.1.1 The meson-baryon Bethe-Salpeter equation

In order to obtain the meson-baryon amplitude, the *Bethe-Salpeter equation* is used as the starting-point. The covariant Bethe-Salpeter equation in momentum space, supressing spin and isospin labels for simplicity, takes the following form (see, for example, Ref. [Itz80]):

$$\mathcal{T}_{ij}(k_i,k_j;P) = \mathcal{V}_{ij}(k_i,k_j;P) + i\sum_l \int \frac{d^4k_l}{(2\pi)^4} \mathcal{V}_{il}(k_i,k_l;P)\, D_B(k_l,P)\, D_m(k_l,P) \mathcal{T}_{lj}(k_l,k_j;P)\,, \tag{1.1}$$

where k_i, k_j are the initial and final relative four-momenta, respectively, and k_l the intermediate meson four-momentum whereas P is the total four-momentum of the system. The relativistic baryon (meson) propagator $D_{B(m)}(k_l,P)$ reads

$$D_B(k_l,P) = \frac{1}{(\not{P} - \not{k}_l) - M_l + i\epsilon}, \qquad D_m(k_l,P) = \frac{1}{k_l^2 - m_l^2 + i\epsilon}\,, \tag{1.2}$$

with M_l and m_l being, respectively, the masses of the baryon and the meson in the intermediate channel l. The invariant amplitude for the two-particle scattering process is represented by $\mathcal{T}$, commonly called T-matrix, and $\mathcal{V}$ is the meson-baryon potential that, in a meson-exchange framework or using chiral effective lagrangians, results from the sum of all two-particle irreducible diagrams. Usually one works in the center-of-

mass frame with $P = (\sqrt{s}, 0)$ where k_l transforms into the relative four-momentum.

This four-dimensional integral equation turns out to be tedious to solve. Then, it is usually replaced by three-dimensional reductions, more practical for numerical purposes. Moreover, one more simplification will be used: only the positive energy component of the baryon propagator is kept, because we are only concerned with the positive solutions to the energy. Explicitly

$$\frac{1}{(\not{P} - \not{k}_l) - M + i\epsilon} \to \frac{M}{E_l(\vec{k}_l)} \; \frac{u_l \bar{u}_l}{\sqrt{s} - k_l^0 - E_l(\vec{k}_l) + i\epsilon} \; , \tag{1.3}$$

where M and $E_l(\vec{k}_l)$ are the mass and energy of the baryon, respectively, and u_l is a Dirac spinor. It is convenient to split the meson propagator into the particle and antiparticle contributions

$$\frac{1}{k_l^2 - m^2 + i\epsilon} = \frac{1}{2k_l^0} \left(\frac{1}{k_l^0 - \omega_l(\vec{k}_l) + i\epsilon} + \frac{1}{k_l^0 + \omega_l(\vec{k}_l) - i\epsilon} \right) \; , \tag{1.4}$$

where m and $\omega_l(\vec{k}_l)$ are the mass and energy of the meson, respectively. Introducing Eq. (1.3) and Eq. (1.4) in Eq. (1.1), and defining

$$\widetilde{T}_{ij} = \bar{u}_i \mathcal{T}_{ij} u_j \; , \tag{1.5}$$

one obtains the *Lippman-Schwinger equation* (LS) by integrating out the time component k_l^0 (see Ref. [Lee98])

$$\begin{aligned} &\widetilde{T}_{ij}(\vec{k}_i, \vec{k}_j; \sqrt{s}) = \widetilde{V}_{ij}(\vec{k}_i, \vec{k}_j; \sqrt{s}) \\ &+ \sum_l \int \frac{d^3 k_l}{(2\pi)^3} \frac{M_l}{E_l(\vec{k}_l)} \frac{1}{2\omega_l(\vec{k}_l)} \frac{\widetilde{V}_{il}(\vec{k}_i, \vec{k}_l; \sqrt{s}) \; \widetilde{T}_{lj}(\vec{k}_l, \vec{k}_j; \sqrt{s})}{\sqrt{s} - E_l(\vec{k}_l) - \omega_l(\vec{k}_l) + i\epsilon} \; . \end{aligned} \tag{1.6}$$

In this last expression we have used $k^2 = m^2$ to eliminate the dependence on the time component of the four-momenta.

Defining

$$T_{ij} = \frac{1}{(2\pi)^3}\sqrt{\frac{M_i}{E_i(\vec{k}_i)}}\sqrt{\frac{1}{2\omega_i(\vec{k}_i)}}\widetilde{T}_{ij}\sqrt{\frac{M_j}{E_j(\vec{k}_j)}}\sqrt{\frac{1}{2\omega_j(\vec{k}_j)}}\ , \tag{1.7}$$

we are able to absorbe the energy/mass factors within the T-matrix. Therefore, the LS equation reads

$$T_{ij}(\vec{k}_i,\vec{k}_j;\sqrt{s}) = V_{ij}(\vec{k}_i,\vec{k}_j;\sqrt{s}) + \sum_l \int d^3k_l \, \frac{V_{il}(\vec{k}_i,\vec{k}_l;\sqrt{s})\ T_{lj}(\vec{k}_l,\vec{k}_j;\sqrt{s})}{\sqrt{s} - E_l(\vec{k}_l) - \omega_l(\vec{k}_l) + i\epsilon}\ . \tag{1.8}$$

This is the expression of the LS equation that is used for the $\bar{K}N$ system when using the Jülich $\bar{K}N$ meson-exchange potential [Mul90], in which the definition of $V_{ij}(\vec{k}_i,\vec{k}_j;\sqrt{s})$ consistently contains these energy/mass factors.

The relation between the experimental measurements (cross sections and scattering amplitudes) and the meson-baryon T-matrix obtained from the solution of the LS equation will be established in the next section. However, we are showing first how to solve the LS in the partial wave basis.

1.1.1.1 Partial wave decomposition

In order to solve the Bethe-Salpeter equation or its three-dimensional reduction, the Lippman-Schwinger equation, for a two particle system, one usually works in the partial wave basis. The physical basis $|(\mathcal{P}_1\mathcal{P}_2)\vec{k}_1\vec{k}_2 s_1 s_2 \sigma_1\sigma_2 t_1 t_2 \tau_1\tau_2\rangle$, where $\mathcal{P}$, $\vec{k}$, s, σ, t, τ indicate the type of particle, the three-momentum vector, the spin, the third component

of spin, the isospin and its third component, respectively, has to be rewritten in terms of its partial wave decomposition $|(\mathcal{P}_1\mathcal{P}_2)\vec{P}kLSJMIM_I\rangle$, i.e, in terms of the total centre-of-mass momentum $\vec{P}$, the modulus of the relative momentum k, the total orbital angular momentum L, the total spin S, the total angular momentum J, the third component M of the angular momentum, the total isospin I and the third compoment of isospin M_I. Therefore, all the terms in the Lippman-Schwinger equation

$$T = V + V\ \frac{1}{E}\ T\ , \tag{1.9}$$

have to be expressed in this new basis. We will restrict ourselves to the meson-baryon case in which $\mathcal{P}_1$ is a meson (M) and $\mathcal{P}_2$ turns out to be a baryon (B).

The meson-baryon potential V in the meson-exchange framework is commonly given in the partial wave basis due to the invariance properties of the interaction. In fact, this is one of the reasons to solve the Lippman-Schwinger equation in the partial wave basis. Translational and rotational invariance together with the isospin symmetry characteristic of the strong interaction allow one to write

$$\begin{aligned}\langle(M_1B_1)\vec{P}'k'L'S'J'M'I'M_I'|V|(M_2B_2)\vec{P}kLSJMIM_I\rangle = \delta_{\vec{P}\vec{P}'}\delta_{JJ'}\delta_{MM'}\times \\ \delta_{II'}\delta_{M_IM_I'}\langle(M_1B_1)\vec{P}k'L'S'JMIM_I|V|(M_2B_2)\vec{P}kLSJMIM_I\rangle\ .\end{aligned} \tag{1.10}$$

The possible difficulties come of expressing the propagator $1/E$ in partial wave decomposition, especially when the medium effects are included. In this subsection we present the explicit derivation of the transformation from the physical basis to the partial wave basis. The necessary changes or approximations required for the inclusion of the medium effects will be described in the next chapter.

The propagator for a meson-baryon interaction is diagonal in the physical basis and can be written as

$$
\begin{aligned}
D_{MB}(\vec{k_1},\vec{k_2}) &= \langle (MB)\vec{k}_1\vec{k}_2 s_1 s_2 \sigma_1\sigma_2 t_1 t_2 \tau_1\tau_2| \ \frac{1}{E} \ |(MB)\vec{k}_1\vec{k}_2 s_1 s_2 \sigma_1\sigma_2 t_1 t_2 \tau_1\tau_2\rangle \ , \\
D_{MB}(\vec{k_1},\vec{k_2}) &= \frac{1}{\Omega - \sqrt{\vec{k}_1^{\,2}+m_1^2} - \sqrt{\vec{k}_2^{\,2}+m_2^2} + i\epsilon} \ ,
\end{aligned}
\tag{1.11}
$$

where Ω is the starting energy with $\sqrt{s} = \sqrt{\Omega^2 - \vec{P}^{\,2}}$. For the scattering process in the center-of-mass frame, Ω is equal to $\sqrt{s}$.

In order to express the propagator in the partial wave basis, the transformation between bases is used. First, we decouple the spin and isospin via

$$
\begin{aligned}
|SM_S\rangle &= \sum_{\sigma_1\sigma_2} (s_1 s_2 \sigma_1\sigma_2 | SM_S) \ |\sigma_1\sigma_2\rangle \\
|IM_I\rangle &= \sum_{\tau_1\tau_2} (t_1 t_2 \tau_1\tau_2 | IM_I) \ |\tau_1\tau_2\rangle \ .
\end{aligned}
\tag{1.12}
$$

Afterwards, $\vec{k}_1 \equiv \vec{k}_M$ and $\vec{k}_2 \equiv \vec{k}_B$ are expressed in terms of the center of mass momentum $\vec{P}$ and the relative one $\vec{k}$

$$
\begin{aligned}
\vec{P} = \vec{k}_M + \vec{k}_B, \quad \vec{k} &= \frac{m_B\vec{k}_M - m_M\vec{k}_B}{m_M + m_B} \ , \\
\vec{k}_B = -\vec{k} + \frac{\xi}{1+\xi}\vec{P}, \quad \vec{k}_M &= \vec{k} + \frac{1}{1+\xi}\vec{P} \ ,
\end{aligned}
\tag{1.13}
$$

with $\xi = m_B/m_M$ and one makes use of

$$
|kLM_L\rangle = \int d\hat{k} \ Y_{LM_L}(\hat{k}) \ |\vec{k}\rangle \ ,
\tag{1.14}
$$

where the unit vector $\widehat{k}$ is defined as $\widehat{k} = \vec{k}/|\vec{k}|$.

Finally we decouple the total angular momentum J

$$|LSJM\rangle = \sum_{M_L M_S} (LM_L SM_S|JM) \ |LM_L SM_S\rangle \ . \tag{1.15}$$

The coupled basis is then expressed in terms of the physical basis as

$$\begin{aligned} |(MB)\vec{P}kLSJMIM_I\rangle = & \sum_{\substack{\sigma_1\sigma_2\tau_1\tau_2 \\ M_L M_S}} \int d\widehat{k} \ Y_{LM_L}(\widehat{k}) \ (s_1 s_2 \sigma_1 \sigma_2 | SM_S) \\ & \times (t_1 t_2 \tau_1 \tau_2 | IM_I)(LM_L SM_S|JM) \ |(MB)\vec{P}\vec{k} s_1 s_2 \sigma_1 \sigma_2 t_1 t_2 \tau_1 \tau_2\rangle \ , \end{aligned} \tag{1.16}$$

or inversely

$$\begin{aligned} |(MB)\vec{P}\vec{k} s_1 s_2 \sigma_1 \sigma_2 t_1 t_2 \tau_1 \tau_2\rangle = & \sum_{\substack{LM_L SM_S \\ JMIM_I}} Y^*_{LM_L}(\widehat{k}) (s_1 s_2 \sigma_1 \sigma_2 | SM_S) \\ & \times (t_1 t_2 \tau_1 \tau_2 | IM_I)(LM_L SM_S|JM) \ |(MB)\vec{P}kLSJMIM_I\rangle \ , \end{aligned} \tag{1.17}$$

where the inverse relations have been used

$$\begin{aligned} |\sigma_1\sigma_2\rangle &= \sum_{SM_S} (s_1 s_2 \sigma_1 \sigma_2 | SM_S) \ |SM_S\rangle \ , \\ |\tau_1\tau_2\rangle &= \sum_{IM_I} (t_1 t_2 \tau_1 \tau_2 | IM_I) \ |IM_I\rangle \ , \qquad (1.18) \\ |\vec{k}\rangle &= \sum_{LM_L} Y^*_{LM_L}(\widehat{k}) \ |kLM_L\rangle \ , \qquad (1.19) \\ |LM_L SM_S\rangle &= \sum_{JM} (LM_L SM_S|JM) \ |LSJM\rangle \ . \qquad (1.20) \end{aligned}$$

Using Eq.(1.11) and (1.16), we can write the propagator in partial wave basis as

$$\langle (MB)\vec{P}kL'S'J'M'I'M'_I|\ \frac{1}{E}\ |(MB)\vec{P}kLSJMIM_I\rangle =$$
$$\sum_{\substack{\sigma_1\sigma_2\tau_1\tau_2\\ M_S M_L M'_S M'_L}} (s_1 s_2 \sigma_1\sigma_2|SM_S)(s_1 s_2\sigma_1\sigma_2|S'M'_S)(t_1 t_2\tau_1\tau_2|IM_I)(t_1 t_2\tau_1\tau_2|I'M'_I)$$
$$\times(LSM_L M_S|JM)(L'S'M'_L M'_S|J'M')\int d\widehat{k}\ Y^*_{L'M'_L}(\widehat{k})\ D_{MB}(k,\widehat{k},\vec{P}\,)\ Y_{LM_L}(\widehat{k}) \quad (1.21)$$

In this equation, the diagonal property of the propagator in the physical basis has been employed.

Restricting ourselves to the Lippman-Schwinger equation, without including any medium effects, it is easily seen that the propagator is independent of spin and isospin. Therefore, using the orthogonality property

$$\sum_{m_1 m_2} (j_1 j_2 m_1 m_2|jm)(j_1 j_2 m_1 m_2|j'm') = \delta_{jj'}\delta_{mm'}\ , \quad (1.22)$$

for spin and isospin, the sum over σ_1, σ_2 and τ_1, τ_2 can be performed obtaining

$$\langle (MB)\vec{P}kL'SJ'M'IM_I|\ \frac{1}{E}\ |(MB)\vec{P}kLSJMIM_I\rangle =$$
$$\sum_{M_S M_L M'_L} (LSM_L M_S|JM)(L'SM'_L M_S|J'M')\int d\widehat{k}\ Y^*_{L'M'_L}(\widehat{k})\ D_{MB}(k,\widehat{k},\vec{P}\,)\ Y_{LM_L}(\widehat{k}) \quad (1.23)$$

Up to here the formalism has been written in a way that will be convenient for introducing the medium effects in the next chapter. In free space, the invariance of the amplitude allows one to perform the calculation in the center-of-mass frame where the propagator D_{MB} does not depend on the angle and, hence, the integral of the solid angle in Eq. (1.23) can be calculated straightforwardly. The integral over ϕ of

the spherical harmonics gives a $\delta_{M_L M'_L}$ factor, allowing to sum over M'_L and, hence, $M = M' = M_L + M_S$. On the other hand, $\delta_{LL'}$ appears if we perform the integral over the angle θ. Then, the $\sum_{M_S M_L}$ can be done using again the orthogonality property of Eq. (1.22), finally observing that the propagator is diagonal in both basis. Therefore, the Lippman-Schwinger equation in the partial wave basis can be written as

$$\begin{aligned}
&\langle (M_1 B_1)\vec{P}k'L'S'JMIM_I|T|(M_2 B_2)\vec{P}kLSJMIM_I\rangle = \\
&\langle (M_1 B_1)\vec{P}k'L'S'JMIM_I|V|(M_2 B_2)\vec{P}kLSJMIM_I\rangle + \\
&\sum_{M_3 B_3}\sum_{L''S''}\int dk'' k''^2 \langle (M_1 B_1)\vec{P}k'L'S'JMIM_I|V|(M_3 B_3)\vec{P}k''L''S''JMIM_I\rangle \\
&\times \frac{1}{\Omega - E_{B_3}(k'',\vec{P}) - \omega_{M_3}(k'',\vec{P}) + i\epsilon} \\
&\times \langle (M_3 B_3)\vec{P}k''L''S''JMIM_I|T|(M_2 B_2)\vec{P}kLSJMIM_I\rangle \ . \qquad (1.24)
\end{aligned}$$

where in this case $\vec{P}$ is taken to zero.

1.1.2 The S-matrix: cross section and s-wave scattering amplitudes

In this section the *S-matrix* (or collision operator) is studied. It contains the complete information about all collision processes, relating the dynamical content of the Bethe-Salpeter equation with the measurable parameters, like the experimental cross sections.

In a collision process (see Ref. [Man84, Itz80]), we define a state vector $|\Phi(-\infty)\rangle = |i\rangle$ as an initial state, long before the scattering occurs ($t_i = -\infty$). It specifies a definite number of particles with definite properties and far apart from each other so that they don't interact. In the scattering process, the particles will come close together, collide

and fly apart again. Then, at $t = \infty$, long after the scattering is over and all particles are far apart again, we can define $|\Phi(\infty)\rangle$ into which the initial state evolves. The S-matrix relates $|\Phi(-\infty)\rangle$ with $|\Phi(\infty)\rangle$ and is defined by

$$|\Phi(\infty)\rangle = S|\Phi(-\infty)\rangle = S|i\rangle \ . \tag{1.25}$$

A collision can lead to many different final states $|f\rangle$, and all these possibilities are contained within $|\Phi(\infty)\rangle$. The transition probability that after the collision the system is the state $|f\rangle$ is given by

$$|\langle f|\Phi(\infty)\rangle|^2 \ , \tag{1.26}$$

and the corresponding amplitude is

$$\langle f|\Phi(\infty)\rangle = \langle f|S|i\rangle \equiv S_{if} \ , \tag{1.27}$$

where S_{if} is a unitary matrix which can be defined as [Itz80]

$$S_{if} = \delta_{if} - i(2\pi)^4\delta^{(4)}(P_i - P_f)\bar{T}_{if} \ , \tag{1.28}$$

where i,f denote the initial and final state, P is the total four-momentum of the system, and $\bar{T}_{if}$ is the scattering T-amplitude that contains the information on the interactions. This amplitude ($\bar{T}_{if}$) and the invariant amplitude defined by the Bethe-Salpeter equation and calculated in the three-dimensional approach or Lippman-Schwinger equation ($\widetilde{T}_{if}$) are related as follows

$$\bar{T}_{if} = \prod_{fermions}\left(\frac{m}{VE}\right)^{\frac{1}{2}} \prod_{bosons}\left(\frac{1}{2V\omega}\right)^{\frac{1}{2}} \widetilde{T}_{if} \ , \tag{1.29}$$

where the normalization factors coming from the fermion/boson fields are factorized out, being m and E the mass/energy of the baryons and ω the energy of mesons, respectively, while V is the volume of the system. Following Ref. [Man84], the probability for the transition over the whole space-time will be

$$|S_{i\neq f}|^2 = (2\pi)^8[\delta^{(4)}(P_f - P_i)]^2 \prod_{fermions}\left(\frac{m}{VE}\right)\prod_{bosons}\left(\frac{1}{2V\omega}\right)|\widetilde{T}_{if}|^2 \ . \tag{1.30}$$

To derive the cross section, it is useful to take the time (t) and volume (V) finite. In this case

$$[\delta^{(4)}(P_f - P_i)]^2 = \delta^{(4)}(P_f - P_i)\frac{Vt}{(2\pi)^4} \ , \tag{1.31}$$

and, therefore, the transition probability per unit time ω_t is

$$\omega_t = \frac{|S_{i\neq f}|^2}{t} = V(2\pi)^4\delta^{(4)}(P_f - P_i)\prod_{fermions}\left(\frac{m}{VE}\right)\prod_{bosons}\left(\frac{1}{2V\omega}\right)|\widetilde{T}_{if}|^2 \ . \tag{1.32}$$

Eq. (1.32) is the transition rate to a definite final state. To obtain transitions to a specific group of final states with momenta between $\vec{k}_f$ and $\vec{k}_f + d\vec{k}_f$, we must multiply ω_t by the number of the states in this interval

$$\prod_f \frac{Vd^3k_f}{(2\pi)^3} \ . \tag{1.33}$$

The differential cross section is defined as the transition rate into this group of final states for one scattering centre and unit incident flux. The volume V that we are considering contains one scattering centre, and the incident flux is v_{rel}/V, where v_{rel} is the relative velocity of the colliding particles. Therefore, the differential decay rate

for two-particle scattering becomes

$$d\widetilde{\sigma}_{if} = \omega_t \frac{V}{v_{rel}} \prod_f \frac{V d^3k_f}{(2\pi)^3} = (2\pi)^4 \delta^{(4)}(P_f - P_i) \frac{1}{v_{rel}} \frac{1}{2\varepsilon_1 2\varepsilon_2} \prod_l (2M_l) \prod_f \frac{d^3k_f}{(2\pi)^3 2\varepsilon_f} |\widetilde{T}_{if}|^2 \ , \tag{1.34}$$

being ε_1 and ε_2 the energies of the initial colliding particles. The product over M_l stays for the fermions in the initial/final state and ε_f is the energy of the final states.

In many experiments, the colliding particles are unpolarized and the polarizations of the final-state particles are not detected. Therefore, we will sum over all final states compatible with the initial conditions and average over the initial states

$$\begin{aligned} d\sigma_{if} &= \overline{\sum_i} \sum_f d\widetilde{\sigma}_{if} \\ \overline{\sum_i} &= \frac{1}{(2s_1+1)(2s_2+1)} \ , \end{aligned} \tag{1.35}$$

with s_1, s_2 being the spin of the initial particles.

Considering now the case of two colliding particles (1,2) going to a two-particle final state (3,4), and working in the center-of-mass frame, the relative velocity is $v_{rel} = k\frac{\sqrt{s}}{\varepsilon_1 \varepsilon_2}$, with $\sqrt{s} = \varepsilon_1 + \varepsilon_2$, and k the modulus of the momentum of the initial particles. It can also be shown that [Mui65]

$$\sum_f \ d^3p_3 \ d^3p_4 \ \delta^{(4)}(P_i - P_f) = \sum_\alpha d\Omega_3 \ \varepsilon_3 \ \varepsilon_4 \ \frac{k'}{\sqrt{s}} \ , \tag{1.36}$$

where the sum α is over the remaining final states, k' is the modulus of the momentum of the final two particles in the center-of-mass frame and $d\Omega \equiv d\Omega_3 = \pi - d\Omega_4$ is the solid angle. Using all these ingredients, the final expression for the differential cross

section in the case of meson-baryon scattering is

$$\frac{d\sigma_{if}}{d\Omega} = \frac{1}{(2\pi)^2}\frac{1}{s}\frac{M_1 M_3}{4}\,\frac{k'}{k}\,\overline{\sum_i}\sum_\alpha |\widetilde{T}_{if}|^2 \,, \tag{1.37}$$

or, using Eq.(1.7), it can be rewritten as

$$\frac{d\sigma_{if}}{d\Omega} = (2\pi)^4\frac{E_1\omega_2 E_3\omega_4}{s}\,\frac{k'}{k}\,\overline{\sum_i}\sum_\alpha |T_{if}|^2 \,, \tag{1.38}$$

which will be the expression used in the next section for the $\bar{K}N$ interaction. Then, the *total cross section* in the center-of-mass frame is given by

$$\sigma_{if} = \int d\Omega\,\frac{d\sigma_{if}}{d\Omega} \,. \tag{1.39}$$

In Eq. (1.38), the T-matrix elements are expressed in the physical basis. Having obtained previously the T-matrix elements in the coupled basis as shown in Eq. (1.24), Eq. (1.17) should be used to express the physical basis in terms of coupled one. Restricting ourselves to the case of a meson of spin zero and a baryon of spin 1/2, one can write

$$\begin{aligned}
&\langle \vec{P}\,\vec{k}'\,s' = \tfrac{1}{2}\,\sigma'\,t_1'\,t_2'\,\tau_1'\,\tau_2'|\;T\;|\vec{P}\,\vec{k}\,s = \tfrac{1}{2}\,\sigma\,t_1\,t_2\,\tau_1\,\tau_2\rangle = \sum_{JLL'I}\sum_{M M_L M_L'} Y_{L'M_L'}(\widehat{k}')\;Y^*_{LM_L}(\widehat{k})\\
&\times\;(t_1'\,t_2'\,\tau_1'\,\tau_2'|I\,(\tau_1'+\tau_2'))\;(t_1\,t_2\,\tau_1\,\tau_2|I\,(\tau_1+\tau_2))\;(L'\,M_L'\,\tfrac{1}{2}\,\sigma'|J\,M)\;(L\,M_L\,\tfrac{1}{2}\,\sigma|J\,M)\\
&\times\;\langle \vec{P}\,k'\,L'\,\tfrac{1}{2}\,J\,M\,I\,(\tau_1'+\tau_2')|\;T\;|\vec{P}\,k\,L\,\tfrac{1}{2}\,J\,M\,I\,(\tau_1+\tau_2)\rangle \,,
\end{aligned} \tag{1.40}$$

where the initial and final states have $S = S' = s' = s$ =1/2, with third components $M_S(M_S') = \sigma(\sigma')$ and where the third component of isospin is $M_I = \tau_1' + \tau_2' = \tau_1 + \tau_2$.

Taking $\widehat{k}$ along z-axis

$$Y^*_{LM_L}(\widehat{k}) = \sqrt{\frac{2L+1}{4\pi}}\delta_{M_L,0} \ , \tag{1.41}$$

it implies that $M = \sigma$ and $M'_L = \sigma - \sigma'$. Therefore, the expression reduces to

$$\begin{aligned}
&\langle \vec{P}\,\vec{k}'\,s' = \tfrac{1}{2}\,\sigma'\,t'_1\,t'_2\,\tau'_1\,\tau'_2|\ T\ |\vec{P}\,\vec{k}\,s = \tfrac{1}{2}\,\sigma\,t_1\,t_2\,\tau_1\,\tau_2\rangle = \sum_{JLI}\sqrt{\frac{2L+1}{4\pi}}\ Y_{L,\sigma-\sigma'}(\widehat{k}') \\
&\times\ (t'_1\,t'_2\,\tau'_1\,\tau'_2|I\,(\tau'_1+\tau'_2))\ (t_1\,t_2\,\tau_1\,\tau_2|I\,(\tau_1+\tau_2))\ (L\,\sigma-\sigma'\,\tfrac{1}{2}\,\sigma'|J\,\sigma)\ (L\,0\,\tfrac{1}{2}\,\sigma|J\,\sigma) \\
&\times\langle \vec{P}\,k'\,L\,\tfrac{1}{2}\,J\,\sigma\,I\,(\tau'_1+\tau'_2)|\ T\ |\vec{P}\,k\,L\,\tfrac{1}{2}\,J\,\sigma\,I\,(\tau_1+\tau_2)\rangle \ ,
\end{aligned} \tag{1.42}$$

with $L = L'$ since the two angular momentum values compatible with a given J, $L = J \pm 1/2$, cannot be connected by the interaction due to parity conservation.

To facilitate the comparison with the physical observables, it is convenient to introduce the *partial wave scattering amplitudes* and relate them to the T-matrix just derived.

Let us first start with the scattering of one particle in the presence of a non-relativistic potential to introduce the concept of *scattering amplitude* and generalize it afterwards for the relativistic scattering of two particles, which is the problem we are interested in.

Note that only for spinless particles and in the non-relativistic case, this problem reduces to the simple one of potential scattering. Following Ref. [Joa75], the stationary scattering wave function, $\Psi^{(+)}_{\vec{k}}(\vec{r})$, of a non-relativistic spinless particle of mass m scattered by a potential $V(r)$ can be obtained by solving the corresponding Schrödinger equation. Assuming that the potential tends to zero faster than r^{-1} as $r \to \infty$, the

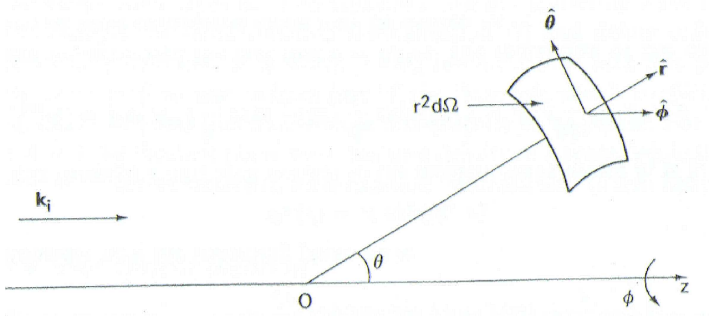

Figure 1.1: Illustration of the coordinates used in the test. Taken from Ref. [Joa75].

solution satisfies the asymptotic boundary condition

$$\Psi_{\vec{k}}^{(+)}(\vec{r})_{r\to\infty} A\left(exp(i\vec{k}\vec{r}) + f(k,\theta,\phi)\frac{exp(ikr)}{r}\right) \ . \tag{1.43}$$

This solution is a superposition of a plane wave of wave vector $\vec{k}$ and an outgoing spherical wave with an amplitude depending on θ and ϕ and inversely proportional to r. The meaning of this amplitude will come clear in the following.

Let us again calculate the differential cross section $d\sigma_{if}/d\Omega$. Defined as the number of particles emitted per unit time and unit incident flux within the solid angle $d\Omega$ in the direction $\Omega(\theta,\phi)$ [see Fig. 1.1], it is equal to the outgoing flux of particles scattered through the spherical surface $r^2\ d\Omega$ (for $r\to\infty$), divided by the incident flux. It can be seen that [Joa75]

$$\frac{d\sigma_{if}}{d\Omega}d\Omega = \frac{|\vec{j}_f|}{|\vec{j}_i|}r^2\, d\Omega = |f(k,\theta,\phi)|^2\, d\Omega \ , \tag{1.44}$$

where the incident and outgoing fluxes are calculated according to $j \sim \mathrm{Re}\{\Psi^*(\vec{r})\overline{\nabla}_{\vec{r}}\Psi(\vec{r})\}$, using first and second terms of Eq. (1.43), respectively. Therefore, the $f(k,\theta,\phi)$ amplitude is called *scattering amplitude*. This relation between the asymptotic behaviour of

the wave function $\Psi^{(+)}_{\vec{k}}(\vec{r})$ and the differential cross section is of fundamental importance since it links our theoretical knowledge, contained in $\Psi^{(+)}_{\vec{k}}(\vec{r})$, to the experimental quantity $d\sigma_{if}/d\Omega$.

Using the asymptotic form of the scattering wave function $\Psi^{(+)}_{\vec{k}}(\vec{r})$, introduced previously, and matching coefficients with its partial wave representation (following Ref. [Joa75]), we obtain the scattering amplitude as

$$f(k,\theta) = \frac{1}{k}\sum_{l=0}^{\infty} (2l+1)\ \exp(i\delta_l(k))\sin(\delta_l(k))\ P_l(cos\theta)\ , \tag{1.45}$$

where the dependence on ϕ has disappeared, and the Legendre polynomials and the *phase shift* $\delta_l(k)$ concept have been introduced. The phase shift $\delta_l(k)$ displays the influence of the interaction. We may also write Eq. (1.45) in the form

$$f(k,\theta) = \sum_{l=0}^{\infty} (2l+1)\ a_l(k)\ P_l(cos\theta) = 4\pi \sum_{l=0}^{\infty}\sum_{m=-l}^{+l} a_l(k)\ Y_{lm}(\widehat{k'})Y^*_{lm}(\widehat{k})\ , \tag{1.46}$$

where for the last equality we have used the addition theorem of the spherical harmonics

$$P_l(cos\theta) = \frac{4\pi}{2l+1}\sum_{m=-l}^{+l} Y_{lm}(\widehat{k'})Y^*_{lm}(\widehat{k}) \qquad cos\theta = \widehat{k}\cdot\widehat{k'}\ . \tag{1.47}$$

Then, the *partial wave scattering amplitudes* a_l are such that

$$a_l(k) = \frac{1}{k}\exp(i\delta_l(k))\ \sin(\delta_l(k))\ . \tag{1.48}$$

Thus the knowledge of the phase shifts enables one to obtain the scattering amplitude.

In analogy with this simple case of potential scattering, it is convenient to intro-

duce the scattering amplitude f_{if} for the non-relavistic or relativistic scattering of two particles according to

$$\frac{d\sigma_{if}}{d\Omega} = \frac{k'}{k}|f_{if}|^2 \ , \tag{1.49}$$

where k and k' were defined previously as the modulus of the momentum of the initial and final state, respectively, in the center-of-mass frame. As a consequence, from Eq. (1.38) we can relate the scattering amplitude f_{if} with the two-body T-matrix as

$$f_{if} = (2\pi)^2 \left(\frac{E_1\omega_2 E_3\omega_4}{s}\right)^{\frac{1}{2}} T_{if}\ e^{i\phi} \ , \tag{1.50}$$

being ϕ an arbitrary phase. The choice $\phi = \pi$ is generally adopted, hence $f_{if} \propto -T_{if}$.

In order to introduce the partial wave scattering amplitudes a_l, we should decompose T_{if} in partial waves and, for simplicity, we explicitly treat the case of central interactions. Before performing the decomposition, we can still make one more simplification because we are only concerned with a_l coming from the elastic scattering of a meson and a baryon, so Eq. (1.50) reduces to

$$f_{if} = -(2\pi)^2 \frac{E\ \omega}{\sqrt{s}}\ T_{if} \ , \tag{1.51}$$

with E and ω being the energy of the baryon and meson, respectively.

The elastic T-matrix element $T_{if}(k, \widehat{k}\cdot\widehat{k}\,')$ (omitting spin and isospin indices for simplicity) can be written in partial waves as

$$T_{if}(k, \widehat{k}\cdot\widehat{k}\,') = \sum_{l=0}^{\infty}\sum_{m=-l}^{+l} T_l(k) Y_{lm}(\widehat{k}\,') Y^*_{lm}(\widehat{k}) \ , \tag{1.52}$$

and, therefore, a_l as

$$a_l = -(2\pi)^2 \frac{E\ \omega}{\sqrt{s}} \frac{T_l}{4\pi} \ , \tag{1.53}$$

according to Eqs. (1.46), (1.51) and (1.52).

This result is easily generalized to the case of non-central forces which mix states of different orbital angular momentum, while the total angular momentum J is a conserved quantity. In this case, one works in the $|LSJM\rangle$ basis and performs the partial wave expansion through the generalized spherical harmonics to get

$$a^J_{LS} = -(2\pi)^2 \frac{E\ \omega}{\sqrt{s}} \frac{T^J_{LS}}{4\pi} \ . \tag{1.54}$$

The method of partial waves is most useful when only a small number of partial waves contribute to the scattering, situation that arises out at low incident energies if we are not taken into account the possibility of resonance phenomena. Therefore, for the low energy case, only the $L = 0$ component survives and the previous relation of Eq. (1.53) is usually studied for the s-wave case, i.e,

$$a_{s-wave} = -(2\pi)^2 \frac{E\ \omega}{\sqrt{s}} \frac{T_{s-wave}}{4\pi} \ , \tag{1.55}$$

and, up to a sign convention, this quantity is usually referred to as *scattering length* .

1.2 The $\bar{K}N$ interaction

The study of the meson-baryon amplitude for the $\bar{K}N$ system presented in this section starts from the introduction of the main features of the Jülich $\bar{K}N$ potential in the

meson-exchange framework [Mul90]. Afterwards, the $\bar{K}N$ Lippman-Schwinger equation will be solved numerically paying attention to its coupled channel structure.

1.2.1 The Jülich $\bar{K}N$ meson-exchange potential

A succesful interpretation of the experimental data and the reliability of predictions in kaon physics requires the precise knowledge of the interaction mechanism of antikaons with nuclei. Since each theoretical model for the antikaon-nucleus interaction starts from the free antikaon-nucleon interaction adding, in a second step, medium corrections, a precise knowledge of the interaction in free space is absolutely essential.

Existing work on the $\bar{K}N$ system have constructed potentials with a certain number of free parameters determined by a fit to empirical data (see Ref. [Hen80, Brw84, Sch87, Sie88]) or parametrized the T-matrix directly (see Ref. [Kim65, Mar76, Mar81, Mar69, Dal82]). However, the poor quality of the existing $\bar{K}N$ data make very difficult a reliable interpretation of such data. More and better data would be extremely helpful, but instead of concentrating on the $\bar{K}N$ system only, a promising and theoretically appealing alternative would be to describe many different hadronic reactions using the same underlying picture and using the same calculational scheme as consistently as possible. This is the program pursued by the Jülich group. The idea is to start from the Bonn meson exchange NN interaction and apply the same scheme to other hadronic processes, like the $\bar{K}N$ interaction

The Bonn group [Mac87, Mac89] constructed a meson-exchange model of the NN interaction based on suitable meson-nucleon-nucleon and meson-nucleon-delta vertices. In addition to the one-boson exchange (OBE), it contains explicit 2π-exchange contri-

butions to be consistent with results from dispersion theory and $\pi\rho$-exchange diagrams to fit the NN data. In such a way, the fictitious σ-exchange is avoided.

The same philosophy is applied to the $\bar{K}N$ Jülich potential, starting from the same framework, meson-exchange, and using, as closely as possible, the same methods applied in the construction of the Bonn potential for NN. Furthermore, consistency with the KN system, previously obtained in Ref. [But90], is required, due to G-parity. Therefore, a field-theoretical interaction hamiltonian is constructed containing, apart from meson-nucleon-nucleon and meson-delta-nucleon couplings, additional $\bar{K}\bar{K}$-meson and $\bar{K}\bar{K}^*$-meson vertices. Therefore, the lagrangians that appear for the $\bar{K}N$ meson-exchange potential have the following structure. Let B, D denote the octet ($J^P = 1/2^+$) and the decuplet ($J^P = 3/2^+$) baryons, respectively, and S, P, V be scalar, pseudoscalar and vector mesons, respectively. Then, the lagrangians involving baryons read

$$\begin{aligned}
\mathcal{L}_{BBS} &= g_{BBS}\,\bar{\psi}_B\psi_B\;\phi_S\;, \\
\mathcal{L}_{BBP} &= g_{BBP}\,\bar{\psi}_B i\gamma^5\psi_B\;\phi_P\;, \\
\mathcal{L}_{BDP} &= \frac{g_{BDP}}{m_P}\,(\bar{\psi}_{D\mu}\psi_B + \bar{\psi}_B\psi_{D\mu})\;\partial^\mu\phi_P\;, \\
\mathcal{L}_{BDV} &= \frac{g_{BDV}}{m_V}\,i(\bar{\psi}_{D\nu}\gamma^5\gamma_\mu\psi_B - \bar{\psi}_B\gamma^5\gamma_\mu\psi_{D\nu})\;(\partial^\mu\phi_V^\nu - \partial^\nu\phi_V^\mu)\;, \\
\mathcal{L}_{BBV} &= g_{BBV}\,\bar{\psi}_B\gamma_\mu\psi_B\;\phi_V^\mu + \frac{f_{BBV}}{4m_N}\,\bar{\psi}_B\sigma_{\mu\nu}\psi_B\;(\partial^\mu\phi_V^\nu - \partial^\nu\phi_V^\mu)\;,
\end{aligned} \tag{1.56}$$

while those involving only mesons are given by

$$\begin{aligned}
\mathcal{L}_{PPS} &= g_{PPS}\,m_P\;\phi_P\;\phi_P\;\phi_S\;, \\
\mathcal{L}_{PPV} &= g_{PPV}\,\phi_P\;\partial_\mu\;\phi_P\;\phi_V^\mu\;,
\end{aligned}$$

$$\mathcal{L}_{VVP} = \frac{g_{VVP}}{m_V}\, i\, \varepsilon_{\mu\nu\tau\delta}\, \partial^\mu\, \phi_V^\nu\, \partial^\tau\, \phi_V^\delta\, \phi_P\ . \tag{1.57}$$

Furthermore, the $\bar{K}N$ interaction, in consistency with the KN one, takes into account the effect of further channels ($N\bar{K}^*$, $\Delta\bar{K}^*$, $\Delta\bar{K}$) by adding corresponding fourth-order terms to the $\bar{K}N \to \bar{K}N$ part of the potential. The difference between the interaction of kaons and antikaons with the nucleons comes from the coupled-channel structure of the $\bar{K}N$ system. Already at the $\bar{K}N$ threshold, we have a system of three coupled channels: $\bar{K}N$, $\pi\Lambda$ and $\pi\Sigma$. This coupled-channel potential introduces additional degrees of freedom without any constraints from G-parity. Their respective parameters, unless fixed by previous studies, have to be adjusted in the fitting procedure. The diagrams present in the Jülich $\bar{K}N$ meson-exchange potential are shown in Fig. 1.2.

The form factors that describe the extended hadron structure are suitably parametrized for baryon-meson-baryon vertices [Mac87, Mac89]

$$F_\alpha(\vec{q}_r^{\,2}) = \left(\frac{\Lambda_\alpha^2 - m_r^2}{\Lambda_\alpha^2 + \vec{q}_r^{\,2}}\right)^{n_\alpha}\ , \tag{1.58}$$

where Λ_α, $\vec{q}_r$ and m_r are the cutoff, momentum and mass in the vertex, respectively, and $n_\alpha = 1$ for NN and $N\Delta$ vertices while $n_\alpha = 2$ for the $N\Delta\rho$ one.

The additional form factors which appear at the meson-meson-meson vertices are also parametrized according to the same vertex structure (see Ref. [But90, Mul90]). The only exception constitutes the pole contributions where a baryon is exchanged. In order to avoid problems of convergence and singularities, a slightly different prescription

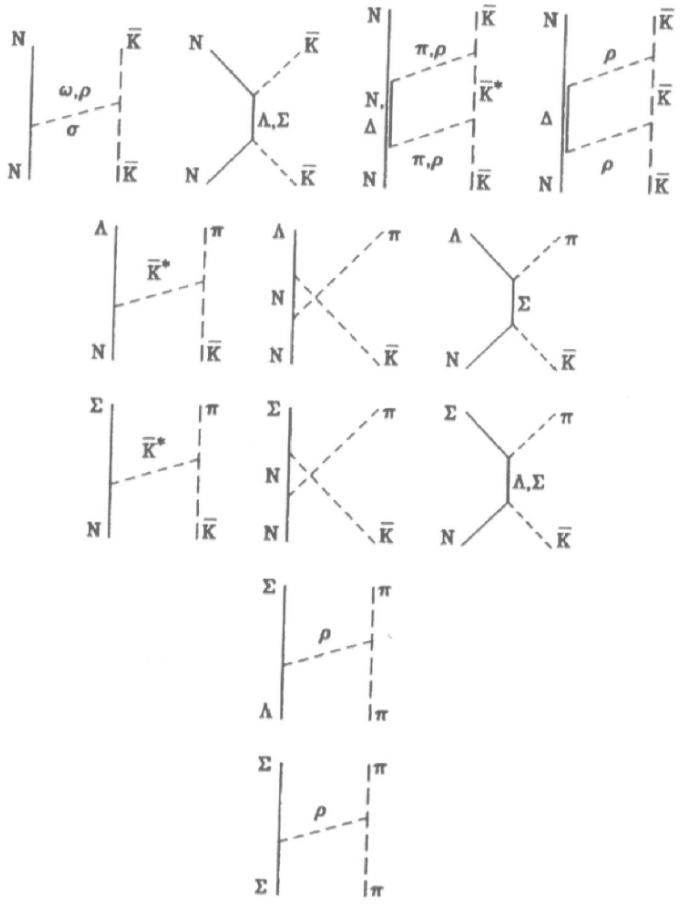

Figure 1.2: All contributions to the potential. Taken from Ref. [Mul90].

is taken (see Ref. [Mul90])

$$F_\beta(\vec{q}_r^{\,2}) = \frac{\Lambda_\beta^4 + m_r^4}{\Lambda_\beta^4 + (\vec{q}_r^{\,2})^2} \ . \tag{1.59}$$

Finally, corrections due to the Coulomb interaction are also considered.

1.2.2 The coupled $\bar{K}N$ Lippman-Schwinger equation

In this section we outline how the $\bar{K}N$ Lippman-Schwinger equation is solved numerically in a coupled channel framework, paying attention to the partial wave decompo-

sition and discussing how to treat the Lippman-Schwinger propagator singularities.

The $\bar{K}N$ scattering amplitude is obtained from the bare $\bar{K}N$ interaction derived in the meson-exchange framework, described in the previous section [Mul90]. As it was explained, the bare interaction allows for the transition from the $\bar{K}N$ to other channels, like $\pi\Sigma$ or $\pi\Lambda$, because the strong interaction connects states in which strangeness is conserved ($S = -1$). Therefore, we are confronted with a coupled channel problem. The coupling to other $S = -1$ meson-baryon states at higher energy, such as $\eta\Lambda$, $\eta\Sigma$ and $K\Xi$, not considered in the Jülich parametrization, can be thought to be embedded in the parameters of the model such as the coupling constants or the form-factor cutt-offs. The resultant meson-baryon (MB) T-matrices can be grouped in a matrix notation according to the isospin quantum number, where each box corresponds to one channel. The $\bar{K}N$ channel can have isospin $I = 0$ or $I = 1$. In the first case, it can only couple to the $\pi\Sigma$ channel and the corresponding matrix has the following structure

$$\begin{pmatrix} T_{\bar{K}N\to\bar{K}N} & T_{\pi\Sigma\to\bar{K}N} \\ T_{\bar{K}N\to\pi\Sigma} & T_{\pi\Sigma\to\pi\Sigma} \end{pmatrix} ,$$

while for $I = 1$ it can couple to both the $\pi\Sigma$ and $\pi\Lambda$ channels

$$\begin{pmatrix} T_{\bar{K}N\to\bar{K}N} & T_{\pi\Sigma\to\bar{K}N} & T_{\pi\Lambda\to\bar{K}N} \\ T_{\bar{K}N\to\pi\Sigma} & T_{\pi\Sigma\to\pi\Sigma} & T_{\pi\Lambda\to\pi\Sigma} \\ T_{\bar{K}N\to\pi\Lambda} & T_{\pi\Sigma\to\pi\Lambda} & T_{\pi\Lambda\to\pi\Lambda} \end{pmatrix} .$$

Keeping this structure in mind, each box ($\bar{K}N \leftrightarrow \bar{K}N$, $\bar{K}N \leftrightarrow \pi\Lambda$, $\bar{K}N \leftrightarrow \pi\Sigma$,

$\pi\Sigma \leftrightarrow \pi\Sigma$, $\pi\Lambda \leftrightarrow \pi\Lambda$, $\pi\Sigma \leftrightarrow \pi\Lambda$) of the T-matrix is formally given by

$$\langle M_1B_1 \mid T(\Omega) \mid M_2B_2\rangle = \langle M_1B_1 \mid V(\sqrt{s}) \mid M_2B_2\rangle$$
$$+ \sum_{M_3B_3} \langle M_1B_1 \mid V(\sqrt{s}) \mid M_3B_3\rangle \frac{1}{\Omega - E_{M_3} - E_{B_3} + i\eta} \langle M_3B_3 \mid T(\Omega) \mid M_2B_2\rangle \ . \quad (1.60)$$

In Eq. (1.60), M_i and B_i represent the possible mesons ($\bar{K}$, π) and baryons (N, Λ, Σ), respectively, and their corresponding quantum numbers such as spin, isospin, strangeness, and linear momentum. The starting energy Ω can be calculated according to $\sqrt{s} = \sqrt{\Omega^2 - \vec{P}^{\,2}}$. In the center-of-mass frame, $\Omega = \sqrt{s}$.

In order to solve the T-matrix numerically, we use the partial wave decomposition of Eq. (1.24). The total angular momentum J, its third component M, the isospin I and its third component M_I are conserved, as it is expected for strong interactions. On the other hand, the orbital angular momentum for an interacting system of a meson of $s = 0$ and baryon of $s = 1/2$ turns out to be a conserved quantity because of parity conservation.

Therefore, for a given starting energy Ω and working in the center-of-mass frame ($\vec{P} = 0$), each meson-baryon (k', k) matrix element inside one box can be written [see Eq. (1.24)]

$$\langle (M_1B_1)k'L\tfrac{1}{2}JMIM_I|T|(M_2B_2)kL\tfrac{1}{2}JMIM_I\rangle =$$
$$\langle (M_1B_1)k'L\tfrac{1}{2}JMIM_I|V|(M_2B_2)kL\tfrac{1}{2}JMIM_I\rangle +$$
$$\sum_{M_3B_3} \int dk''k''^2 \langle (M_1B_1)k'L\tfrac{1}{2}JMIM_I|V|(M_3B_3)k''L\tfrac{1}{2}JMIM_I\rangle$$
$$\times \frac{1}{\Omega - E_{B_3}(k'') - \omega_{M_3}(k'') + i\epsilon}$$
$$\times \langle (M_3B_3)k''L\tfrac{1}{2}JMIM_I|T|(M_2B_2)kL\tfrac{1}{2}JMIM_I\rangle \ . \quad (1.61)$$

In order to perform the integral over the relative momentum k'', we use the relations

$$\begin{aligned} \frac{1}{x+i\epsilon} &= \mathcal{P}\frac{1}{x} - i\pi\delta(x) \\ \delta(f(x)) &= \sum_{\substack{zeros\ x_j \\ from\ f(x)}} \frac{1}{|f'(x_j)|}\,\delta(x-x_j)\ , \end{aligned} \tag{1.62}$$

to simplify the integral

$$\begin{aligned} &\int dk\,k^2 \frac{\mathcal{N}(k)}{\Omega - E(k) - \omega(k) + i\epsilon} = \\ &\mathcal{P}\int dk\,k^2 \frac{\mathcal{N}(k)}{\Omega - E(k) - \omega(k)} - i\pi \int dk\ k^2\ \mathcal{N}(k)\ \delta(\Omega - E(k) - \omega(k)) = \\ &\mathcal{P}\int dk\,k^2 \frac{\mathcal{N}(k)}{\Omega - E(k) - \omega(k)} - i\pi \bar{k}\frac{E(\bar{k})\omega(\bar{k})}{\Omega}\mathcal{N}(\bar{k})\ , \end{aligned} \tag{1.63}$$

where $\mathcal{N}(k)$ stands for the product $\langle V\rangle \times \langle T\rangle$, and $\bar{k}$ is the momentum for which the intermediate system M_3B_3 is on the mass shell. Afterwards, we discretize the principal part having for each (k', k) element inside a box the following equation

$$\begin{aligned} &\langle (M_1B_1)k'L\tfrac{1}{2}JMIM_I|T|(M_2B_2)kL\tfrac{1}{2}JMIM_I\rangle = \\ &\langle (M_1B_1)k'L\tfrac{1}{2}JMIM_I|V|(M_2B_2)kL\tfrac{1}{2}JMIM_I\rangle + \\ &\sum_{M_3B_3}\sum_n k_n''^2 W_n \frac{1}{\Omega - E_{B_3}(k_n'') - \omega_{M_3}(k_n'')} \\ &\times\langle (M_1B_1)k'L\tfrac{1}{2}JMIM_I|V|(M_3B_3)k_n''L\tfrac{1}{2}JMIM_I\rangle \\ &\langle (M_3B_3)k_n''L\tfrac{1}{2}JMIM_I|T|(M_2B_2)kL\tfrac{1}{2}JMIM_I\rangle \\ &-i\pi\bar{k}_{M_3B_3}\frac{E_{B_3}(\bar{k}_{M_3B_3})\,\omega_{M_3}(\bar{k}_{M_3B_3})}{\Omega} \\ &\times\langle (M_1B_1)k'L\tfrac{1}{2}JMIM_I|V|(M_3B_3)\bar{k}_{M_3B_3}L\tfrac{1}{2}JMIM_I\rangle \\ &\langle (M_3B_3)\bar{k}_{M_3B_3}L\tfrac{1}{2}JMIM_I|T|(M_2B_2)kL\tfrac{1}{2}JMIM_I\rangle\ , \end{aligned} \tag{1.64}$$

where the points of the mesh (k_n) and their corresponding weights (W_n) are defined by a logarithmic mapping

$$k_n = C \ln\left(\frac{1+x_n}{1-x_n}\right), \quad W_n = C\frac{2}{1-x_n^2}v_n \ , \tag{1.65}$$

where x_n are Gaussian points chosen from 0 to 1 and v_n are their corresponding weights. Note that formally the range of the mesh points goes from 0 to ∞. The value of the arbitrary constant C is chosen to optimize the numerical integration. In practice, we fit a maximum momentum value k_{max} dictated by the range in momentum space of the meson-baryon interaction and define $C = k_{max}/\ln\left(\frac{1+x_p}{1-x_p}\right)$, being x_p the last point of the Gaussian mesh.

Defining $\mathcal{B}(k_n'')^{M_3B_3}$ as

$$\mathcal{B}(k_n'')^{M_3B_3}\begin{cases} \dfrac{k_n''^2 W_n}{\Omega - E_{B_3}(k_n'') - \omega_{M_3}(k_n'')} & \text{for } n \leq N, \\ -i\pi\bar{k}_{M_3B_3}\dfrac{E_{B_3}(\bar{k}_{M_3B_3})\,\omega_{M_3}(\bar{k}_{M_3B_3})}{\Omega} & \text{for } n = N+1, \end{cases} \ , \tag{1.66}$$

we can write Eq.(1.64) as

$$\begin{aligned} &\langle (M_1B_1)\vec{P}k'L\tfrac{1}{2}JMIM_I|T|(M_2B_2)\vec{P}kL\tfrac{1}{2}JMIM_I\rangle = \\ &\langle (M_1B_1)\vec{P}k'L\tfrac{1}{2}JMIM_I|V|(M_2B_2)\vec{P}kL\tfrac{1}{2}JMIM_I\rangle + \\ &\sum_{M_3B_3}\sum_{n=1}^{n=N+1}\mathcal{B}(k_n'',\vec{P})^{M_3B_3}\times\langle (M_1B_1)\vec{P}k'L\tfrac{1}{2}JMIM_I|V|(M_3B_3)\vec{P}k_n''L\tfrac{1}{2}JMIM_I\rangle \\ &\times\langle (M_3B_3)\vec{P}k_n''L\tfrac{1}{2}JMIM_I|T|(M_2B_2)\vec{P}kL\tfrac{1}{2}JMIM_I\rangle \ . \end{aligned} \tag{1.67}$$

where $\vec{P} = 0$.

Then, we can construct the $N_{\bar{K}N}N_{\pi\Sigma} \times N_{\bar{K}N}N_{\pi\Sigma}$ ($N_{\bar{K}N}N_{\pi\Sigma}N_{\pi\Lambda} \times N_{\bar{K}N}N_{\pi\Sigma}N_{\pi\Lambda}$) matrix for $I = 0$ ($I = 1$).

The dimension is determined by an off-shell finite momentum mesh with $N_{\bar{K}N}$, $N_{\pi\Sigma}$ or $N_{\pi\Lambda}$ components. In case that the pole in the Lippman-Schwinger propagator for the $\bar{K}N$, $\pi\Sigma$ or $\pi\Lambda$ intermediate channel is achieved for a given energy parameter Ω, an extra row and column are introduced in the corresponding box and the sum will run to $N+1$, being $k_{N+1}^{M_3B_3} \equiv \bar{k}_{M_3B_3}$ as one can easily seen in the previous expressions [Eqs. (1.64) and (1.66)].

In order to solve the T-matrix, we use the inversion method that in compact notation reads

$$\begin{aligned} T &= V \; + \; V \; \frac{1}{E} \; T \\ \left(1 - \; V \; \frac{1}{E}\right) \; T &= V \\ T &= \left(1 - \; V \; \frac{1}{E}\right)^{-1} \; V. \end{aligned} \tag{1.68}$$

Finally, let us make some remarks about the singular propagator of the Lippman-Schwinger equation and the solution of possible numerical instabilities. In order to properly treat numerically the poles which may appear in the propagator when the starting energy Ω is larger than the minimum energy of the intermediate states, it is common to substract numerically and add analytically the integral

$$\bar{k} \; E(\bar{k}) \; \omega(\bar{k}) \; \langle k_j|V|\bar{k}\rangle \; \langle \bar{k}|T|k_i\rangle \; \mathcal{P} \int dk \; \frac{k}{E(k) \; \omega(k) \; (\Omega - E(k) - \omega(k))} \; , \tag{1.69}$$

which has the same behaviour as the integral of the propagator around the pole.

Spin and isospin indices have been omitted for simplicity. Consequently, $\mathcal{B}(k_n'')^{M_3B_3}$ of Eq.(1.66) will contain two more terms for $n = N+1$

$$\mathcal{B}(k_n'')^{M_3B_3} \begin{cases} \dfrac{k_n''^2 W_n}{\Omega - E_{B_3}(k_n'') - \omega_{M_3}(k_n'')} & \text{for } n \leq N, \\ \bar{k}_{M_3B_3}\, E_{B_3}(\bar{k}_{M_3B_3})\, \omega_{M_3}(\bar{k}_{M_3B_3}) & \\ \times \left(-\Gamma_q^{M_3B_3} + \dfrac{1}{\Omega} \ln \left| \dfrac{\Omega}{m_{B_3} + m_{M_3}} - 1 \right| - i\dfrac{\pi}{\Omega} \right) & \text{for } n = N+1, \end{cases}$$

with $\Gamma_q^{M_3B_3}$ equals to

$$\Gamma_q^{M_3B_3} = \sum_{n=1}^{N} \frac{W_n q_n}{E_{B_3}(q_n)\ \omega_{M_3}(q_n)\ (\Omega - E_{B_3}(q_n) - \omega_{M_3}(q_n))}\ . \tag{1.70}$$

An alternative and often complementary way of cancelling the instabilities is to choose a mesh symmetrically around the position of the pole.

1.3 Free space scattering observables

In this last section we present the results obtained by solving the $\bar{K}N$ interaction or T-matrix, using the $\bar{K}N$ Jülich potential derived in the meson-exchange framework [Mul90]. In particular, we will show the $\Lambda(1405)$ mass spectrum and the total cross sections for $K^-p \to K^-p, \bar{K}^0n, \pi^0\Lambda, \pi^0\Sigma^0, \pi^+\Sigma^-, \pi^-\Sigma^+$, comparing them to the experimental results. At the end, we will make some comments about the short-commings of the $\bar{K}N$ Jülich potential that arise when the s-wave scattering amplitudes and various threshold ratios are compared to their experimental values.

1.3.1 The $\Lambda(1405)$ resonance

We start by commenting on the free space observables like the $\Lambda(1405)$ mass spectrum. The dynamics of the $\bar{K}N$ interaction is particularly rich due to the presence of the strange resonance $\Lambda(1405)$, which has isospin 0 and $J^P = (1/2)^-$ and lies only 27 MeV below the $\bar{K}N$ threshold. There is still debate whether this state has to be interpreted either as a genuine 3-quark resonance or as a quasibound $\bar{K}N$ state. This resonance is observed in the mass distribution of $\pi\Sigma$ in reactions such as $\pi^- p \to K\Sigma\pi$ [Tho73] and $K^- p \to \Sigma^*(1660), \Sigma^*(1660) \to \Lambda(1405)\pi^+, \Lambda(1405) \to \Sigma\pi$ [Hem85].

In order to obtain the mass distribution [Fla76], one has to recover the expression of the total cross section for a reaction process of two initial particles going to a three particle final state so as to study a reaction of the type $\pi^- p \to K\Sigma\pi$. According to Eq.(1.34) and integrating the final momenta, the cross section for this system reads

$$\sigma_{\pi p \to K\Sigma\pi} = (2\pi)^4 \int \frac{d^3p_\Sigma}{(2\pi)^3} \int \frac{d^3p_{\pi(f)}}{(2\pi)^3} \int \frac{d^3p_K}{(2\pi)^3} \frac{m_\Sigma}{E_\Sigma} \frac{1}{2\omega_{\pi(f)}} \frac{1}{2\omega_K}$$
$$\times \frac{1}{v_{rel}} \frac{m_p}{E_p} \frac{1}{2\omega_{\pi(i)}} \, \delta^{(4)}(p_K + p_\Sigma + p_{\pi(f)} - p_{\pi(i)} - p_p) \, |T_{\pi p \to K\Sigma\pi}|^2 \, . \qquad (1.71)$$

In this last equation, $1/(2\omega)$ and M/E are the normalization factors for the meson (π,K) and baryon (p,Σ) fields, v_{rel} is the relative velocity of the colliding particles, and the four-momentum conservation shows up in the delta function $\delta^{(4)}(p_K + p_\Sigma + p_{\pi(f)} - p_{\pi(i)} - p_p)$. The $T_{\pi p \to K\Sigma\pi}$ can be evaluated as

$$T_{\pi p \to K\Sigma\pi} = \mathcal{C} T_{\pi\Sigma \to \pi\Sigma} \approx \mathcal{C}' T^0_{\pi\Sigma \to \pi\Sigma} \, , \qquad (1.72)$$

where it is assumed that the main contribution to $T_{\pi p \to K\Sigma\pi}$ comes from the isospin zero

component of the on-shell T-matrix for the $\pi\Sigma \to \pi\Sigma$ channel. Introducing

$$\int dm_\alpha \; 2m_\alpha \; \delta(m_\alpha^2 - (p_\Sigma + p_{\pi(f)})^2) \tag{1.73}$$

in Eq.(1.71), where m_α is the invariant mass of the $\Sigma\pi$ system, and defining

$$\vec{P} = \vec{p}_\Sigma + \vec{p}_{\pi(f)}; \qquad 2\vec{p} = \vec{p}_\Sigma - \vec{p}_{\pi(f)} \; , \tag{1.74}$$

we can write $\sigma_{\pi p \to K\Sigma\pi} \equiv \sigma$ as

$$\begin{aligned} \sigma \approx \mathcal{C}'(2\pi)^4 \int dm_\alpha \; 2m_\alpha \int \frac{d^3P}{(2\pi)^3} \int \frac{d^3p}{(2\pi)^3} \int \frac{d^3p_K}{(2\pi)^3} \frac{m_\Sigma}{E_\Sigma} \frac{1}{2\omega_{\pi(f)}} \frac{1}{2\omega_K} \frac{1}{v_{rel}} \frac{m_p}{E_p} \frac{1}{2\omega_{\pi(i)}} \\ \times \; \delta^{(4)}(p_K + p_\Sigma + p_{\pi(f)} - p_{\pi(i)} - p_p) \; \delta(m_\alpha^2 - (E_\Sigma + \omega_{\pi(f)})^2 + \vec{P}^2) \; |T^0_{\pi\Sigma\to\pi\Sigma}|^2 \; . \end{aligned} \tag{1.75}$$

Performing $\int d^3p_K$, it follows that

$$(2\pi)^4 \; \delta^{(4)}(p_K + p_\Sigma + p_{\pi(f)} - p_{\pi(i)} - p_p) \to (2\pi) \; \delta(\sqrt{s} - (E_\Sigma + \omega_{\pi(f)}) - \omega_K), \tag{1.76}$$

with $\sqrt{s} = E_p + \omega_{\pi(i)}$. If we now use $\delta(\sqrt{s} - (E_\Sigma + \omega_{\pi(f)}) - \omega_K)$ for writing $\delta(m_\alpha^2 - (\sqrt{s} - \omega_K)^2 + \vec{P}^2)$, we have for the mass distribution $d\sigma/dm_\alpha$

$$\begin{aligned} \frac{d\sigma}{dm_\alpha} \approx \mathcal{C}' 2m_\alpha \int \frac{d^3P}{(2\pi)^3} \int \frac{d^3p}{(2\pi)^3} \frac{m_\Sigma}{E_\Sigma} \frac{1}{2\omega_{\pi(f)}} \frac{1}{2\omega_K} \frac{1}{v_{rel}} \frac{m_p}{E_p} \frac{1}{2\omega_{\pi(i)}} \\ \times (2\pi) \; \delta(\sqrt{s} - (E_\Sigma + \omega_{\pi(f)}) - \omega_K) \; \delta(m_\alpha^2 - (\sqrt{s} - \omega_K)^2 + \vec{P}^2) \; |T^0_{\pi\Sigma\to\pi\Sigma}|^2 \; . \end{aligned} \tag{1.77}$$

Finally, the integral over $\vec{P}$ and $\vec{p}$ will be performed, taking into account the possible dependences in $\vec{P}$ or $\vec{p}$. Assuming that we are sitting in the πp center-of-mass frame

and using $\delta(m_\alpha^2 - (\sqrt{s} - \omega_K(\vec{P}))^2 + \vec{P}^2)$, $\int d\vec{P}$ will give

$$\frac{d\sigma}{dm_\alpha} \approx \mathcal{C}' \frac{1}{2\pi^2} \frac{1}{2\sqrt{s}} \; |\vec{P}| \; m_\alpha \int \frac{d^3p}{(2\pi)^3} \frac{m_\Sigma}{E_\Sigma} \frac{1}{2\omega_{\pi(f)}}$$
$$\times \frac{1}{v_{rel}} \frac{m_p}{E_p} \frac{1}{2\omega_{\pi(i)}} (2\pi) \; \delta(\sqrt{s} - (E_\Sigma + \omega_{\pi(f)}) - \omega_K(\vec{P})) \; |T^0_{\pi\Sigma\to\pi\Sigma}|^2 \; , \qquad (1.78)$$

where we have shown explicitly the dependence of ω_K in $\vec{P}$. The three particle final state can be interpreted as a "$\pi\Sigma$ particle " of invariant mass m_α that moves with a momentum $\vec{P}$ and a kaon that moves with $-\vec{P}$, being $\sqrt{s}$ the invariant center-of-mass energy. Therefore

$$|\vec{P}| = \frac{\lambda^{\frac{1}{2}}(s, m_K^2, m_\alpha^2)}{2\sqrt{s}}. \qquad (1.79)$$

Because of Lorentz invariance, we can evaluate the integral $\int d^3p$ in the frame where the $\pi\Sigma$ system is at rest, i.e, $E_\Sigma(p_{cm}), \omega_\pi(p_{cm})$. Therefore, one gets

$$\frac{d\sigma}{dm_\alpha} \propto \lambda^{\frac{1}{2}}(s, m_K^2, m_\alpha^2) |T^0_{\pi\Sigma\to\pi\Sigma}|^2 p_{cm} \; , \qquad (1.80)$$

as we perform the integral over $\vec{p}$. This expression shows that the mass distribution of the $\pi\Sigma$ system can be calculated as

$$\frac{d\sigma}{dm_\alpha} \propto |T^0_{\pi\Sigma\to\pi\Sigma}|^2 p_{cm} \; , \qquad (1.81)$$

because the "triangle function" $\lambda^{\frac{1}{2}}(s, m_K^2, m_\alpha^2)$ is a very smooth function of m_α^2.

The study of the mass distribution of $\pi\Sigma$ state according to [Fla76] reflects the $\Lambda(1405)$ resonance. The $\Lambda(1405)$ appears dynamically in our calculation without readjusting any parameter of the Jülich potential. In Fig. 1.3 we show the $\Lambda(1405)$ mass spectrum, calculated with the $L = 0$ and $I = 0$ component of $T_{\pi\Sigma\to\pi\Sigma}$ (solid line) and

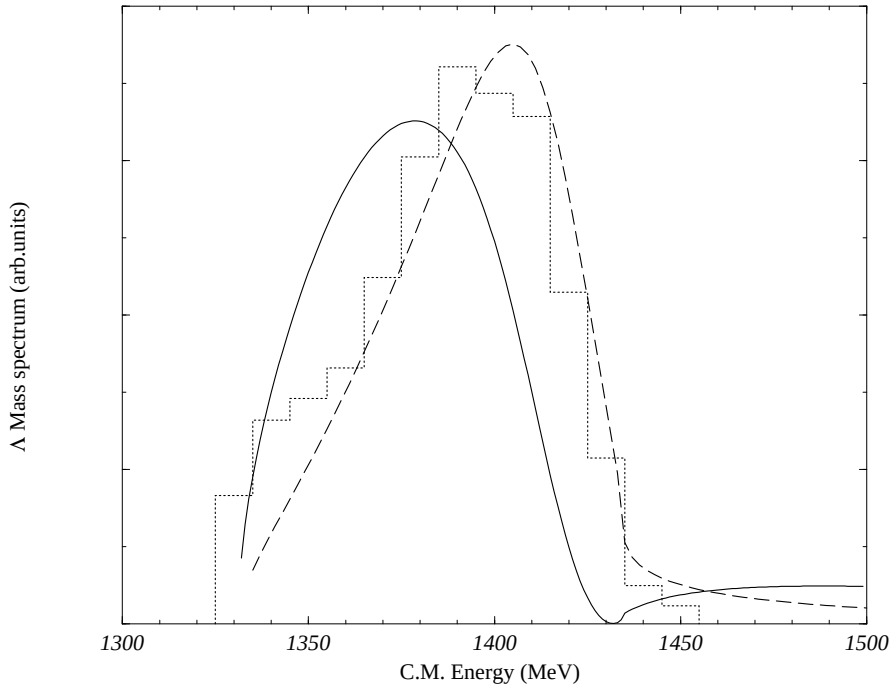

Figure 1.3: $\Lambda(1405)$ mass spectrum. The experimental histogram [Hem85] is compared to the invariant mass distribution $|T_{\pi\Sigma\to\pi\Sigma}|^2 p_{cm}$ (solid line) and $|T_{\bar{K}N\to\pi\Sigma}|^2 p_{cm}$ (long-dashed line).

also using the $T_{\bar{K}N\to\pi\Sigma}$ amplitude (long-dashed line) since it can also contribute to generate the final $\pi\Sigma$ mass distribution.

Comparing to the experimental $\Lambda(1405)$ spectrum, also displayed in Fig. 1.3, it appears that the Jülich $\bar{K}N$ model will build up the resonance from a linear combination of both $T_{\pi\Sigma\to\pi\Sigma}$ and $T_{\bar{K}N\to\pi\Sigma}$ amplitudes. We note, however, that there is a discrepancy between the $\Lambda(1405)$ mass spectrum displayed in the $\bar{K}N$ Jülich potential reference [Mul90] and the one shown here, since the $T_{\pi\Sigma\to\pi\Sigma}$ amplitude alone seems to reproduce the $\Lambda(1405)$ mass spectrum in the previous reference. This discrepancy may come from differences between the Jülich potential reported in the original reference and the one used in this thesis.

1.3.2 The K^-p elastic and inelastic cross sections

The theoretical predictions of the Jülich $\bar{K}N$ interaction for the K^-p scattering cross sections, defined in Eqs. (1.38) and (1.39), can also be compared to data. We pay attention to the cross sections for $K^-p \to K^-p, \bar{K}^0n, \pi^0\Lambda, \pi^0\Sigma^0, \pi^+\Sigma^-, \pi^-\Sigma^+$ at low energies for the K^- laboratory momenta between 50 and 200 MeV/c. This momentum range is largely dominated by the $L = 0$ partial wave.

Due to the fact that we have been using the isospin formalism in which $\pi, \bar{K}, N, \Sigma$ stand for (π^+, π^0, π^-), $(\bar{K}^0, K^-)$, (p, n) and $(\Sigma^+, \Sigma^0, \Sigma^-)$, respectively, we shall construct the physical amplitudes from the isospin states $|I\ M_I\rangle$ as

$$
\begin{aligned}
|K^-p\rangle &= -\frac{1}{\sqrt{2}}|1,0\rangle + \frac{1}{\sqrt{2}}|0,0\rangle \\
|\bar{K}^0n\rangle &= \frac{1}{\sqrt{2}}|1,0\rangle + \frac{1}{\sqrt{2}}|0,0\rangle \\
|\pi^0\Sigma^0\rangle &= \sqrt{\frac{2}{3}}|2,0\rangle - \frac{1}{\sqrt{3}}|0,0\rangle \\
|\pi^-\Sigma^+\rangle &= -\frac{1}{\sqrt{6}}|2,0\rangle + \frac{1}{\sqrt{2}}|1,0\rangle - \frac{1}{\sqrt{3}}|0,0\rangle \\
|\pi^+\Sigma^-\rangle &= -\frac{1}{\sqrt{6}}|2,0\rangle - \frac{1}{\sqrt{2}}|1,0\rangle - \frac{1}{\sqrt{3}}|0,0\rangle \\
|\pi\Lambda\rangle &= |1,0\rangle\ ,
\end{aligned}
\tag{1.82}
$$

where we use the phase convention $|\pi^+\rangle = -|1,1\rangle$,$|K^-\rangle = -|1/2,-1/2\rangle$ and $|\Sigma^+\rangle = -|1,1\rangle$, consistent with the structure of the octet of $1/2^+$ baryons.

Therefore,

$$
\begin{aligned}
T_{K^-p\to K^-p} &= \frac{1}{2}T^{I=1}_{\bar{K}N\to\bar{K}N} + \frac{1}{2}T^{I=0}_{\bar{K}N\to\bar{K}N} \\
T_{K^-p\to\bar{K}^0n} &= -\frac{1}{2}T^{I=1}_{\bar{K}N\to\bar{K}N} + \frac{1}{2}T^{I=0}_{\bar{K}N\to\bar{K}N} \\
T_{K^-p\to\pi^0\Sigma^0} &= -\frac{1}{\sqrt{6}}T^{I=0}_{\bar{K}N\to\pi\Sigma} \\
T_{K^-p\to\pi^-\Sigma^+} &= -\frac{1}{2}T^{I=1}_{\bar{K}N\to\pi\Sigma} - \frac{1}{\sqrt{6}}T^{I=0}_{\bar{K}N\to\pi\Sigma} \\
T_{K^-p\to\pi^+\Sigma^-} &= \frac{1}{2}T^{I=1}_{\bar{K}N\to\pi\Sigma} - \frac{1}{\sqrt{6}}T^{I=0}_{\bar{K}N\to\pi\Sigma} \\
T_{K^-p\to\pi^0\Lambda} &= -\frac{1}{\sqrt{2}}T^{I=1}_{\bar{K}N\to\pi\Lambda} \ .
\end{aligned}
\tag{1.83}
$$

In Figs. 1.4, 1.5 and 1.6, we display the obtained total cross sections for the different physical states as a function of the K^- momentum in the laboratory frame, comparing them with the available low-energy scattering data [Hum62, Sak65, Kim65, Kim66, Kit66, Cib82, Eva83]. In those figures, the dashed line corresponds to only use the s-wave component of the T-matrix in the cross sections, while the solid one includes higher partial waves up to $L = 5$. In particular, the elastic cross-section $K^-p \to K^-p$ and the inelastic process $K^-p \to \bar{K}^0n$ are shown in Fig. 1.4. The cusp that appears in the $K^-p \to K^-p$ cross section for $p_{\rm lab}$ below 100 MeV/c corresponds to the opening of the $\bar{K}^0n$ channel. However, the use of the average masses for $\bar{K}$, N, π and Σ in the evaluation of the amplitudes using the isospin basis makes the cusp show up below the physical value $p_{\rm lab} \sim 90$ MeV/c.

With regard to the effect of higher partial waves, one can see that at low momentum (below 100 MeV/c), the $L \leq 5$ and $L = 0$ lines fall on the same curve. This is an expected behaviour because the $L = 0$ component or s-wave is the most important

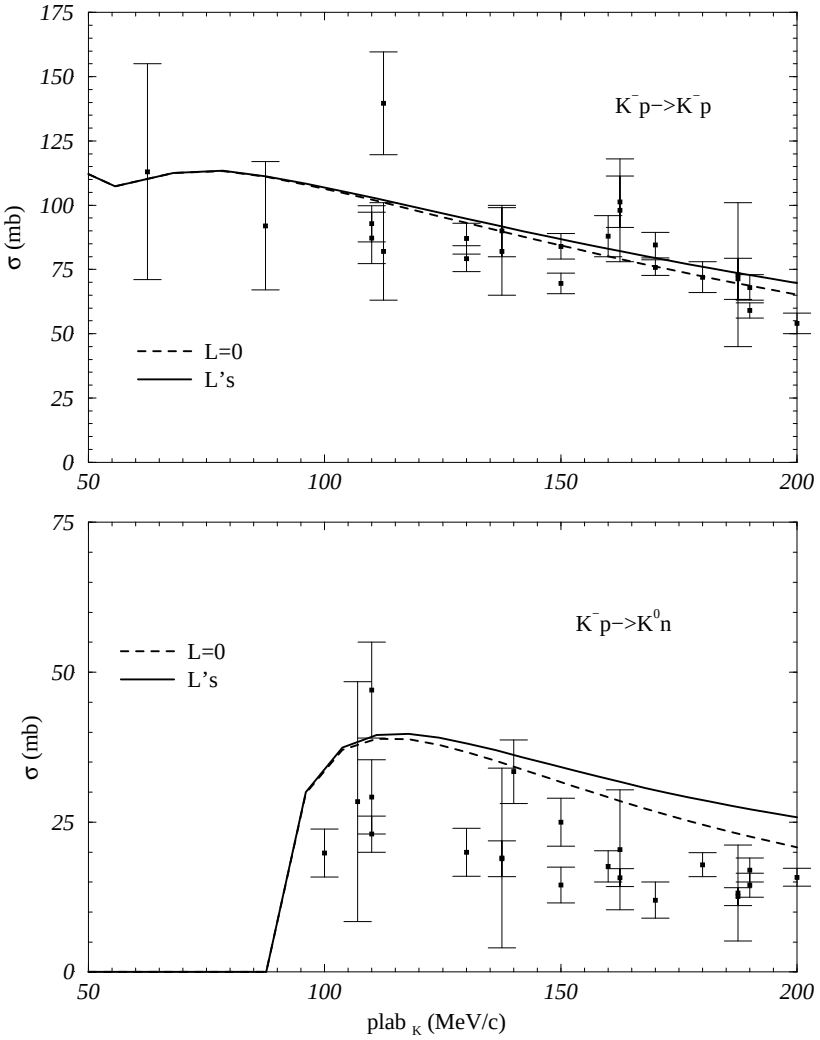

Figure 1.4: $K^-p \to K^-p$ and $K^-p \to \bar{K}^0 n$ cross sections as a function of the K^- momentum in the laboratory frame. Experimental data taken from [Hum62, Sak65, Kim65, Kim66, Kit66, Cib82, Eva83].

contribution to the scattering processes at low energies. The effect of partial waves beyond s-wave lies around 5 mb for $p_{\rm lab} = 200$ MeV/c for all the reaction processes. As expected, the higher the momentum is, the bigger the difference is between the solid and dashed lines.

The agreement with the total elastic and inelastic K^-p scattering cross section

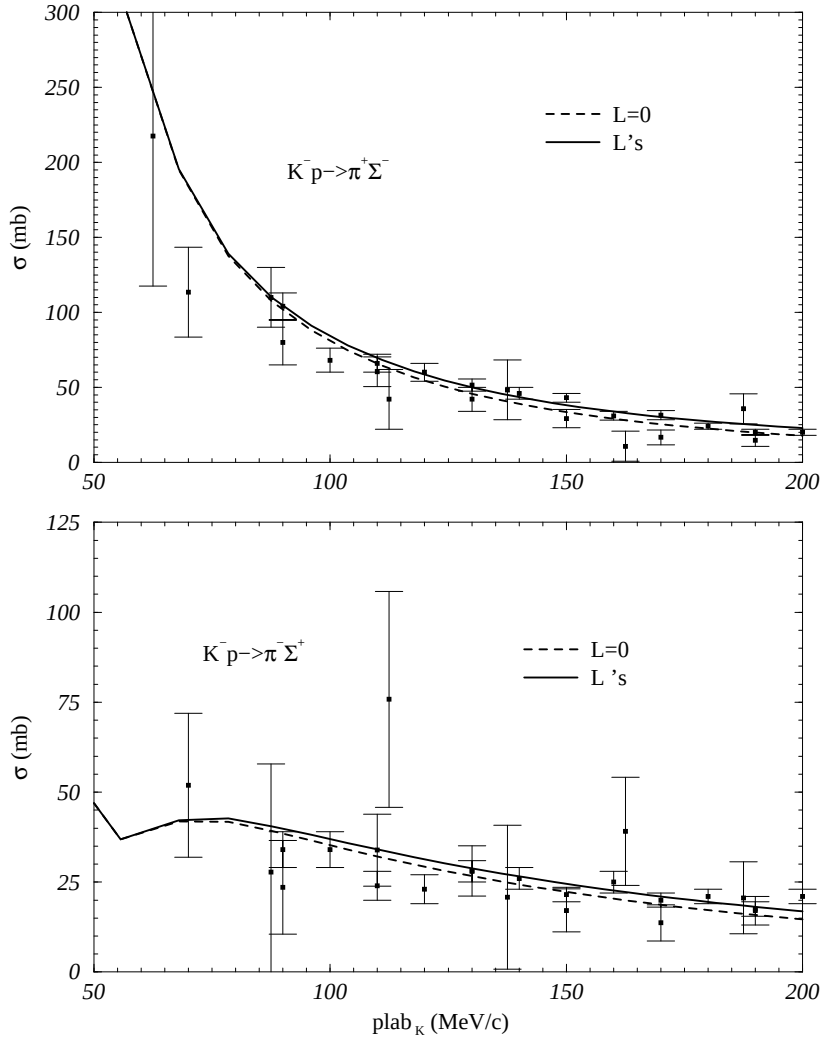

Figure 1.5: $K^-p \to \pi^+\Sigma^-$ and $K^-p \to \pi^-\Sigma^+$ cross sections as a function of the K^- momentum in the laboratory frame. Experimental data taken from [Hum62, Sak65, Kim65, Kim66, Kit66, Cib82, Eva83].

data is quite satisfactory. Nevertheless, the calculation tends to overestimate the experimental values, especially for the $K^-p \to \pi^0\Lambda$ system (lower panel of Fig. 1.6). This channel couples only to $I = 1$ and, as a consequence, this could be an indication that the Jülich $\bar{K}N$ potential could have some deficiencies for $I = 1$. The $I = 0$ component of the cross sections seems to present a better agreement with the data if we look at

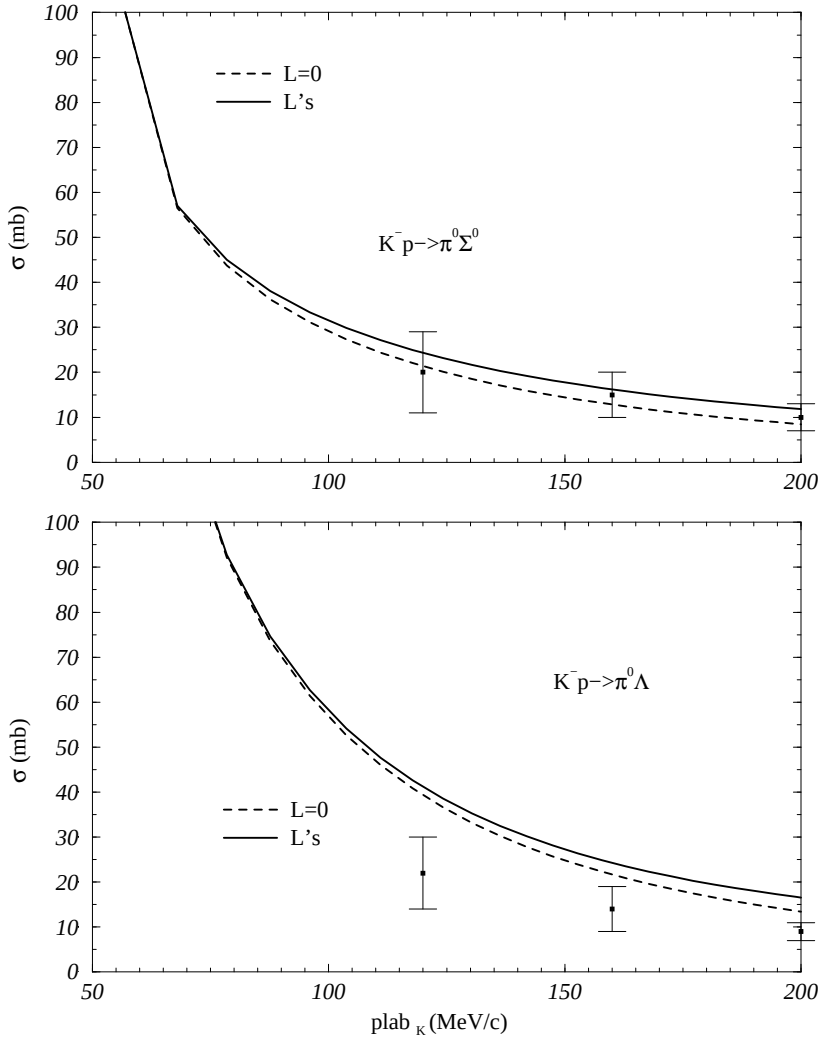

Figure 1.6: $K^-p \to \pi^0\Sigma^0$ and $K^-p \to \pi^0\Lambda^0$ cross sections as a function of the K^- momentum in the laboratory frame. Experimental data taken from [Hum62, Sak65, Kim65, Kim66, Kit66, Cib82, Eva83].

the upper panel of the same figure. Here it is displayed the $K^-p \to \pi^0\Sigma^0$ cross section which only couples to $I = 0$. The scattering amplitudes at threshold could be a helpful tool for investigating the different isospin components of T-matrix at low energies. The s-wave scattering amplitudes will be studied in the next section together with some experimental ratios.

1.3.3 The s-wave $\bar{K}N$ scattering amplitudes and threshold ratios

An important check of any $\bar{K}N$ interaction in s-wave is provided by the isospin scattering amplitudes [Mar81]

$$\begin{aligned} a^{I=0} &= -1.70 + i0.68 \text{ fm} \\ a^{I=1} &= 0.37 + i0.60 \text{ fm} , \end{aligned}$$

and a few rather accurate branching ratios at threshold [Hum62, Sak65, Tov71, Now78]:

$$\begin{aligned} \gamma &= \frac{\Gamma(K^- p \to \pi^+ \Sigma^-)}{\Gamma(K^- p \to \pi^- \Sigma^+)} = 2.36 \pm 0.04 \\ R_c &= \frac{\Gamma(K^- p \to \text{charged particles})}{\Gamma(K^- p \to \text{all})} = 0.664 \pm 0.011 \\ R_n &= \frac{\Gamma(K^- p \to \pi^0 \Lambda)}{\Gamma(K^- p \to \text{all neutral states})} = 0.189 \pm 0.015 . \end{aligned}$$

The results obtained from the Jülich $\bar{K}N$ potential at the $K^- p$ threshold energy of 1431.95 MeV are

$$\begin{aligned} a^{I=0} &= -1.71 + i1.28 \text{ fm} \\ a^{I=1} &= 1.07 + i0.71 \text{ fm} , \\ \gamma &= 5.778 \\ R_c &= 0.600 \\ R_n &= 0.447 . \end{aligned}$$

These results are a reflection of the deficiencies present in the $L = 0$ component of this $\bar{K}N$ interaction. The $a^{I=1}$ component is overestimated and the ratios are not in agreement with the experimental ones. In addition, while a relevant contribution to the $L = 1$ component of the Jülich $\bar{K}N$ interaction comes from the Λ and Σ pole diagrams, the role of the $\Sigma^*(1385)$, which is closer to the $\bar{K}N$ threshold, has not been included.

In spite of the shortcomings of the Jülich $\bar{K}N$ interaction, one can still explore the importance of the various partial waves when in-medium $\bar{K}$ effects are introduced. The aim of the next chapter is devoted to this end. However, one has to keep in mind that a more accurate $\bar{K}N$ interaction in all partial waves is needed. It would be interesting to include the s-wave scattering amplitudes and threshold branching ratios in the fitting procedure of the Jülich interaction, since they are very sensitive to the parameters of the model. A small fine tunning of the parameters of the present Jülich $\bar{K}N$ interaction would probably improve dramatically the agreement with all low energy data. This effort, however, goes beyond the purpose of the present work.

Chapter 2

Medium effects on the $\bar{K}N$ interaction

In this chapter we study the interaction of the $\bar{K}$ meson embedded in symmetric nuclear matter using the meson-exchange Jülich $\bar{K}N$ interaction [Mul90] described in the previous chapter. This chapter is organized as follows. Section 2.1 is devoted to introduce the in-medium $\bar{K}N$ interaction as the starting-point for determining the $\bar{K}$ self-energy in Section 2.2. In Section 2.3, two self-consistent schemes to construct the $\bar{K}$ self-energy are presented. The effect of higher partial waves of the $\bar{K}N$ interaction, beyond $L = 0$, and the momentum dependence of the $\bar{K}$ self-energy are studied. Finally, in Section 2.4 we focus our attention on the influence of the in-medium pion properties on the $\bar{K}$ self-energy.

2.1 The properties of $\bar{K}$ in the nuclear medium

In this section the dynamics of the $\bar{K}N$ interaction in the medium is carefully considered which in turn determines the most adequate way to obtain the optical potential felt by a $\bar{K}$ meson embedded in nuclear matter.

The $\bar{K}$ optical potential is evaluated for nuclear symmetric matter by means of the integral

$$U_{\bar{K}}(k_{\bar{K}},\rho) = \nu \int \frac{d^3k}{(2\pi)^3}\, n(\vec{k},\rho)\; \mathsf{T}_{\bar{K}N}(k_{\bar{K}},\vec{k},\rho)\;, \tag{2.1}$$

which stands for the sum of the in-medium $\bar{K}N$ interaction $\mathsf{T}_{\bar{K}N}$ over the Fermi sea of nucleons $n(\vec{k},\rho)$, being ν the spin-isospin degeneracy factor of nuclear symmetric matter. Therefore the main concern is to decide the most realistic manner of introducing medium effects on the $\bar{K}N$ interaction.

The $\bar{K}N$ amplitude at low energies is dominated by the $\Lambda(1405)$ resonance, which in the approaches of Refs. [Kai95, Ose98] is interpreted as an isospin $I = 0$ quasi-bound K^-p state. The $\Lambda(1405)$ resonance is slightly below the K^-p threshold leading to a repulsive K^-p amplitude in free space. The first step towards determining the $\bar{K}$ optical potential would be to identify the $\bar{K}N$ amplitude in the medium with the scattering matrix $T_{\bar{K}N}$ including medium effects afterwards. Actually, theoretical evaluations of the potential felt by a particle in a nucleus usually start from the *low-density theorem or impulse approximation* [Dov71, Huf72, Huf75] that would consider the interaction of a $\bar{K}$ meson in medium to have the form $\overline{T}_{\bar{K}N}\rho$, being $\overline{T}_{\bar{K}N}$ the elementary scattering amplitude of the antikaon with the nucleons averaged over isospin and the Fermi motion of the nucleons. This approach would lead to a repulsive $\bar{K}$ optical potential due to the presence of the resonance.

However, kaonic data suggest that, even at a small fraction of the normal nuclear matter density, the K^- feels a strongly attractive potential. This implies a rapid transition from a repulsive $\bar{K}N$ interaction to an attractive one as density increases and, therefore, a microscopic study of the $\bar{K}$ properties in the medium cannot be done in terms of the simple $\overline{T}_{\bar{K}N}\rho$ approximation. It is necessary to consider the density dependence of the in-medium $\bar{K}N$ interaction.

One source of density dependence comes from the *Pauli principle*, which prevents the scattering to intermediate nucleon states below the Fermi momentum. This effect was proved to be very important in [Koc94, Waa96a, Waa96b, Waa97]. Indeed, forcing the intermediate nucleon states to be on top of a Fermi sea costs more energy, and the net effect is a shift to higher energies of the $\Lambda(1405)$ resonance. This shift produces the expected attractive $\bar{K}$ optical potential already seen at very small densities. However, if the $\bar{K}$ optical potential acquires a negative value because of the Pauli effects, then it costs less energy to produce the $\Lambda(1405)$ resonance, hence producing a shift of the $\bar{K}N$ amplitude towards lower energies. A *self-consistent* evaluation becomes then necessary as shown in [Lut98a, Lut98b], where it was found that the consideration of the $\bar{K}$ self-energy together with the Pauli blocking on the nucleons left the position of the $\Lambda(1405)$ resonance basically unchanged.

In this thesis we incorporate microscopically all the previous medium effects on the calculation of the $\bar{K}$ optical potential by building the in-medium $\bar{K}N$ interaction in a Brueckner-type many-body theory, as it was done long time ago to study kaonic atoms [Alb76].

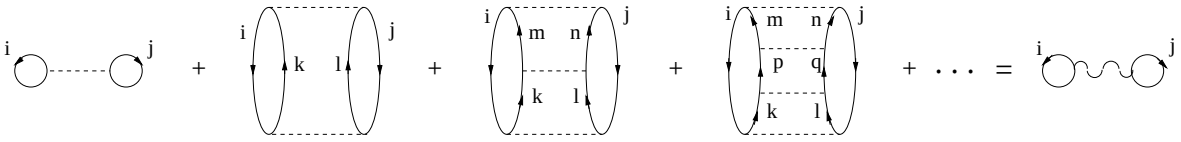

Figure 2.1: Illustration of the summation of the infinite sequence of ladder diagrams to obtain the G-matrix (diagram on the right-hand side). Taken from [Vid00].

2.1.1 The Brueckner-Hartree-Fock approach for the $\bar{K}N$ interaction

We start by presenting the basic ideas that lie behind the Brueckner-Goldstone theory for nuclear matter [Bru50s, Day67, Gol57] in order to apply them to the in-medium $\bar{K}N$ interaction.

This theory for nuclear matter is based on the principle that, equivalent to the treatment of nucleon-nucleon scattering, each matrix element of V should be substituted by an infinite series which takes into account the two-body interaction to all orders called *reaction matrix* or *G-matrix*.

Fig. 2.1 displays the infinite sequence of ladder diagrams. The summation of the sequence, starting from an antisymmetric nucleon-nucleon state $|N_i N_j\rangle$ lying below the Fermi level F, which evolves towards the same final two-body state, reads

$$\frac{1}{2}\sum_{i,j\leq F}\langle N_i N_j|\left(V + V\sum_{k,l>F}\frac{|N_k N_l\rangle\langle N_k N_l|}{\varepsilon_i+\varepsilon_j-\varepsilon_k-\varepsilon_l}V + V\sum_{k,l>F}\frac{|N_k N_l\rangle\langle N_k N_l|}{\varepsilon_i+\varepsilon_j-\varepsilon_k-\varepsilon_l}V\sum_{m,n>F}\frac{|N_m N_n\rangle\langle N_m N_n|}{\varepsilon_i+\varepsilon_j-\varepsilon_m-\varepsilon_n}V + \ldots\right)|N_i N_j\rangle_{\mathcal{A}}\ , \quad (2.2)$$

where ε is the nucleon energy. This previous summation defines the reaction matrix

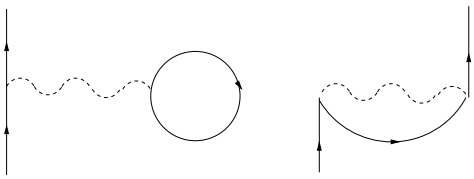

Figure 2.2: The Brueckner-Hartree-Fock approach for the nucleon optical potential.

$G(\omega)$ as

$$G(\omega) = V + V\frac{Q}{\omega - H_0}V + V\frac{Q}{\omega - H_0}V\frac{Q}{\omega - H_0}V + \dots \ , \tag{2.3}$$

where $\omega = \varepsilon_i + \varepsilon_j$ is the "starting energy" and

$$\frac{Q}{\omega - H_0} = \sum_{p,q>F} \frac{|N_p N_q\rangle\langle N_p N_q|}{\omega - \varepsilon_p - \varepsilon_q} \ , \tag{2.4}$$

with Q being the Pauli operator that anhilates a two-nucleon state unless both nucleons are above the Fermi sea whereas $\omega - H_0$ is the energy difference between the initial and intermediate state. The expansion of Eq. (2.3) is equivalent to the integral equation

$$G(\omega) = V + V\frac{Q}{\omega - H_0}G(\omega) \ , \tag{2.5}$$

which is known as the *Bethe-Goldstone equation.* For values of ω larger than the sum of the energies of the intermediate states, the propagator of the Bethe-Goldstone equation may become singular and then, it is necessary to add a quantity $i\eta$ in the energy denominator to properly treat the propagator.

The next step is to perform a perturbative series in terms of G, the so-called *Brueckner-(Bethe)-Goldstone expansion* or *hole-line expansion* (see Ref.[Raj60s]), in order to compute the energy of the nuclear system, or to obtain the potential felt by a nucleon in the presence of a Fermi sea of nucleons.

The leading term of this perturbation series is the *Brueckner-Hartree-Fock approximation* (BHF) (see Fig.2.2), due to its analogy with the Hartree-Fock (HF) approximation. In this approach, the potential felt by a nucleon inside a Fermi sea of nucleons can be calculated according to

$$U_{N_i}^{BHF} = \mathrm{Re}\sum_{j\leq F}\langle N_i N_j|G(\omega=\varepsilon_i+\varepsilon_j)|N_i N_j\rangle_{\mathcal{A}} \ . \tag{2.6}$$

The difference with respect to the HF approach arises out because the matrix elements V are substituted by the reaction matrix G, understood as an effective interaction between two particles in $|N_i\rangle$ and $|N_j\rangle$ states.

In analogy with the nuclear matter problem, the G-matrix turns out to be the in-medium $\bar{K}N$ interaction and, therefore, we can write the $\bar{K}$ optical potential in correspondence with the Brueckner-Hartree-Fock approximation for the nucleon optical potential as

$$U_{\bar{K}} = \sum_{j\leq F}\langle \bar{K}N_j|G(\omega)|\bar{K}N_j\rangle \ . \tag{2.7}$$

where the two body state stands for an antikaon $\bar{K}$ and a nucleon N. More explicitly, the former equation reads:

$$U_{\bar{K}}(k_{\bar{K}},\rho) = \nu \int \frac{d^3k}{(2\pi)^3}\ n(\vec{k},\rho)\ G_{\bar{K}N}(k_{\bar{K}},\vec{k},\rho) \ , \tag{2.8}$$

which is the expression introduced at the beginning of the section.

2.2 In-medium $\bar{K}N$ interaction and the $\bar{K}$ self-energy

In this section we present the formalism to obtain the self-energy of a $\bar{K}$ meson embedded in infinite symmetric nuclear matter. This self-energy accounts for the interaction of the $\bar{K}$ meson with the nucleons and its calculation requires the knowledge of the in-medium $\bar{K}N$ interaction, which is described by a G-matrix. The medium effects incorporated in this G-matrix include the Pauli blocking on the nucleons in the intermediate states as well as the dressing of the $\bar{K}$ meson and the different baryons. We explore different ways of dressing the $\bar{K}N$ intermediate state in solving the G-matrix, which define the type of self-consistency of the calculation giving rise to the different approaches discussed in the results' section.

2.2.1 In-medium $\bar{K}N$ interaction

The $\bar{K}N$ amplitude in the nuclear medium or G-matrix is obtained from the bare $\bar{K}N$ interaction derived in the meson exchange framework [Mul90], according to the same procedure followed in the derivation of the T-matrix. As it was seen in Sec. 1.2.2, we are confronted with a coupled channel problem as the bare interaction allows transitions from the $\bar{K}N$ channel to the $\pi\Sigma$ and $\pi\Lambda$ channels, conserving strangeness $S = -1$. This coupled structure is solved by building meson-baryon matrices according to isospin $I = 0$

$$\begin{pmatrix} G_{\bar{K}N\to\bar{K}N} & G_{\pi\Sigma\to\bar{K}N} \\ G_{\bar{K}N\to\pi\Sigma} & G_{\pi\Sigma\to\pi\Sigma} \end{pmatrix},$$

or $I = 1$

$$\begin{pmatrix} G_{\bar{K}N\to\bar{K}N} & G_{\pi\Sigma\to\bar{K}N} & G_{\pi\Lambda\to\bar{K}N} \\ G_{\bar{K}N\to\pi\Sigma} & G_{\pi\Sigma\to\pi\Sigma} & G_{\pi\Lambda\to\pi\Sigma} \\ G_{\bar{K}N\to\pi\Lambda} & G_{\pi\Sigma\to\pi\Lambda} & G_{\pi\Lambda\to\pi\Lambda} \end{pmatrix} .$$

As it was done previously for the T-matrix, we solve the G-matrix equation by first doing a partial wave decomposition. In the Sec. 1.1.1.1 of Chapter 1, it was shown that the propagator of the T-matrix equation is diagonal either in the physical basis or in the partial wave one and, therefore, the partial wave decomposition of the T-matrix turns out to be very simple [see Eq. (1.24)].

Nevertheless, complications can arise when the medium effects are implemented. The propagator in the G-matrix equation, $D_{MB}^{med}(\vec{k},\vec{P}) \equiv Q(\vec{k},\vec{P})/E(\omega,\vec{k},\vec{P})$, contains the information on the medium. The quantity $Q(\vec{k},\vec{P})$ stands for the Pauli operator, permitting only intermediate nucleon states compatible with the Pauli principle. The Pauli operator together with the dressing of the intermediate states in the energy denominator $E(\omega,\vec{k},\vec{P})$ are the two sources of medium effects. In this chapter, we are interested in symmetric nuclear matter and, therefore, the isospin/spin symmetry is fulfilled, still allowing us to write the propagator according to Eq. (1.23). Moreover, in order to simplify the numerical calculation of the G-matrix, it has become a usual technique to perform an angle average of the propagator.

The idea is to replace $D_{MB}^{med}(\vec{k},\vec{P}) = Q(\vec{k},\vec{P})/E(\omega,\vec{k},\vec{P})$ by a function $\overline{D}_{MB}^{med}(k,P) = \overline{Q}(k,P)/\overline{E}(\omega,k,P)$ independent of the angle between $\vec{P}$ and $\vec{k}$. As a consequence, the integral over the spherical harmonics in Eq. (1.23) gives $\delta_{LL'}$, $\delta_{M_L M'_L}$, and we obtain a

similar expression to Eq. (1.24) for the G-matrix equation

$$\begin{aligned}\langle (M_1B_1);k'|G^{LJI}(P,\Omega)|(M_2B_2);k\rangle \quad &= \langle (M_1B_1);k'|V^{LJI}(\sqrt{s})|(M_2B_2);k\rangle \\ &+ \sum_{M_3B_3}\int k''^2dk''\langle (M_1B_1);k'|V^{LJI}(\sqrt{s})|(M_3B_3);k''\rangle \\ &\times \frac{\overline{Q}_{M_3B_3}(k'',P)}{\Omega-\sqrt{M_{B_3}^2+\widetilde{k_{B_3}^2}}-\sqrt{M_{M_3}^2+\widetilde{k_{M_3}^2}}-U_{B_3}(\widetilde{k_{B_3}^2})-U_{M_3}(\widetilde{k_{M_3}^2})+i\epsilon} \\ &\times\langle (M_3B_3);k''|G^{LJI}(P,\Omega)|(M_2B_2);k\rangle \ , \end{aligned} \tag{2.9}$$

where the variables k, k', k'' and L denote relative momenta and orbital momentum, respectively, while P is the center-of-mass momentum. The starting energy Ω is related to the invariant center-of-mass energy by means of $\sqrt{s}=\sqrt{\Omega^2-\vec{P}^{\,2}}$. The functions $\widetilde{k_B^2}$ and $\widetilde{k_M^2}$ are, respectively, the square of the momentum of the baryon and that of the meson in the intermediate states, averaged over the angle between the total momentum $\vec{P}$ and the relative momentum $\vec{k}''$ (see the definitions in appendix A)

$$\widetilde{k_B^2}(k'',P) = k''^2+\left(\frac{m_B}{m_M+m_B}\right)^2P^2 \ , \tag{2.10}$$

$$\widetilde{k_M^2}(k'',P) = k''^2+\left(\frac{m_M}{m_M+m_B}\right)^2P^2 \ . \tag{2.11}$$

The angle average of the Pauli operator, $\overline{Q}_{M_3B_3}(k'',P)$, is shown explicitly in Appendix A and differs from unity only in the case of the $\bar{K}N$ channel.

The total angular momentum and isospin are denoted by J and I, respectively. For each J, two values of orbital angular momentum, $L=J+1/2$ and $L=J-1/2$, are allowed. However, due to parity conservation, the interaction can not mix these two states and, as a consequence, the orbital angular momentum is also a conserved

quantity, as already seen for the T-matrix.

The former equation for the G-matrix has to be considered together with a prescription for the single-particle energies of all the mesons and baryons participating in the reaction and in the intermediate states. These energies can be written as

$$E_{M_i(B_i)}(k) = \sqrt{k^2 + m^2_{M_i(B_i)}} + U_{M_i(B_i)}(k, E^{qp}_{M_i(B_i)}) \ , \tag{2.12}$$

where $U_{M_i(B_i)}$ is the single-particle potential of each meson (baryon) calculated at the real quasiparticle energy $E^{qp}_{M_i(B_i)}$, obtained by solving the following equation

$$E^{qp}_{M_i(B_i)}(k) = \sqrt{k^2 + m^2_{M_i(B_i)}} + \mathrm{Re}\, U_{M_i(B_i)}(k, E^{qp}_{M_i(B_i)}) \ . \tag{2.13}$$

As a first approach, we have considered the single-particle potential for the $\bar{K}$ meson and all baryons. Although the dressing of pions plays a crucial role in the determination of the in-medium $\bar{K}N$ interaction, we first study the main features of the $\bar{K}N$ interaction in the nuclear medium without dressing them. We consider in detail the dressing of pions afterwards.

For the Λ and Σ hyperons we use the simplified form

$$U_{\Lambda,\Sigma}(\rho) = -30\frac{\rho}{\rho_0} \ , \tag{2.14}$$

where ρ_0 is the saturation nuclear matter density while for nucleons we take the density

ρ (fm^{-3})	α (MeV)	β (MeV)	Λ (fm^{-1})
0.1	4.76	-62.3	2.86
0.15	12.9	-82.5	2.63
0.2	27.7	-102	2.61
0.3	72.8	-138	3.07
0.4	176	-211	4.31
0.5	332	-311	6.00

Table 2.1: Parameters for the nucleon single particle potential of Eq. (2.15).

dependent parametrization [Wir88]

$$U_N(\rho, k) = \alpha(\rho) + \frac{\beta(\rho)}{1 + \left[\frac{k}{\Lambda(\rho)}\right]^2} , \tag{2.15}$$

that was fitted to the single-particle potentials obtained from variational calculations using realistic NN interactions. The density-dependent real parameters $\alpha(\rho)$, $\beta(\rho)$ and $\Lambda(\rho)$ are shown in Table 2.1. The zero momentum nucleon potential at $\rho = \rho_0$ amounts to -70 MeV.

In the Brueckner-Hartree-Fock approach, the $\bar{K}$ single-particle potential is schematically given by

$$U_{\bar{K}}(k, E^{qp}_{\bar{K}}) = \sum_{N \leq F} \langle \bar{K}N \mid G_{\bar{K}N \to \bar{K}N}(\Omega = E^{qp}_N + E^{qp}_{\bar{K}}) \mid \bar{K}N \rangle , \tag{2.16}$$

where the summation over nucleon states is limited by the nucleon Fermi momentum. The explicit calculation of $U_{\bar{K}}$ will be discussed in the next subsection.

At the required $\bar{K}$ energies, the G-matrix in the above equation becomes complex due to the possibility of $\bar{K}N$ decaying into the $\pi\Sigma$, $\pi\Lambda$ channels. As a consequence,

the potential $U_{\bar{K}}$ is also a complex quantity. However, the influence of the medium on the G-matrix is studied by considering different approaches that have been used in the literature: (a) the real quasiparticle energy defined in Eq. (2.13) and (b) the complex $E_{\bar{K}}$ defined in Eq. (2.12) which also contains the imaginary part of $U_{\bar{K}}$ calculated at $E^{qp}_{\bar{K}}$.

At this point and before entering into the explicit calculation of the $\bar{K}$ single-particle energy, we should make some remarks about the numerical instabilities that may appear in the function $\overline{D}^{med}_{MB}$ when the energy parameter Ω is large enough to put on the mass shell the intermediate states, as we did for the Lippman-Schwinger equation. For the G-matrix, the integral over $\overline{D}^{med}_{MB}$ in a schematic form reads

$$\int k''^2 dk'' \frac{\langle k'|V|k''\rangle\ \overline{Q}(k'')\ \langle k''|G|k\rangle}{\Omega - \varepsilon_B(k'') - \omega_M(k'') - U_B(k'') - U_M(k'') + i\epsilon}\ , \tag{2.17}$$

keeping only the momentum dependence which is relevant for determining appropiately the solution to the instabilities and with ε_B (U_B) being the free spectrum (optical potential or single-particle potential) of baryons, and ω_M (U_M) the free spectrum (optical potential) of mesons, respectively.

For the $\pi\Sigma$ and $\pi\Lambda$ intermediate states, it is easily seen that using the density parametrization for Λ and Σ described in Eq. (2.14) and fixing $U_\pi = 0$, we can redefine Ω as $\Omega - U_{\Lambda,\Sigma}(\rho)$ obtaining an expression that has the same kind of behaviour around the pole structure as Eq. (1.69). Therefore, the singular propagator is treated in the same way as done before for the T-matrix.

However, complications show up for the $\bar{K}N$ state, depending on the approach used. If we take the complex $U_{\bar{K}}$, no singularities appear on the real Ω-axis and the

integral is well-behaved in general. However, we need to reformulate the solution to the singular propagator when only the real part of $U_{\bar{K}}$ is kept.

In this case, the delta function in Eq. (2.17) is written as

$$-i\pi k''^{\,2}\delta(\Omega-\varepsilon_N(k'')-\omega_{\bar{K}}(k'')-U_N(k'')-U_{\bar{K}}(k'')) = -i\pi\frac{\bar{k}_{\bar{K}N}}{\mathcal{C}(\bar{k}_{\bar{K}N})}\delta(k''-\bar{k}_{\bar{K}N})$$

$$\mathcal{C}(\bar{k}_{\bar{K}N}) = \left|\frac{\varepsilon_N(\bar{k}_{\bar{K}N})+\omega_{\bar{K}}(\bar{k}_{\bar{K}N})}{\varepsilon_N(\bar{k}_{\bar{K}N})\omega_{\bar{K}}(\bar{k}_{\bar{K}N})}+\frac{1}{\bar{k}_{\bar{K}N}}\frac{dU_N(k'')}{dk''}\Big)_{\bar{k}_{\bar{K}N}}+\frac{1}{\bar{k}_{\bar{K}N}}\frac{dU_{\bar{K}}(k'')}{dk''}\Big)_{\bar{k}_{\bar{K}N}}\right| . \quad (2.18)$$

Therefore, once the integral is performed, one realizes that the imaginary contribution to Eq. (2.9) is located in the $N+1th$ column and row of the $\bar{K}N$ box. To overcome the singularity and similarly to what was done for the T-matrix, one should add analytically and substract numerically the following expression in the $N+1th$ column/row

$$\begin{aligned}&\bar{k}_{\bar{K}N}\varepsilon_N(\bar{k}_{\bar{K}N})\omega_{\bar{K}}(\bar{k}_{\bar{K}N})\langle k'|V|\bar{k}_{\bar{K}N}\rangle\ \overline{Q}_{\bar{K}N}(\bar{k}_{\bar{K}N})\ \langle\bar{k}_{\bar{K}N}|G|k\rangle\\ &\times\lim_{k''\to\bar{k}_{\bar{K}N}}\frac{\widetilde{E}-\varepsilon_N(k'')-\omega_{\bar{K}}(k'')}{\Omega-\varepsilon_N(k'')-\omega_{\bar{K}}(k'')-U_N(k'')-U_{\bar{K}}(k'')}\\ &\times\mathcal{P}\int dk''\frac{k''}{\varepsilon_N(k'')\omega_{\bar{K}}(k'')(\widetilde{E}-\varepsilon_N(k'')-\omega_{\bar{K}}(k''))}\ ,\end{aligned} \quad (2.19)$$

with $\widetilde{E}=\varepsilon_N(\bar{k}_{\bar{K}N})+\omega_{\bar{K}}(\bar{k}_{\bar{K}N})$. This expression has the same behaviour around the $\bar{K}N$ pole as Eq. (2.17).

Therefore, in order to solve numerically the G-matrix similarly to Eq. (1.67), we substitute $B(k_n'')^{M_3B_3}$ of Eqs. (1.66) and (1.70) by $B(k_n'')^{M_3B_3}_{med}$, defined as follows. For

the $\pi\Sigma$ and $\pi\Lambda$ intermediate states, we have

$$\mathcal{B}(k_n'')^{\pi Y}_{med} \begin{cases} \dfrac{k_n''^2 W_n}{\Omega - \varepsilon_Y(k_n'') - \omega_\pi(k_n'') - U_Y(\rho)} & \text{for } n \leq N, \\ \left(-\Gamma_q^{\pi Y} + \dfrac{1}{\overline{\Omega}} \ln \left| \dfrac{\overline{\Omega}}{m_Y + m_\pi} - 1 \right| - i\dfrac{\pi}{\overline{\Omega}}\right) \bar{k}_{\pi Y}\ \varepsilon_Y(\bar{k}_{\pi Y})\ \omega_\pi(\bar{k}_{\pi Y}) & \text{for } n = N+1\ , \end{cases}$$

with Y denoting the hyperons (Λ or Σ), $\overline{\Omega} = \Omega - U_Y(\rho)$ and $\Gamma_q^{\pi Y}$ being

$$\Gamma_q^{\pi Y} = \sum_{n=1}^{N} \frac{W_n q_n}{\varepsilon_Y(q_n)\ \omega_\pi(q_n)\ (\overline{\Omega} - \varepsilon_Y(q_n) - \omega_\pi(q_n))}\ . \tag{2.20}$$

For the $\bar{K}N$ intermediate state, there are two possibilities. If we include the imaginary part in $U_{\bar{K}}$, then no extra column/row is needed and

$$\mathcal{B}(k_n'')^{\bar{K}N}_{med} = \frac{k_n''^2\ W_n\ \overline{Q}_{\bar{K}N}(k_n'')}{\Omega - \varepsilon_N(k_n'') - \omega_{\bar{K}}(k_n'') - U_N(k_n'') - \mathrm{Re}U_{\bar{K}}(k_n'') - i\ \mathrm{Im}U_{\bar{K}}(k_n'')} \quad n \leq N \tag{2.21}$$

On the other hand, if $\mathrm{Im}U_{\bar{K}} = 0$

$$\mathcal{B}(k_n'')^{\bar{K}N}_{med} \begin{cases} \dfrac{k_n''^2 W_n\ \overline{Q}_{\bar{K}N}(k_n'')}{\Omega - \varepsilon_N(k_n'') - \omega_{\bar{K}}(k_n'') - U_N(k_n'') - \mathrm{Re}U_{\bar{K}}(k_n'')} & \text{for } n \leq N, \\ \bar{k}_{\bar{K}N}\ \varepsilon_N(\bar{k}_{\bar{K}N})\ \omega_{\bar{K}}(\bar{k}_{\bar{K}N}) \overline{Q}_{\bar{K}N}(\bar{k}_{\bar{K}N}) & \\ \times \left(-\Gamma_q^{\bar{K}N} + \Upsilon \times \dfrac{\varepsilon_N(\bar{k}_{\bar{K}N})\ \omega_{\bar{K}}(\bar{k}_{\bar{K}N})}{\widetilde{E}} \ln \left| \dfrac{\widetilde{E}}{m_N + m_{\bar{K}}} - 1 \right| - i\dfrac{\pi}{\mathcal{C}(\bar{k}_{\bar{K}N})}\right) & \text{for } n = N+1, \end{cases}$$

with $\Gamma_q^{\bar{K}N}$ being

$$\Gamma_q^{\bar{K}N} = \Upsilon \times \sum_{n=1}^{N} \frac{W_n q_n}{\varepsilon_N(q_n)\ \omega_{\bar{K}}(q_n)\ (\Omega - \varepsilon_N(q_n) - \omega_{\bar{K}}(q_n))} ,$$

and

$$\Upsilon = \lim_{k'' \to \bar{k}_{\bar{K}N}} \frac{\widetilde{E} - \varepsilon_N(k'') - \omega_{\bar{K}}(k'')}{\Omega - \varepsilon_N(k'') - \omega_{\bar{K}}(k'') - U_N(k'') - U_{\bar{K}}(k'')} . \tag{2.22}$$

2.2.2 $\bar{K}$ single-particle energy

By using the partial wave decomposition of the G-matrix, the Brueckner-Hartree-Fock approximation to the single-particle potential of a $\bar{K}$ meson embedded in a Fermi sea of nucleons [Eq. (2.16)] becomes (see Appendix B)

$$\begin{aligned} U_{\bar{K}}(k_{\bar{K}}, E_{\bar{K}}^{qp}(k_{\bar{K}})) &= \frac{1}{2}\sum_{LJI}(2J+1)(2I+1)(1+\xi)^3 \int_0^{k_{max}} k^2 dk f(k, k_{\bar{K}}) \\ &\times \langle (\bar{K}N); k | G^{LJI}(\overline{P^2}, E_{\bar{K}}^{qp}(k_{\bar{K}}) + E_N^{qp}(\overline{k_N^2})) | (\bar{K}N); k \rangle , \end{aligned} \tag{2.23}$$

where the weight function $f(k, k_{\bar{K}})$ is given by (see Appendix C),

$$f(k, k_{\bar{K}}) = \begin{cases} 1 & \text{for } k \leq \frac{k_F - \xi k_{\bar{K}}}{1+\xi}, \\ 0 & \text{for } |\xi k_{\bar{K}} - (1+\xi)k| > k_F, \\ \dfrac{{k_F}^2 - [\xi k_{\bar{K}} - (1+\xi)k]^2}{4\xi(1+\xi)k_{\bar{K}}k} & \text{otherwise,} \end{cases} \tag{2.24}$$

with $\xi = \dfrac{m_N}{m_{\bar{K}}}$ and k_F the Fermi momentum. The magnitude of the relative momentum k is constrained by

$$k_{max} = \frac{k_F + \xi k_{\bar{K}}}{1+\xi} . \tag{2.25}$$

This weight function corresponds to the analytical integral over the angle between the external $\bar{K}$ momentum in the lab system, $\vec{k}_{\bar{K}}$, and the $\bar{K}N$ relative momentum, $\vec{k}$. This integral can be performed analytically after having eliminated the angular dependence of the G-matrix by using angle averages $\overline{P^2}$ and $\overline{k_N^2}$ for the center-of-mass and nucleon momenta, respectively (see appendix D for details).

After self-consistency for the on-shell value $U_{\bar{K}}(k_{\bar{K}}, E^{qp}_{\bar{K}})$ is achieved, one can obtain the complete energy dependence of the self-energy $\Pi_{\bar{K}}(k_{\bar{K}}, \omega)$,

$$\Pi_{\bar{K}}(k_{\bar{K}}, \omega) = 2\sqrt{k^2_{\bar{K}} + m^2_{\bar{K}}}\, U_{\bar{K}}(k_{\bar{K}}, \omega) \ , \tag{2.26}$$

by replacing $E^{qp}_{\bar{K}}$ in Eq. (2.23) by ω. This self-energy can then be used to determine the $\bar{K}$ single-particle propagator in the medium,

$$D_{\bar{K}}(k_{\bar{K}}, \omega) = \frac{1}{\omega^2 - k^2_{\bar{K}} - m^2_{\bar{K}} - 2\sqrt{k^2_{\bar{K}} + m^2_{\bar{K}}} U_{\bar{K}}(k_{\bar{K}}, \omega)} \ , \tag{2.27}$$

and the corresponding spectral density

$$S_{\bar{K}}(k_{\bar{K}}, \omega) = -\frac{1}{\pi} \mathrm{Im}\, D_{\bar{K}}(k_{\bar{K}}, \omega) \ . \tag{2.28}$$

In the two schemes discussed here, only the value of $U_{\bar{K}}$ at the quasiparticle energy $\omega = E^{qp}_{\mathrm{K}}$ is determined self-consistently. This amounts to take, in the subsequent iterations leading to self-consistency, the so-called "quasiparticle" approximation to

the $\bar{K}$ propagator

$$D^{qp}_{\bar{K}}(k_{\bar{K}},\omega) = \frac{1}{\omega^2 - k^2_{\bar{K}} - m^2_{\bar{K}} - 2\sqrt{k^2_{\bar{K}} + m^2_{\bar{K}}}\,U_{\bar{K}}(k_{\bar{K}}, E^{qp}_{\bar{K}})}\ , \tag{2.29}$$

which gives rise to a simplified spectral strength

$$S^{qp}_{\bar{K}}(k_{\bar{K}},\omega) = \tag{2.30}$$
$$-\frac{1}{\pi}\frac{2\sqrt{k^2_{\bar{K}} + m^2_{\bar{K}}}\,\mathrm{Im}\,U_{\bar{K}}(k_{\bar{K}}, E^{qp}_{\bar{K}})}{\mid \omega^2 - k^2_{\bar{K}} - m^2_{\bar{K}} - 2\sqrt{k^2_{\bar{K}} + m^2_{\bar{K}}}\,\mathrm{Re}\,U_{\bar{K}}(k_{\bar{K}}, E^{qp}_{\bar{K}}) \mid^2 + \mid 2\sqrt{k^2_{\bar{K}} + m^2_{\bar{K}}}\,\mathrm{Im}\,U_{\bar{K}}(k_{\bar{K}}, E^{qp}_{\bar{K}}) \mid^2}\ .$$

The location and width of the peak in this distribution are determined, respectively, by the real and imaginary parts of $U_{\bar{K}}(k_{\bar{K}}, E^{qp}_{\bar{K}})$.

We note that if only the real part of the $U_{\bar{K}}$ is retained in the self-consistent scheme, as done for instance in Ref. [Aka02], the $\bar{K}$ spectral distribution reduces to a δ-function at the quasiparticle energy. This is what we refer as the approach (a), while the approach (b) considers a spectral function of the type (2.30) built up with the full complex optical potential at the quasiparticle energy. Although this last scheme still represents a simplification with respect to the more sophisticate scheme followed in Refs. [Ram00, Lut98a], where the full energy dependence of the $\bar{K}$ self-energy is self-consistently determined, hence the $\bar{K}$ propagator is that of Eq. (2.27), the approximation of Eq. (2.29) is sufficiently good for the studies that are carried out in this chapter. Moreover, once self-consistency is achieved for the quasiparticle energy, one can calculate $U_{\bar{K}}(k_{\bar{K}},\omega)$ as a function of ω and derive, through Eqs. (2.27) and (2.28), the fine details of the actual strength distribution of the $\bar{K}$ meson.

2.3 In-medium results for the $\bar{K}N$ system

We start this section by discussing the most characteristic modification of the $\bar{K}N$ amplitude, which is obtained when the Pauli blocking on the intermediate nucleons is incorporated. The real and imaginary parts of the resulting in-medium $\bar{K}N$ amplitudes for a total momentum $\mid \vec{k}_{\bar{K}} + \vec{k}_N \mid = 0$ are shown in Fig. 2.3 as functions of the invariant center-of-mass energy, for three different densities: $\rho = 0$ (dotted lines), $\rho = \rho_0/2$ (dot-dashed lines), and $\rho = \rho_0$ (solid lines), with $\rho_0 = 0.17$ fm^{-3} being the saturation density of nuclear matter. We clearly see, as noticed already by all earlier microscopic calculations, the repulsive effect on the resonance produced by having moved the threshold of intermediate allowed $\bar{K}N$ states to higher energies, as a result of Pauli blocking acting on the nucleon.

Clearly, this shift of the resonance changes the $\bar{K}N$ scattering amplitude at threshold ($\sim$ 1432 MeV) from being repulsive in free space to being attractive in the medium. Since this effect is intimately connected with the strong energy dependence of the $\bar{K}N$ amplitude, important changes can be expected from a self-consistent incorporation of the $\bar{K}$ properties on the $\bar{K}N$ G-matrix, as already noted by Lutz [Lut98a] and confirmed in Ref. [Ram00].

This type of self-consistent calculations are also common in Brueckner-Hartree-Fock studies of the NN interaction, where it is costumary to take the nucleon single-particle energies as real quantities. This amounts to disregard the imaginary part of the in-medium NN amplitude in the calculation of the single-particle energy for nucleons above the Fermi momentum. We have attempted a similar type of approximate scheme for the $\bar{K}$ meson, the so-called approach (a), although in this case the $\bar{K}N$ amplitude

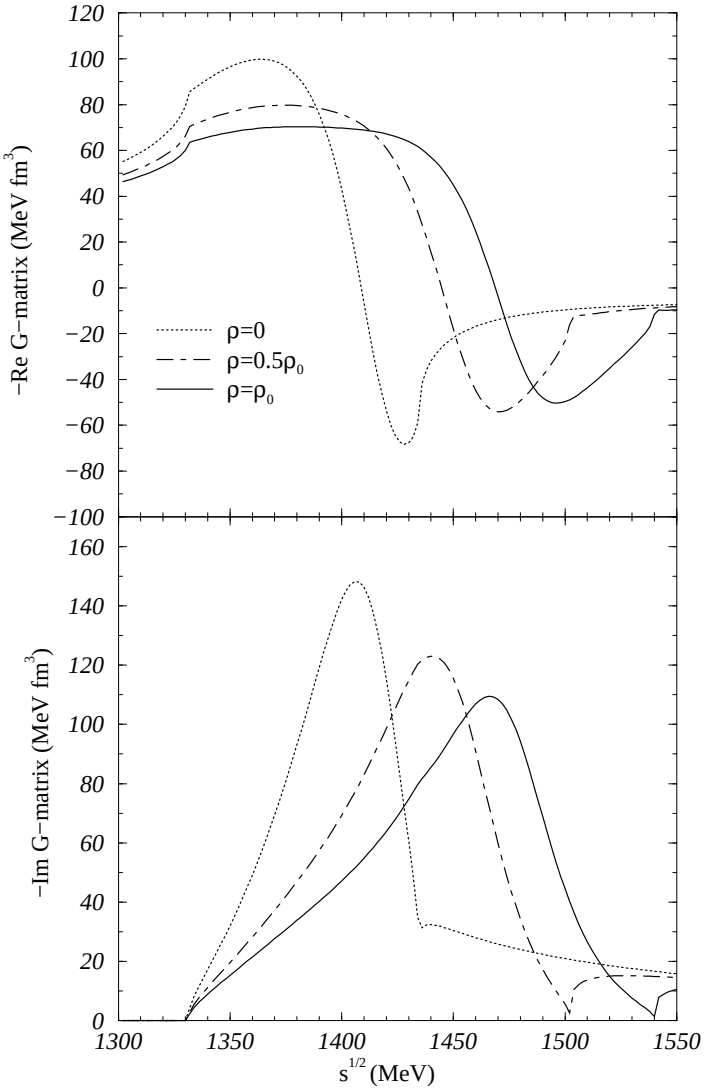

Figure 2.3: Real and imaginary parts of the $\bar{K}N$ amplitude in the $I = 0$, $L = 0$ channel as functions of the center-of-mass energy at total momentum $|\vec{k}_{\bar{K}} + \vec{k}_N| = 0$ for various densities.

is already complex at threshold due to the $\pi\Lambda$, $\pi\Sigma$ channels. In this simplified self-consistent scheme, only the real part of the $\bar{K}$ potential is retained in the solution of the G-matrix, i.e. the $\bar{K}$ energy appearing in the energy denominator of the G-matrix equation (2.9) is taken to be the real quasiparticle energy of Eq. (2.13).

Once self-consistency is achieved, we use Eq. (2.23) to calculate both real and

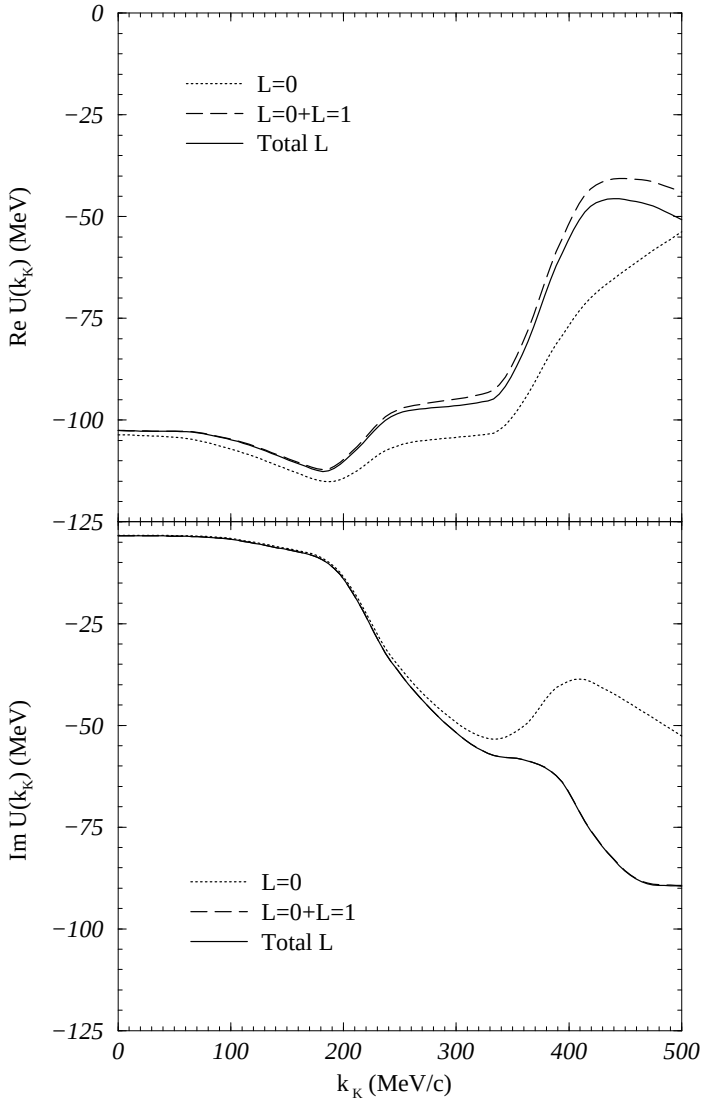

Figure 2.4: Real and imaginary parts of the $\bar{K}$ optical potential at $\rho = \rho_0$ as functions of the antikaon momentum. These results are obtained when only the real part of the $\bar{K}$ potential is determined self-consistently.

imaginary parts of the $\bar{K}$ potential, which are displayed in Fig. 2.4 as functions of the antikaon momentum, for normal nuclear matter density $\rho = \rho_0$. We explicitly show the separate contribution of the various partial waves of the $\bar{K}N$ interaction. At zero momentum the real part of the $\bar{K}$ potential is about -100 MeV and the partial waves

higher than the $L = 0$ component give a negligible contribution. Both the real and imaginary parts of the potential show some structure between 200 MeV/c and 400 MeV/c. This is connected to the behavior of the in-medium $\bar{K}N$ amplitude which, in this simplified self-consistent scheme, still retains the resonant-like shape at $\rho = \rho_0$. We observe that the high partial waves start being non-negligible for momenta larger than 200 MeV/c. It is interesting to focus our attention on the imaginary part of the $\bar{K}$ potential which at low momentum is rather small. This is due to the supressed coupling to intermediate $\pi\Sigma$ states as a result of the strong attraction felt by the antikaon combined with the attraction of around -70 MeV felt by the nucleon. The in-medium $\bar{K}N$ system then explores energies below those available for $\pi\Sigma$ excitations and the antikaon width becomes extremely small. In this low momentum region the imaginary part of the $\bar{K}$ potential is essentially due to the coupling to $\pi\Lambda$ states in the relatively weak $I = 1$ channel. As seen in the figure, for the $\pi\Sigma$ channel to start giving a contribution to the imaginary part, it is necessary to provide the $\bar{K}$ with a finite momentum (around 200 MeV/c), such that the condition $E^{qp}_{\bar{K}} + E^{qp}_{N} > m_\pi + m_\Sigma + U_\Sigma \simeq$ 1300 MeV can be fulfilled.

The substantial attraction obtained for the $\bar{K}$ optical potential combined with the extremely small imaginary component of the $\bar{K}$ optical potential might induce to think that the chances of producing very narrow, hence observable, deeply bound $\bar{K}$-nucleus states are quite high. If these results were confirmed by more sophisticated treatments of the in-medium effects, an experimental search for these states should be indeed encouraged. However, as we will show in the following, the use of a more realistic self-consistent scheme wears this finding off.

Our second method consists of determining the complete complex $\bar{K}$ single-particle

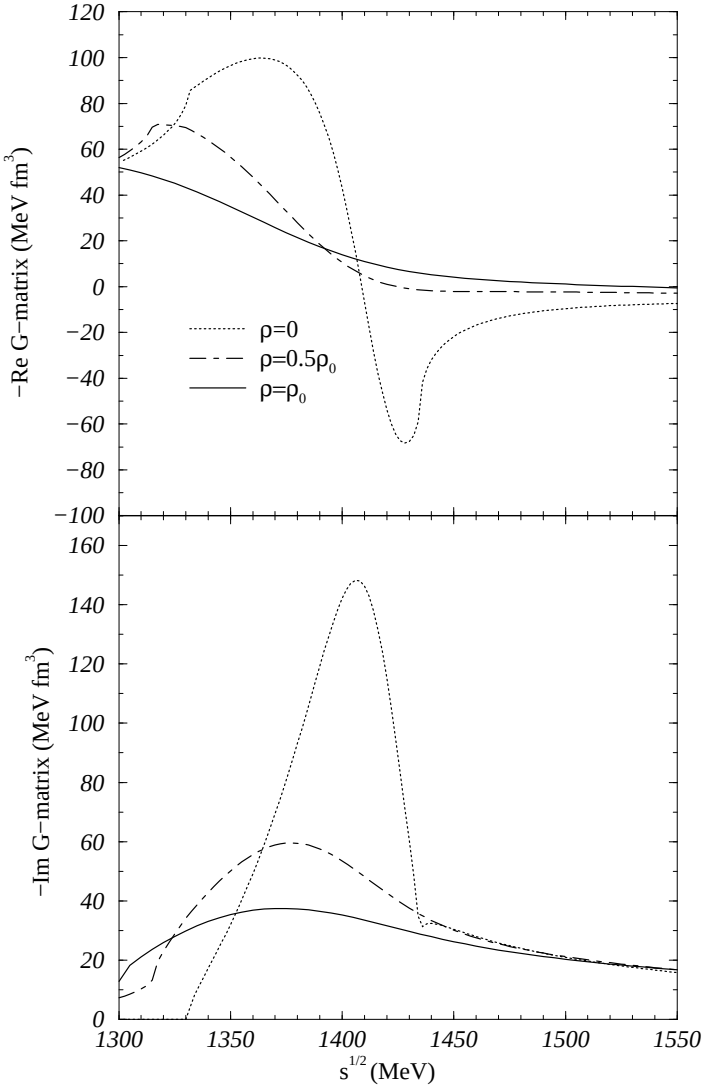

Figure 2.5: Real and imaginary parts of the $\bar{K}N$ amplitude in the $I = 0$, $L = 0$ channel as functions of the center-of-mass energy at total momentum $|\vec{k}_{\bar{K}} + \vec{k}_N| = 0$ for various densities, as obtained from a self-consistent calculation with a complex $\bar{K}$ optical potential.

energy given in Eq. (2.12) self-consistently. That means that the antikaons in the intermediate states of the G-matrix equation are dressed with the so-called "quasiparticle" spectral density given in Eq. (2.30), which has a width proportional to the imaginary part of the optical potential at the quasiparticle peak.

We first show in Fig. 2.5 the effect of dressing the antikaon with a complex self-energy on the in-medium $\bar{K}N$ amplitude for a center-of-mass momentum $|\vec{k}_N+\vec{k}_{\bar{K}}|=0$. We represent the on-shell amplitudes using the in-medium energy-momentum relation $\Omega = E_N^{qp}(k_N)+E_{\bar{K}}^{qp}(k_{\bar{K}})$. In fact, with respect to the results of Fig. 2.3, we have included here the mean field potential for the baryons, which produces an attractive shift in the amplitudes, plus the effect of the antikaon optical potential, which produces a further attraction and a widening in the energy distribution, the latter due to the $\bar{K}$ strength being spread out over energy. We note that, considering Pauli blocking that forces $k_N > k_F$ together with the in-medium attraction for antikaons and nucleons, the new $\bar{K}N$ threshold at ρ_0 drops down to about 1422 MeV. Comparing with the results shown in Fig. 2.3, we observe that the resonance peak appears at a lower energy, below the corresponding in-medium $\bar{K}N$ threshold. The resonance gets wider and dilutes much earlier with increasing density. These effects are in qualitative agreement with those obtained with the self-consistent approaches of Refs. [Ram00, Lut98a].

Our results for the antikaon potential at $\rho = \rho_0$ obtained with this complete self-consistent scheme are shown in Fig. 2.6. The real part of the $\bar{K}$ potential at zero momentum increases to -87 MeV. This attraction is similar to what is found by other self-consistent calculations [Ram00, Lut98a] for the optical potential at the quasiparticle energy, $E_{\bar{K}}^{qp}$. In Ref. [Lut98a] the peak in the $k_{\bar{K}} = 0$ spectral function for normal nuclear matter density appears at an energy -380 MeV, which is the quasiparticle energy at zero momentum, usually identified as the effective $\bar{K}$ mass, $m_{\bar{K}}^*$. The non-relativistic potential is then $(m_{\bar{K}}^{*2} - m_{\bar{K}}^2)/2m_{\bar{K}} \simeq -100$ MeV. Similarly, the results of Ref. [Ram00] for dressed antikaons but free pions, as done in this chapter up to now and in Ref. [Lut98a], provide an optical potential at the quasiparticle energy of -70 MeV. However, the potential relevant for the study of kaonic atoms must be taken at

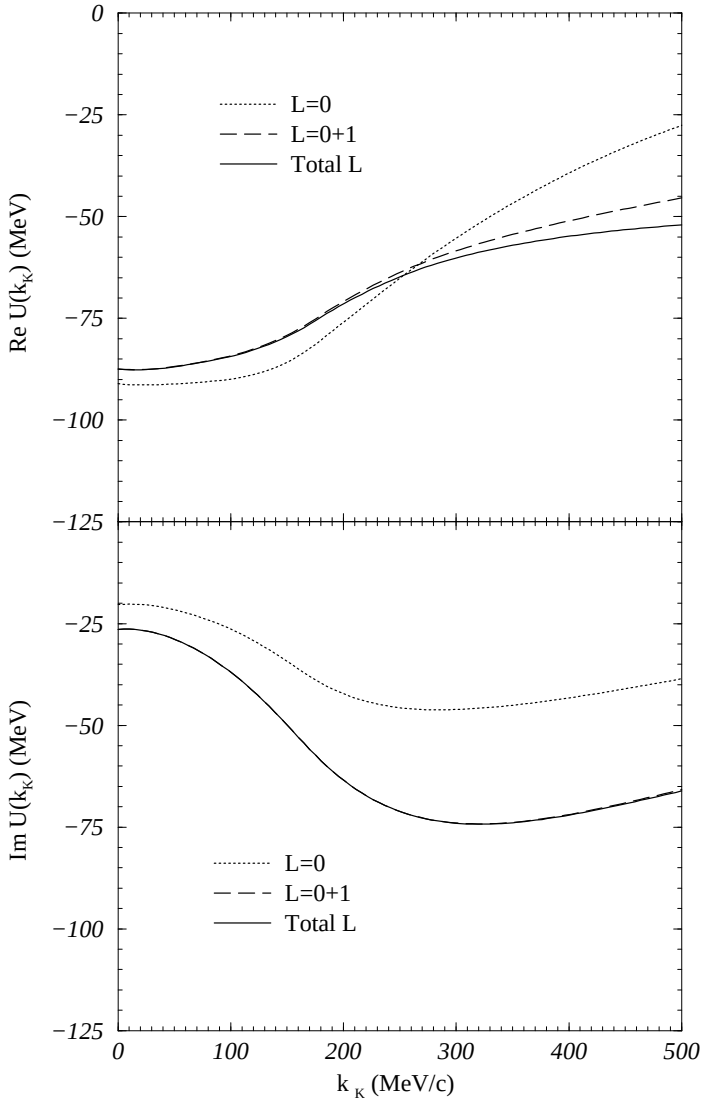

Figure 2.6: Same as Fig. 2.4 but obtained from a self-consistent scheme which uses the complex $\bar{K}$ optical potential.

the antikaon mass, $\omega = m_{\bar{K}}$, and, due to the strong energy dependence of the $\bar{K}N$ amplitude, the value can differ substantially from that taken at the quasiparticle energy. In the model of Ref. [Lut98a] it amounts to only -35 MeV, as can be inferred from the scattering length shown in [Lut98b]. The corresponding value for the model of Ref. [Ram00] is -45 MeV and in the present work we obtain a more moderate de-

crease in the attraction, from -87 MeV at the quasiparticle energy to -73 MeV at the antikaon mass. The different size of the reduction with respect to the value at the quasiparticle energy obtained with the various $\bar{K}N$ interaction models is a reflection of differences in the position and width of the in-medium $\Lambda(1405)$ resonance.

It is worth noticing that the new self-consistent scheme has produced a drastically different imaginary part, as can be seen by comparing the results of Fig. 2.6 with those of Fig. 2.4. The small value of -3 MeV at zero momentum obtained using the simplified scheme turns out to be now around -25 MeV, hence making the observation of bound $\bar{K}$ nuclear states more difficult. This is a consequence of the fact that the in-medium $\bar{K}N$ amplitude becomes smoother and wider when the $\bar{K}$ energies are complex. Since the $\bar{K}$ spectral density develops a width and, in turn, the $\bar{K}$ feels a reduced attraction, the $\bar{K}N$ states can couple more easily to the $\pi\Sigma$ states than in the simplified self-consistent scheme. From these results one must conclude that any approach claiming for narrow bound $\bar{K}$ nuclear states [Aka02] must be looked at with caution, because the self-consistent scheme affects enormously the predicted $\bar{K}$ properties in the medium.

The effect of including the higher partial waves of the $\bar{K}N$ interaction is also shown in Fig. 2.6. We observe that at zero $\bar{K}$ momentum there is already some contribution of partial waves higher than $L = 0$ due to the fact that the $\bar{K}$ meson interacts with nucleons that occupy states up to the Fermi momentum, giving rise to finite $\bar{K}N$ relative momenta of up to around 90 MeV/c. Clearly, the effect of the higher partial waves increases with increasing the $\bar{K}$ momentum, flattening out the real part of the optical potential and producing more structure to the imaginary part. At a $\bar{K}$ momentum around 500 MeV/c, the inclusion of higher partial waves makes the real part more attractive, from -28 MeV to -52 MeV, and practically doubles the size of the

imaginary part. Note that the effect of high partial waves is repulsive at low momenta and attractive at high momenta, while in the simplified self-consistent scheme reported in Fig. 2.4 it was always repulsive. This is due to the fact that the fully self-consistent scheme gives rise to a less attractive $\bar{K}$ potential, thus exploring larger energy values of the $\bar{K}N$ amplitudes. At a $\bar{K}$ momentum of around 250 MeV/c one already feels the change of sign of the isospin averaged $L = 1$ $\bar{K}N$ amplitude, which turns from being repulsive to being attractive at around 1500 MeV. In the simplified scheme one must compensate the additional attraction of the $\bar{K}$ with kinetic energy, hence the change of sign does not happen until a larger momentum, just above 500 MeV/c as can be appreciated from Fig. 2.4.

In Fig. 2.7 we represent the real and the imaginary part of $U_{\bar{K}}$ for different densities, obtained with the scheme that considers the complex potential for the antikaon. As we increase the density we obtain a more attractive potential due to two facts. On one hand, as discussed previously, the $\bar{K}N$ in-medium amplitude becomes more attractive at higher densities. On the other hand, the $\bar{K}$ potential is built up from summing this attractive two-body $\bar{K}N$ interaction over more $\bar{K}N$ pairs. The momentum dependence is moderate for the real part. In contrast, the imaginary part for densities around the saturation density and beyond shows more structure. This momentum dependence is smoother than that obtained in Ref. [Sib98] from a phenomenological model using the information of the vacuum $\bar{K}N$ amplitudes, where the antikaon optical potential at normal nuclear matter density ρ_0 increases from -140 MeV at zero momentum to around -50 MeV at high momenta.

Starting from the self-consistent $\bar{K}$ optical potential shown in Fig. 2.6 and reproduced by the solid line in Fig. 2.7, we perform two different tests in order to check some

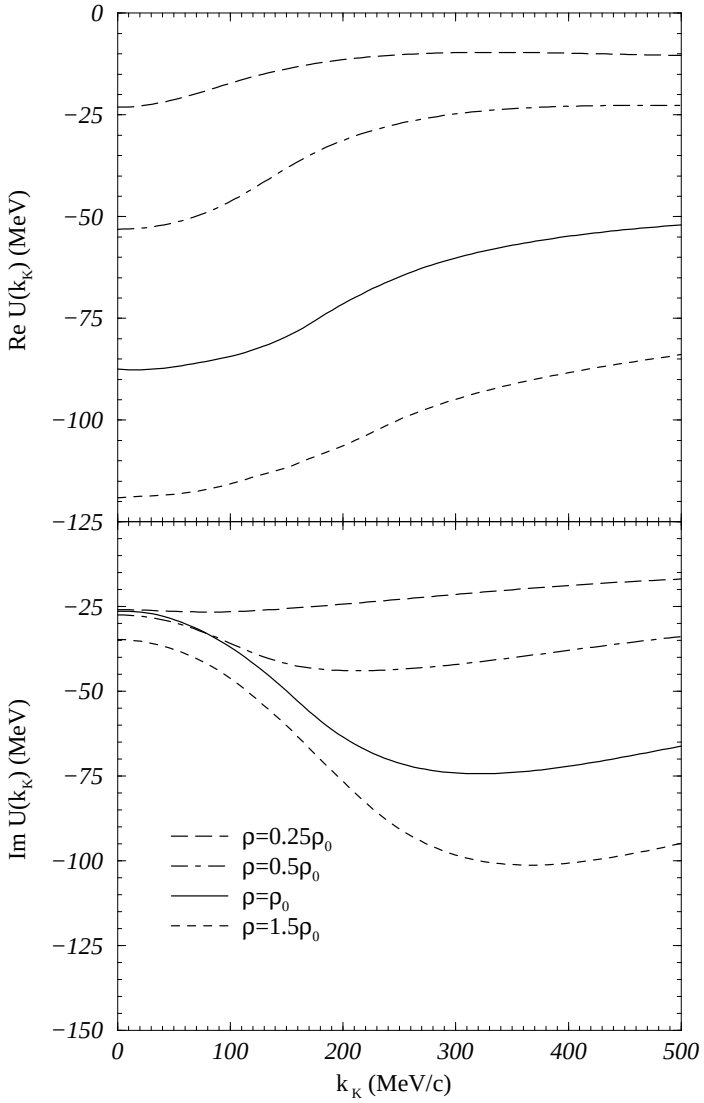

Figure 2.7: Real and imaginary parts of the $\bar{K}$ optical potential as functions of the antikaon momentum for various densities.

of the approximations used in the literature. First, we compute the optical potential neglecting the nucleon recoil corrections, as done in Ref. [Scha00]. This amounts to calculate the $\bar{K}$ potential at momentum $k_{\bar{K}}$ from a $G\rho$ type expression, with G being the in-medium $\bar{K}N$ interaction between a $\bar{K}$ of momentum $k_{\bar{K}}$ and a nucleon of zero

momentum. The expression for the $U_{\bar{K}}$ in this approach reads

$$U_{\bar{K}}(k_{\bar{K}}) = \frac{\pi^2}{2}\sum_{LJI}\frac{(2J+1)(2I+1)}{2}\langle k = \tfrac{m_N}{m_N+m_{\bar{K}}}k_{\bar{K}}|\ G\ |k = \tfrac{m_N}{m_N+m_{\bar{K}}}k_{\bar{K}}\rangle\ \rho\ , \qquad (2.31)$$

where m_N and $m_{\bar{K}}$ are the masses of the nucleon and antikaon, respectively.

The results are displayed by the dashed lines in Fig. 2.8. While the real part is barely affected by this simplified approximation, the imaginary part shows some non-negligible differences at low momenta. Secondly, we have neglected, in addition, the nucleon single-particle potential, which has been claimed to be unimportant in Ref. [Scha00]. Note that in this latter reference a small imaginary part of around 10 MeV for the nucleon optical potential is used, but the real part is set to zero. The results are shown by the dotted line. The differences with the dashed line are quite appreciable at low momenta, both for the real and imaginary parts of the $\bar{K}$ optical potential.

Finally, once self-consistency is reached, we calculate the full energy dependence of the $\bar{K}$ self-energy which defines the in-medium $\bar{K}$ single-particle propagator and its spectral density through Eqs. (2.27) and (2.28). The spectral density at zero momentum is shown in Fig. 2.9 for several densities. As density increases the peak of the $\bar{K}$ pole moves towards lower energies since the $\bar{K}$ optical potential becomes more attractive. The in-medium $\Lambda(1405)$ resonance gets wider and, although not signaled by any clear peak in the figure, its presence can be indirectly noticed from examining the $\bar{K}$ spectral density on the right hand side of the quasiparticle peak, which falls off more slowly than that on the left hand side.

We also notice some structure of the spectral function to the left of the quasipar-

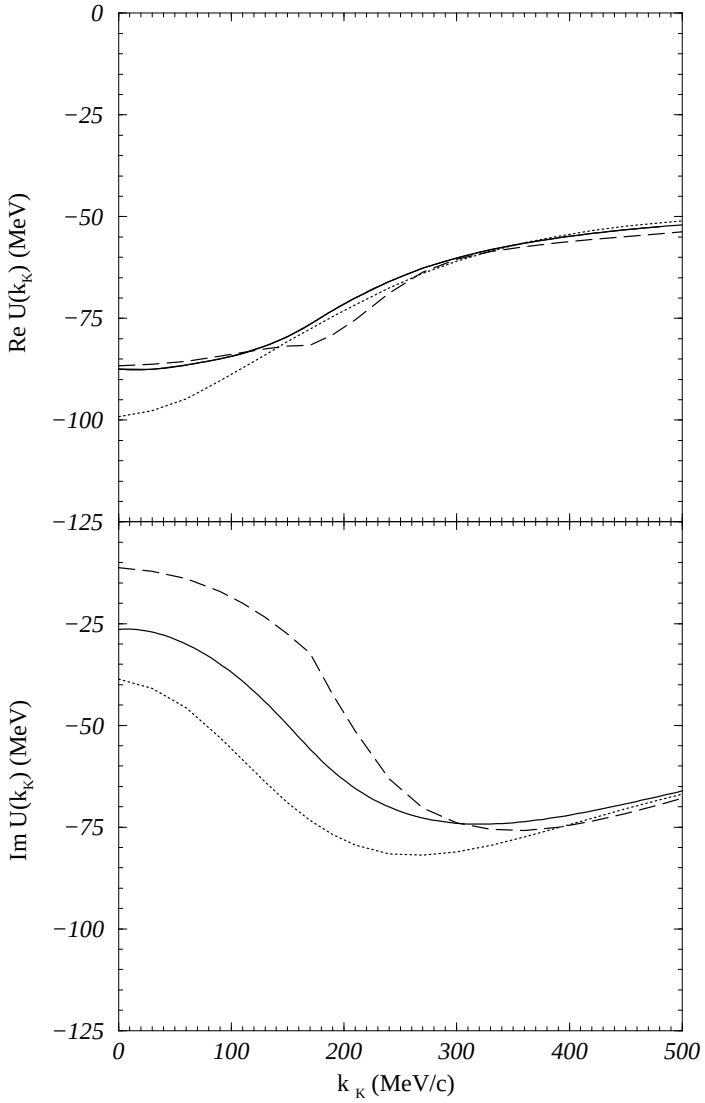

Figure 2.8: Real and imaginary parts of the $\bar{K}$ optical potential as functions of the antikaon momentum for various approximations. Solid line: our results. Dashed line: nucleon recoil corrections neglected. Dotted line: nucleon recoil corrections neglected and free–particle spectrum used for nucleons.

ticle peak at energies of the $\bar{K}$ of around $320 - 360$ MeV, the origin of which can be traced back to the Σ pole diagram of the $\bar{K}N$ Jülich interaction in the $L = 1$, $I = 1$ channel that appears as a singularity in the free $\bar{K}N$ scattering amplitude at an energy $\sqrt{s} = 1230$ MeV, about 200 MeV below the $\bar{K}N$ threshold. This peak in the $\bar{K}$

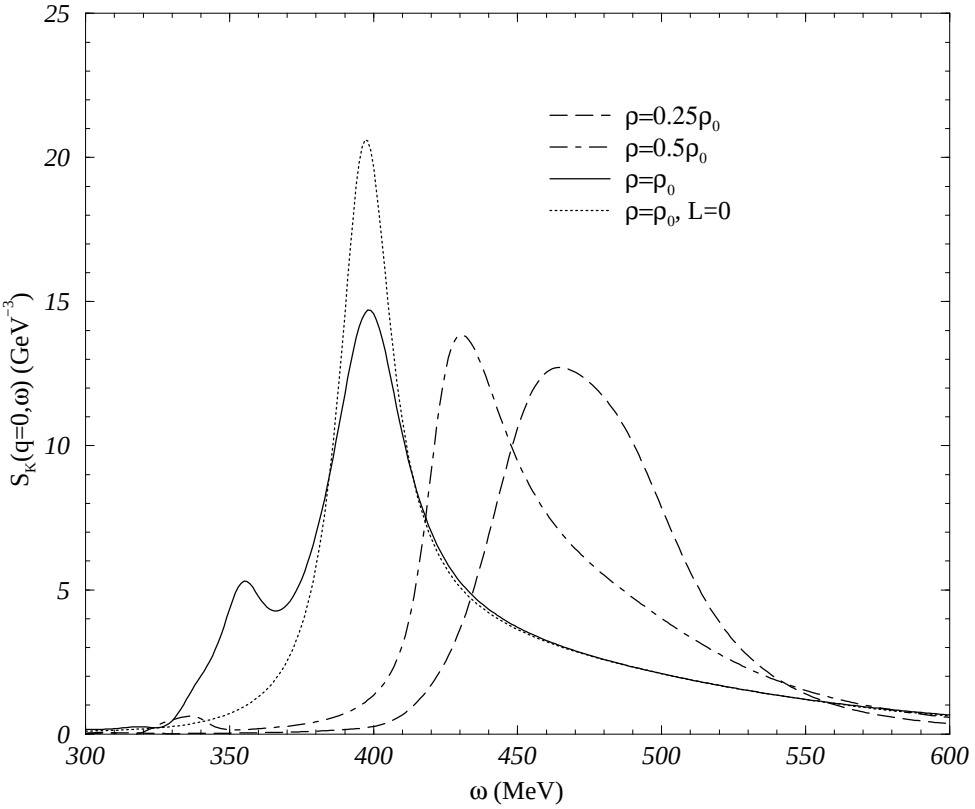

Figure 2.9: $\bar{K}$ spectral density at $k_{\bar{K}} = 0$ as a function of energy for various densities.

spectral function is therefore indicating the physical excitation of Σ-hole states in the nuclear medium with antikaon quantum numbers. If the P-wave Jülich interaction had contained the $\Sigma^*(1385)$ pole diagram, one would find similar structures due to Σ^*-hole excitations. The dotted line shows the spectral density at $\rho = \rho_0$ but keeping only the $L = 0$ component of the $\bar{K}N$ interaction. In agreement with the behavior of the optical potential at zero momentum, we observe that the location of the quasiparticle peak only moves a few MeV, while the width (height) gets reduced (increased) by about 30%.

2.4 Pions in nuclear matter

In this section we study the influence of the in-medium pion properties on the $\bar{K}$ self-energy. When a pion propagates in nuclear matter, it scatters with the surrounding nucleons and the basic first order response of the medium is the excitation of a particle-hole pair. In the region of intermediate energies ($T_\pi = 0 - 300$ MeV), delta-hole excitation also takes place due to the excitation of internal degrees of freedom of the nucleon. These are the first medium corrections in the perturbative expansion of the pion propagator in nuclear matter. In the following, we give a brief description of these medium corrections following the developments and notation of Refs. [Cab01, Ose82b, Fet71, Eri88].

In order to obtain the pion self-energy in symmetric nuclear matter and, therefore, the pion propagator to be inserted in the calculation of the $\bar{K}$ self-energy, we should compute the particle-hole and delta-hole excitations. For the particle-hole excitation, the Yukawa Hamiltonian is taken for the πNN interaction vertex

$$H_{\pi NN} = ig\overline{\Psi}_N(x)\gamma_5\vec{\tau}\vec{\phi}(x)\Psi_N(x) \ , \tag{2.32}$$

where g is the πNN strong coupling constant. Its non-relativistic reduction reads

$$H_{\pi NN} \sim \frac{f_N}{m_\pi}\sigma_i\partial_i\phi^\lambda(x)\tau^\lambda \ , \tag{2.33}$$

where $f_N/m_\pi = g/2m_N$, with m_N the nucleon mass. The quantities f_N and m_π are the nucleon coupling constant and the pion mass, respectively, while σ and τ are the spin Pauli matrices and the $\frac{1}{2}$ isospin operator, respectively. In momentum space, this

leads to the factor $\frac{f_N}{m_\pi}\vec{\sigma}\vec{q}\tau^\lambda$ for each πNN vertex with an incoming pion of momentum $\vec{q}$. For an outgoing pion, a minus sign arises. Therefore, using Feynman rules, the first order irreducible pion self-energy coming from particle-hole excitation $\Pi_0^{ph}(\vec{q},q^0)$ can be calculated:

$$-i\Pi_0^{ph}(\vec{q},q^0)^{\lambda\lambda'} = (-1)\int \frac{d^4k}{(2\pi)^4}\left(\frac{f_N}{m_\pi}\right)^2 \vec{\sigma}(-\vec{q})\vec{\sigma}\vec{q}\tau^\lambda\tau^{\lambda'} iG^0(\vec{k},k^0)iG^0(\vec{k}+\vec{q},k^0+q^0) \quad (2.34)$$

where $G^0(\vec{k},k^0)$ is the nucleon propagator. A sum over intermediate spin and isospin states must be understood in the following. The sum over protons and neutrons gives a factor $2\delta^{\lambda\lambda'}$, while for the spin sum we use the property

$$\sum_{m_s,m_s'} \langle m_s|\sigma_i q_i|m_s'\rangle\langle m_s'|\sigma_j q_j|m_s\rangle = 2\delta_{ij}q_iq_j = 2\vec{q}^{\,2}\ . \quad (2.35)$$

Using the expression of the nucleon propagator, we can write

$$\begin{aligned}\Pi_0^{ph}(\vec{q},q^0)^{\lambda\lambda'} \quad &\equiv \delta^{\lambda\lambda'}\Pi_0^{ph}(\vec{q},q_0) = -i\delta^{\lambda\lambda'}4\left(\frac{f_N}{m_\pi}\right)^2\vec{q}^{\,2} \\ &\times\int\frac{d^4k}{(2\pi)^4}\left\{\frac{1-n(\vec{k})}{k^0-E_N(\vec{k})+i\eta}+\frac{n(\vec{k})}{k^0-E_N(\vec{k})-i\eta}\right\} \\ &\times\left\{\frac{1-n(\vec{k}+\vec{q})}{k^0+q^0-E_N(\vec{k}+\vec{q})+i\eta}+\frac{n(\vec{k}+\vec{q})}{k^0+q^0-E_N(\vec{k}+\vec{q})-i\eta}\right\} \quad (2.36)\end{aligned}$$

where $n(\vec{k})$ is the Fermi distribution for nucleons. The integration over k^0 can be done analytically and only the crossed products of terms from the first and second brackets of Eq. (2.36) contribute.

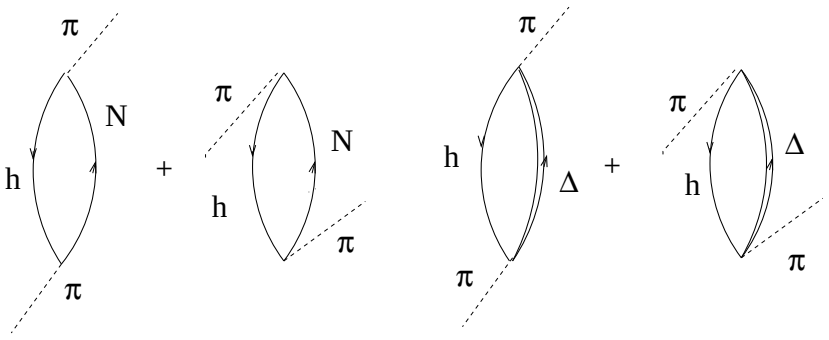

Figure 2.10: Direct and crossed particle-hole (left figures) and delta-hole (right figures) diagrams.

Therefore, one is left with

$$\Pi_0^{ph}(\vec{q}, q^0) = \left(\frac{f_N}{m_\pi}\right)^2 \vec{q}^{\,2} \mathcal{U}_N(\vec{q}, q^0) \ , \tag{2.37}$$

where $\mathcal{U}_N(\vec{q}, q^0)$ is the Lindhard function for the particle-hole excitation, which reads

$$\mathcal{U}_N(\vec{q}, q^0) = \tag{2.38}$$
$$\nu_N \int \frac{d^3k}{(2\pi)^3} \left[\frac{\theta(k_F - |\vec{k}|)[1 - \theta(k_F - |\vec{k} + \vec{q}|)]}{q^0 + E_N(\vec{k}) - E_N(\vec{k} + \vec{q}) + i\eta} + \frac{\theta(k_F - |\vec{k} + \vec{q}|)[1 - \theta(k_F - |\vec{k}|)]}{-q^0 - E_N(\vec{k}) + E_N(\vec{k} + \vec{q}) + i\eta} \right] ,$$

where we have used that the nucleon Fermi distribution $n(\vec{k})$ at $T = 0$ is equal to the $\theta(k_F - |\vec{k}|)$ and $\nu_N = 4$. An analytical expression for Eq. (2.38) can be found in Refs. [Fet71, Ose90]. This result for $\Pi_0^{ph}(\vec{q}, q^0)$ can be quoted as the contribution of the two diagrams on the left-hand side of Fig. 2.10, which are called direct and crossed terms, or forward and backward propagating bubbles, respectively. The arrows indicate the particle and hole character of the nucleonic line, with the convention that up heading arrows stand for particles and down heading arrow for holes. Opening the hole line on the left-hand side diagrams of Fig. 2.10, we find two diagrams that contribute to πN scattering and, therefore, the pion self-energy can be understood as

an integral of the πN scattering matrix over the occupied states of the Fermi sea.

In the region of intermediate energies ($T_\pi = 0-300$ MeV), delta-hole excitations can occur ($\Delta(1232)P_{33}, I(J^P) = \frac{3}{2}\left(\frac{3}{2}^+\right), M_\Delta = 1232\,\mathrm{MeV}$) and they must be included as an additional medium correction to the particle-hole one. The $\pi N\Delta$ vertex is obtained from the effective phenomenological Hamiltonian (in a non-relativistic approach)

$$H_{\pi N\Delta} = \frac{f^*_\Delta}{m_\pi} S_i \partial_i \phi^\lambda(x) T^\lambda + h.c. \ , \tag{2.39}$$

where S_i, T^λ are the $\frac{1}{2} \to \frac{3}{2}$ spin, isospin transition operators defined by means of the Wigner-Eckart theorem as

$$\langle \tfrac{3}{2} M_s | S^+_\nu | \tfrac{1}{2} m_s \rangle = C\left(\tfrac{1}{2}, 1, \tfrac{3}{2}; m_s, \nu, M_s\right) \langle \tfrac{3}{2} || S^+ || \tfrac{1}{2} \rangle \ . \tag{2.40}$$

In order to compute the sum over spin and isospin we make use of the relation

$$\sum_{M_s} S_i |M_s\rangle\langle M_s| S^+_j = \frac{2}{3}\delta_{ij} - \frac{1}{3} i \ \epsilon_{ijk} \ \sigma_k \ . \tag{2.41}$$

The coupling constant f^*_Δ, obtained from fits to scattering data, is $\frac{f^*_\Delta}{f_N} = 2.13$.

In a similar way to the particle-hole case, the contribution of the delta-hole excitation to the pion self-energy is given by two diagrams [see the two diagrams on the r.h.s of Fig. 2.10] corresponding to the two terms in Eq. (2.39), and the $\Pi_0^{\Delta h}(\vec{q}, q^0)$ reads

$$\Pi_0^{\Delta h}(\vec{q}, q^0) = \left(\frac{f_N}{m_\pi}\right)^2 \vec{q}^{\,2} \mathcal{U}_\Delta(\vec{q}, q^0) \ , \tag{2.42}$$

where $\mathcal{U}_\Delta(\vec{q},q^0)$ is the Δ-hole Lindhard function

$$\mathcal{U}_\Delta(\vec{q},q^0) = \tag{2.43}$$
$$\nu_\Delta \int \frac{d^3k}{(2\pi)^3}\left[\frac{\theta(k_F-|\vec{k}|)}{q^0+E_N(\vec{k})-E_\Delta(\vec{k}+\vec{q})+i\frac{\Gamma(\vec{q},q^0)}{2}}+\frac{\theta(k_F-|\vec{k}+\vec{q}|)}{-q^0+E_N(\vec{k}+\vec{q})-E_\Delta(\vec{k})+i\frac{\Gamma(\vec{q},-q^0)}{2}}\right],$$

with $\nu_\Delta = \frac{16}{9}\left(\frac{f^*_\Delta}{f_N}\right)^2$. In Eq. (2.43) the non-relativistic reduction of the Δ propagator has been used and Γ is the energy dependent decay width of the Δ into πN which, using the approximations done in Ref. [Ose90], is taken to depend only on the external variables of the pion. The analytical result is given in this same reference.

The expression for the first-order irreducible pion self-energy finally reads

$$\Pi_0(\vec{q},q^0) = \left(\frac{f_N}{m_\pi}\right)^2 \vec{q}^{\,2}\mathcal{U}(\vec{q},q^0) \tag{2.44}$$
$$\mathcal{U}(\vec{q},q^0) = \mathcal{U}_N(\vec{q},q^0)+\mathcal{U}_\Delta(\vec{q},q^0)\ ,$$

where $\mathcal{U}(\vec{q},q^0)$ is the sum of $1p-1h$ and $1\Delta-1h$ Lindhard functions. We also include in the pion self-energy the coupling to $2p-2h$ excitations, following the phase-space approach of Ref. [Ram94].

Once $1p-1h$ $(2p-2h)$ and $1\Delta-1h$ excitations are computed, form-factors and short-range correlations are introduced. One pion exchange (OPE) provides a good description of the nucleon-nucleon interaction for long distances, but this is not the only ingredient. At shorter distances other effects must be considered, such as correlated and uncorrelated two pion exchange and the exchange of heavier mesons. Therefore, short range spin-isospin correlations have to be taken into account.

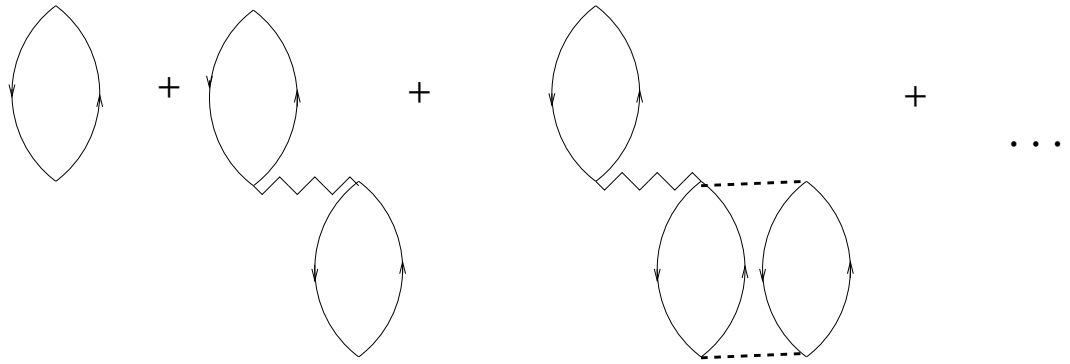

Figure 2.11: Sum of diagrams which contribute to the pion self-energy, taken from Ref. [Cab01]. The wiggly line stands for the Landau-Migdal parameter g'.

Its contribution is mimicked with an effective OPE interaction

$$\widetilde{V}_{OPE}(q) = V_{OPE} + \left(\frac{f_N}{m_\pi}\right)^2 g' \vec{\sigma}_1 \vec{\sigma}_2 \vec{\tau}_1 \vec{\tau}_2 \ , \tag{2.45}$$

called minimal correlation. The g' is the Landau-Migdal parameter taken from the particle-hole interaction described in Ref. [Ose82a], which includes π and ρ exchange modulated by the effect of nuclear short-range correlations.

As a consequence, the pion self-energy must be recalculated including these short-range correlations, summing the diagrams of Fig. 2.11 which contribute to the irreducible pion self-energy. The same procedure is applied for the Δ-nucleon interaction.

The final expression for the pion self-energy reads

$$\begin{aligned} \Pi(\vec{q}, q^0) &= F(\vec{q}, q^0) \left(\frac{f_N}{m_\pi}\right)^2 \vec{q}^{\,2} \frac{\mathcal{U}(\vec{q}, q^0)}{1 - (\frac{f_N}{m_\pi})^2 g' \mathcal{U}(\vec{q}, q^0)} \\ \mathcal{U}(\vec{q}, q^0) &= \mathcal{U}_N(\vec{q}, q^0) + \mathcal{U}_\Delta(\vec{q}, q^0) \ , \end{aligned} \tag{2.46}$$

where $F(\vec{q}, q^0)$ is the form factor,

$$\begin{aligned} F(\vec{q}, q^0) &= \left(\frac{\Lambda^2 - m_\pi^2}{\Lambda^2 - (q^{02} - \vec{q}^2)} \right)^2 \\ \Lambda &= 1200 \text{ MeV} . \end{aligned} \tag{2.47}$$

The pion self-energy also includes a s-wave piece

$$\Pi(\rho)_{\rm s} = -4\pi \ (1 + \frac{m_\pi}{m_N}) \ b_0 \ \rho, \tag{2.48}$$

with $b_0 = \frac{-0.0285}{m_\pi}$, taken from the parameterization of Ref. [Sek83] , which is equivalent to the results of Ref. [Mei89].

Therefore, the total pion self-energy reads

$$\Pi_\pi(\vec{q}, q^0) = \Pi(\rho)_s + \Pi(\vec{q}, q^0) \ . \tag{2.49}$$

The pion propagator can be obtained using the Dyson-Schwinger summation from the pion self-energy, as it was done for the $\bar{K}$ propagator. Redefining $\vec{k} \equiv \vec{q}$ and $\omega \equiv q^0$, the pion propagator reads

$$D_\pi(k_\pi, \omega) = \frac{1}{\omega^2 - k_\pi^2 - m_\pi^2 - \Pi_\pi(k_\pi, \omega)} \ . \tag{2.50}$$

As in the case of the $\bar{K}$ meson, we can define a pion optical potential, $U_\pi(k_\pi, \omega)$, from the complete π self-energy. We use

$$U_\pi(k_\pi, \omega) = \sqrt{k_\pi^2 + m_\pi^2 + \Pi_\pi(k_\pi, \omega)} - \sqrt{k_\pi^2 + m_\pi^2} \ , \tag{2.51}$$

which ensures that, when inserted in the G-matrix equation, one is using a quasiparticle approximation to the spectral function, with the peak located at the right quasiparticle energy defined by

$$(E_\pi^{qp}(k))^2 = k^2 + m_\pi^2 + \mathrm{Re}\,\Pi_\pi(k, E_\pi^{qp}) \ . \tag{2.52}$$

Due to the small mass of the pion, it has not been possible to use the same relation as for the $\bar{K}$ meson, namely, $\Pi_{\bar{K}}(k_{\bar{K}}, \omega) = 2\sqrt{k_{\bar{K}}^2 + m_{\bar{K}}^2}U_{\bar{K}}(k_{\bar{K}}, \omega)$, obtained by only retaining the first term in the expansion of the first square root of Eq. (2.51).

The pion single-particle energy to be used in the solution of the G-matrix of Eq. (2.9) is

$$E_\pi(k) = \sqrt{k^2 + m_\pi^2} + U_\pi(k, E_\pi^{qp}) \ . \tag{2.53}$$

The consequences of dressing the pions in the calculation of the $\bar{K}$ self-energy were already reported in Ref. [Ram00, Ram01a], where it was shown that the results for the $\bar{K}$ self-energy change substantially when pions are dressed with respect to the case when only free pions are included in the intermediate states of the $\bar{K}N$ Bethe-Goldstone equation.

Figs. 2.12 and 2.13 show clearly the importance of including the in-medium properties of pions in the calculation of the $\bar{K}$ self-energy. Fig. 2.12 displays the real and imaginary parts of the $\bar{K}$ optical potential as functions of the $\bar{K}$ momentum for two approaches: including the medium effects on the pion properties (solid lines) or disregarding them (long-dashed lines). When pions are dressed, the real part of the antikaon potential becomes less attractive increasing up to -60 MeV at $k_{\bar{K}} = 0$ MeV/c, and the imaginary part loses structure significantly. Fig. 2.13 shows the real and imaginary parts of the s-wave $\bar{K}N$ G-matrix as functions of the invariant center-of-mass energy

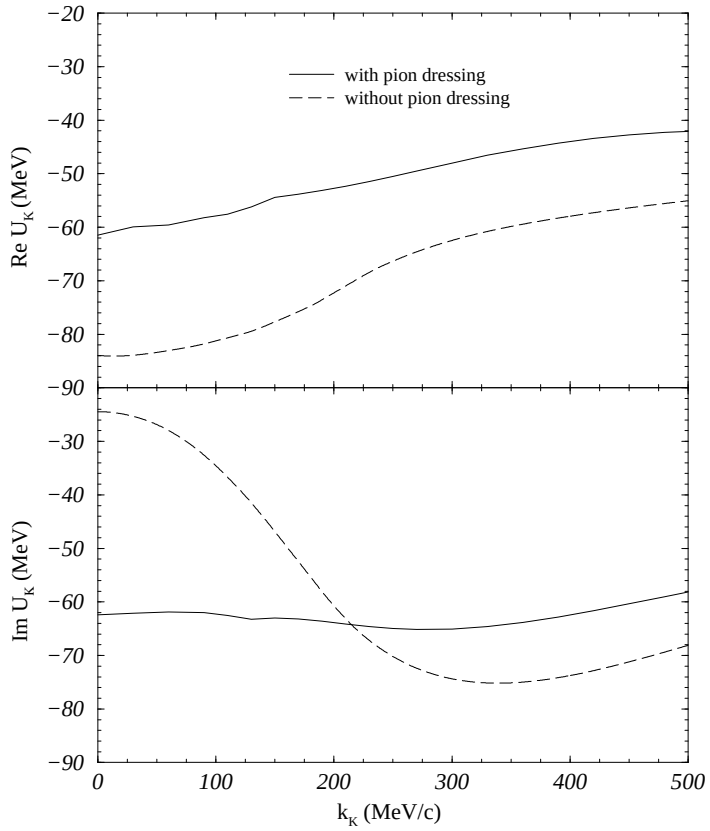

Figure 2.12: Real and imaginary parts of $U_{\bar{K}}$ at $\rho = 0.17$ fm^{-3} as functions of the antikaon momentum with or without including the dressing of pions.

for $I = 0$ and $I = 1$. It is shown that the previous behaviour for the $\bar{K}$ self-energy when pions are dressed is a direct consequence of the energy dependence of the $\bar{K}N$ effective interaction for $I = 0$, which is the main contribution to the $L = 0$ component because of the $\Lambda(1405)$ resonant structure. Note that, due to the less attractive antikaon potential, one explores this interaction at higher energies, further away from the resonant structure.

It is especially interesting to observe the structure in the $I = 0$ amplitude appearing below the $\pi\Sigma$ threshold, a region in energy not explored in previous works [Lut98a, Ram00, Tol01a]. It appears that the resonance in the medium, previously identified

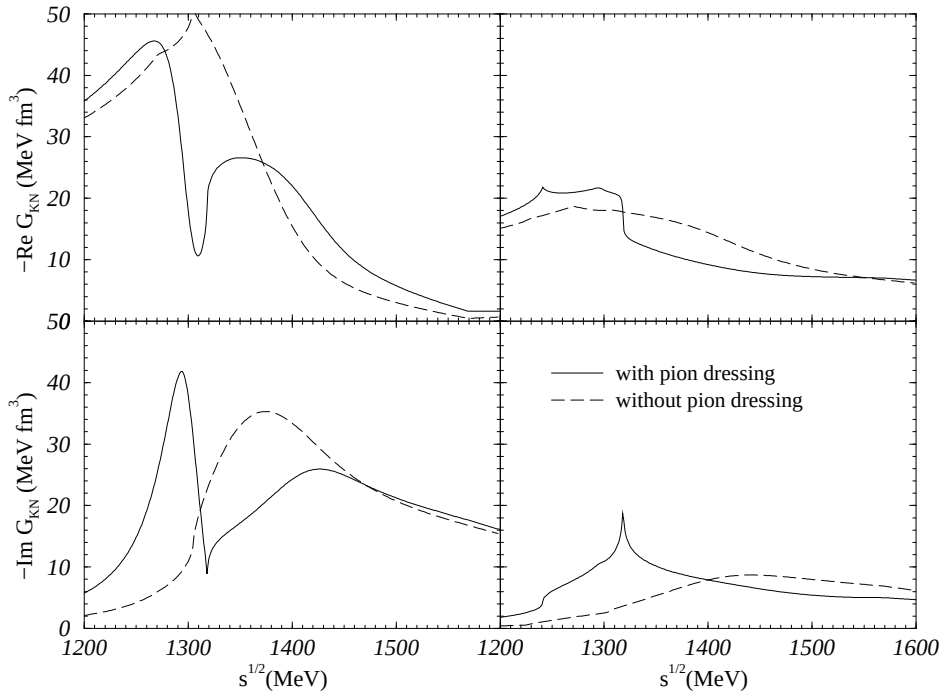

Figure 2.13: Real and imaginary parts of the $\bar{K}N$ amplitude in the $I = 0$, $L = 0$ channel (left panels) and the $I = 1$, $L = 0$ channel (right panels) at $\rho = 0.17$ fm^{-3} as functions of the center-of-mass energy at total momentum $|\vec{k}_{\bar{K}} + \vec{k}_N| = 0$ with or without including the dressing of pions.

with the bump in the imaginary part around 1400 MeV, might be more appropriately identified with the more pronounced peak appearing around 1300 MeV. Whether this is a new resonance (an additional pole in the complex plane) or just a reflection of the same one but distorted by the presence of a cusp at the $\pi\Sigma$ threshold is something that deserves further study. It is also surprising to note that when pions are not dressed this double structure disappears. At the moment, we can only say that there is an enhanced probability of finding a state with Λ-like quantum numbers around 1300 MeV. We note that this structure would have been signaled by a pole in the real axis if neither the pions nor the antikaons would have been dressed, since in this case there would not have been allowed states to decay to. In the self-consistent many-body approach used

here, the states to which this peaked structure can decay are of the type $\pi(ph)\Sigma$ or $\bar{K}(\Lambda h\pi)N$, where in parentheses we have denoted an example for the component of the π and $\bar{K}$ mesons that could show up at energies below the $\pi\Sigma$ threshold.

We note that in preparation to the finite temperature and higher density regimes explored in the following chapters, the results presented in this section contain some modifications on the properties of the baryons with respect to those used in Sec. 2.2. First, we have introduced slight modifications in the single-particle potential of the Λ and Σ hyperons, following the parameterization of Ref. [Bal97],

$$U_{\Lambda,\Sigma}(\rho) = -340\rho + 1087.5\rho^2 \ , \tag{2.54}$$

which is more appropriate for higher densities than the simple parameterization, linear in ρ, used previously.

On the other hand, for nucleons, we have used a relativistic $\sigma - \omega$ model, where the scalar and vector coupling constants, g_s and g_v respectively, are density dependent [Mac89]. This is a simple way to mimic results from Dirac-Brueckner-Hartree-Fock calculations and can be easily extended to the finite temperature case in the next chapter. Further details about the $\sigma - \omega$ model for nucleons will be given in the following chapter.

Chapter 3

The $\bar{K}N$ interaction in hot and dense matter

The aim of this chapter is to study the properties of the $\bar{K}$ meson in hot and dense matter. The calculation of the single-particle potential of the antikaon in symmetric nuclear matter at $T = 0$ is extended to the finite temperature case. The inclusion of temperature affects the Pauli blocking of the nucleons in the intermediate states, as well as the dressing of mesons and baryons. In particular, we pay attention to the temperature modifications on the pion self-energy. The present chapter is organized as follows: Sec. 3.1 is devoted to the treatment of the temperature effects while our results are presented and discussed in Sec. 3.2.

3.1 Finite temperature effects on the $\bar{K}N$ interaction

In the previous chapter, the $\bar{K}N$ interaction in the nuclear medium (G-matrix) at $T = 0$ was derived from a meson-baryon bare interaction built in the meson exchange framework [Mul90]. As it was shown there, one is facing a coupled-channel problem as the bare interaction permits transitions from the $\bar{K}N$ channel to the $\pi\Sigma$ and $\pi\Lambda$ ones, all having strangeness $S = -1$. In a schematic notation, each G-matrix fulfills the coupled channel equation

$$\begin{aligned}\langle M_1B_1 \mid G(\Omega) \mid M_2B_2\rangle &= \langle M_1B_1 \mid V(\sqrt{s}) \mid M_2B_2\rangle \\ &+ \sum_{M_3B_3} \langle M_1B_1 \mid V(\sqrt{s}) \mid M_3B_3\rangle \frac{Q_{M_3B_3}}{\Omega - E_{M_3} - E_{B_3} + i\eta} \langle M_3B_3 \mid G(\Omega) \mid M_2B_2\rangle \ , \quad (3.1)\end{aligned}$$

where Ω is the so-called starting energy, given in the lab frame, and $\sqrt{s}$ is the invariant center-of-mass energy. In Eq. (3.1), M_i and B_i represent, respectively, the possible mesons ($\bar{K}$, π) and baryons (N, Λ, Σ), and their corresponding quantum numbers, such as coupled spin and isospin, and linear momentum. The function $Q_{M_3B_3}$ stands for the Pauli operator preventing the nucleons in the intermediate states from occupying already filled ones. The coupled-channel equation is solved by means of a partial wave decomposition and working in isospin basis.

As it was done previously, the prescription for the single-particle energies of all the mesons and baryons participating in the reaction and in the intermediate states is written as

$$E_{M_i(B_i)}(k) = \sqrt{k^2 + m^2_{M_i(B_i)}} + U_{M_i(B_i)}(k, E^{qp}_{M_i(B_i)}) \ , \quad (3.2)$$

where $U_{M_i(B_i)}$ is the single-particle potential of each meson (baryon) calculated at the real quasi-particle energy $E^{qp}_{M_i(B_i)}$. For baryons, this quasi-particle energy is given by

$$E^{qp}_{B_i}(k) = \sqrt{k^2 + m^2_{B_i}} + U_{B_i}(k) \ , \tag{3.3}$$

while, for mesons, it is obtained by solving the following equation

$$(E^{qp}_{M_i}(k))^2 = k^2 + m^2_{M_i} + \mathrm{Re}\,\Pi_{M_i}(k, E^{qp}_{M_i}) \ , \tag{3.4}$$

where Π_{M_i} is the meson self-energy. The relation between Π_{M_i} and U_{M_i} is given in Eq. (2.26) for the antikaon and in Eq. (2.51) for the lighter pion.

The introduction of temperature in the calculation of the G-matrix affects the Pauli blocking of the intermediate nucleon states as well as the dressing of mesons and baryons present in the intermediate states. The G-matrix equation at finite T reads formally as in Eq. (3.1), but replacing

$$\begin{aligned} Q_{MB} &\rightarrow Q_{MB}(T) \\ G(\Omega) &\rightarrow G(\Omega, T) \\ E_M \ , E_B &\rightarrow E_M(T) \ , E_B(T) \ , \end{aligned}$$

where the density and other dependences of these quantities have been omitted for simplicity.

3.1.1 The Pauli blocking at finite temperature

The function $Q_{MB}(T)$ or Pauli blocking is unity for meson-hyperon states while, for $\bar{K}N$ states, follows the law $1 - n(k_N, T)$, where $n(k_N, T)$ is the nucleon Fermi distribution at the corresponding temperature

$$n(k_N, T) = \frac{1}{1 + \mathrm{e}^{\left(\frac{E_N(k_N,T)-\mu}{T}\right)}} \ . \tag{3.5}$$

The nucleonic spectrum at finite T, $E_N(k_N, T)$, is obtained following a $\sigma - \omega$ model that will be described in Sec. 3.1.2 and μ is the chemical potential obtained by imposing the normalization property

$$\rho = \frac{\nu}{(2\pi)^3} \int d^3k_N \ n(k_N, T) \ , \tag{3.6}$$

at each density ρ, where $\nu = 4$ is the spin-isospin degeneracy factor of symmetric nuclear matter.

As in the $T = 0$ case, we perform an angle average of the Pauli operator $Q_{\bar{K}N}(T)$, a strategy which facilitates the solution of the G-matrix equation in a partial wave basis. We first define $\vec{P}$ and $\vec{k}$ as the total and relative momenta of the $\bar{K}N$ pair, respectively, allowing us to rewrite the nucleon and antikaon momenta in the laboratory system, $\vec{k}_N$ and $\vec{k}_{\bar{K}}$ [see Eqs. (A.1) and (A.2)]. In terms of the total and relative momenta, the Pauli operator $Q_{\bar{K}N}(k_N, T)$ reads $Q_{\bar{K}N}(\mid \frac{\xi}{1+\xi}\vec{P} - \vec{k} \mid, T)$, which explicitly shows the dependence on the angle between $\vec{P}$ and $\vec{k}$. This dependence is eliminated in the G-matrix equation by replacing $Q_{\bar{K}N}$ by its angle average

$$\overline{Q}_{\bar{K}N}(k, P, T) = \frac{1}{2} \int_0^\pi d\theta \ \sin\theta \ Q_{\bar{K}N}(\vec{k}, \vec{P}, T) = \frac{1}{2\mathcal{B}} \ \ln \frac{\mathrm{e}^{\mathcal{A}} + \mathrm{e}^{\mathcal{B}}}{\mathrm{e}^{\mathcal{A}} + \mathrm{e}^{-\mathcal{B}}} \ , \tag{3.7}$$

with

$$\begin{aligned} \mathcal{A} &= \frac{\mu}{T} - \frac{k^2 + (\frac{\xi}{\xi+1})^2 P^2}{2 m_N T} \\ \mathcal{B} &= \frac{k\ \xi\ P}{T\ (1+\xi)\ m_N}\ , \end{aligned} \tag{3.8}$$

being m_N the mass of the nucleon and $\xi = m_N/m_{\bar{K}}$.

3.1.2 Mesons and baryons at finite temperature

- **Antikaon**

  Temperature also affects the properties of the particles involved in the process. The $\bar{K}$ optical potential at a given temperature is calculated according to

$$U_{\bar{K}}(k_{\bar{K}}, E^{qp}_{\bar{K}}, T) = \int d^3k_N\ n(k_N, T)\ \langle \bar{K}N \mid G_{\bar{K}N\to\bar{K}N}(\Omega = E^{qp}_N + E^{qp}_{\bar{K}}, T) \mid \bar{K}N\rangle \tag{3.9}$$

  This expression is equivalent to Eq. (2.16) but introducing the Fermi distribution for a given temperature. Once more, a self-consistent procedure for $U_{\bar{K}}$ is required. More explicitly, using the partial wave components of the G-matrix and similarly to the $T = 0$ case [see Eq. (2.23)], we obtain

$$\begin{aligned} U_{\bar{K}}(k_{\bar{K}}, E^{qp}_{\bar{K}}, T) &= \frac{1}{2}\sum_{L,J,I}(2J+1)(2I+1)\int n(k_N, T)\ k_N^2\ dk_N \\ &\times \langle (\bar{K}N); \overline{k} | G^{LJI}(\overline{P}, E^{qp}_{\bar{K}}(k_{\bar{K}}) + E^{qp}_N(k_N), T) | (\bar{K}N); \overline{k}\rangle\ , \end{aligned} \tag{3.10}$$

  where $\overline{k}$ and $\overline{P}$ are the relative and center-of-mass momentum, respectively, averaged over the angle between the external $\bar{K}$ momentum in the lab system, $\vec{k}_{\bar{K}}$,

and the internal momentum of the nucleon, $\vec{k}_N$.

The $\bar{K}$ self-energy is obtained from the optical potential through the relation

$$\Pi_{\bar{K}}(k_{\bar{K}},\omega,T) = 2\,\sqrt{k_{\bar{K}}^2 + m_{\bar{K}}^2}\; U_{\bar{K}}(k_{\bar{K}},\omega,T)\;, \tag{3.11}$$

and, straightforwardly, the $\bar{K}$ propagator reads

$$D_{\bar{K}}(k_{\bar{K}},\omega,T) = \frac{1}{\omega^2 - k_{\bar{K}}^2 - m_{\bar{K}}^2 - \Pi_{\bar{K}}(k_{\bar{K}},\omega,T)}\;, \tag{3.12}$$

being defined the corresponding spectral density as

$$S_{\bar{K}}(k_{\bar{K}},\omega,T) = -\frac{1}{\pi}\mathrm{Im}\, D_{\bar{K}}(k_{\bar{K}},\omega,T)\;. \tag{3.13}$$

We note that, as in the $T = 0$ case, our self-consistent procedure amounts to replace in the $\bar{K}$ propagator the energy dependent self-energy, $\Pi_{\bar{K}}(k_{\bar{K}},\omega,T)$, by that evaluated at the quasiparticle energy, $\Pi_{\bar{K}}(k_{\bar{K}},\omega = E_{\bar{K}}^{qp}(k_{\bar{K}}),T)$. This is what we refer to as the quasi-particle self-consistent approach, which retains the position and the width of the peak of the $\bar{K}$ spectral function at each iteration.

- **Pion**

We also have to pay attention to the temperature effects on the properties of the other hadrons participating in the process. One has to be especially careful with the pion, since its small mass makes it very sensitive to variations in its properties.

As mentioned in the previous chapter, the pion self-energy at $T = 0$ has been obtained following a model that includes the coupling to $1p-1h$, $1\Delta-1h$ and

$2p-2h$ excitations [see Sec. 2.4]. For the finite temperature case, the $1p-1h$ and $1\Delta-1h$ Lindhard functions are modified accordingly.

The effect of temperature in the pion self-energy comes from the modification of the Fermi sea. At a given temperature, nucleons are distributed following the corresponding Fermi distribution. Then, $\mathcal{U}(\vec{q},q^0\,)$ of Eq. (2.46) transforms into

$$\mathcal{U}(\vec{q},q^0,T)=\mathcal{U}_N(\vec{q},q^0,T)+\mathcal{U}_\Delta(\vec{q},q^0,T)\ , \tag{3.14}$$

with

$$\mathcal{U}_N(\vec{q},q^0,T)= \tag{3.15}$$
$$\nu_N\int\frac{d^3k}{(2\pi)^3}\left[\frac{n(\vec{k},T)[1-n(\vec{k}+\vec{q},T)]}{q^0+E_N(\vec{k})-E_N(\vec{k}+\vec{q})+i\eta}+\frac{n(\vec{k}+\vec{q},T)[1-n(\vec{k},T)]}{-q^0-E_N(\vec{k})+E_N(\vec{k}+\vec{q})+i\eta}\right]\ ,$$

and

$$\mathcal{U}_\Delta(\vec{q},q^0,T)= \tag{3.16}$$
$$\nu_\Delta\int\frac{d^3k}{(2\pi)^3}\left[\frac{n(\vec{k},T)}{q^0+E_N(\vec{k})-E_\Delta(\vec{k}+\vec{q})+i\frac{\Gamma(q^0,\vec{q})}{2}}+\frac{n(\vec{k}+\vec{q},T)}{-q^0+E_N(\vec{k}+\vec{q})-E_\Delta(\vec{k})+i\frac{\Gamma(\vec{q},-q^0)}{2}}\right]\ ,$$

where the step function θ for nucleons has been replaced by the distribution $n(\vec{k},T)$ at the corresponding temperature, and ν_N and ν_Δ are

$$\begin{aligned}\nu_N &= 4,\\ \nu_\Delta &= \frac{16}{9}\left(\frac{f^*_\Delta}{f_N}\right)^2,\ \frac{f^*_\Delta}{f_N}=2.13\ .\end{aligned} \tag{3.17}$$

The imaginary part of $\mathcal{U}_N(\vec{q},q^0,T)$ at finite temperature can be obtained analyt-

ically

$$\begin{aligned}
\mathrm{Im}\,\mathcal{U}_N(\vec{q},q^0,T) &= \mathrm{Im}\,\mathcal{U}_N^D(\vec{q},q^0,T)+\mathrm{Im}\,\mathcal{U}_N^C(\vec{q},q^0,T) \\
&= \mathrm{Im}\,\mathcal{U}_N^D(\vec{q},q^0,T)\left(1+\mathrm{e}^{\frac{-q^0}{T}}\right) \ , \\
\mathrm{Im}\,\mathcal{U}_N(\vec{q},q^0,T) &= -\frac{3}{2}\pi\rho\frac{m_N^2\ T}{k_F^3\ q}\ \ln\frac{1-n(p^+,T)}{1-n(p^-,T)}\ \mathrm{cotanh}\left(\frac{q^0}{2T}\right) \ , \qquad (3.18)\\
& \qquad p^+=\frac{m_N}{q}\left|q^0+\frac{\vec{q}^{\,2}}{2m_N}\right| ,\ p^-=\frac{m_N}{q}\left|q^0-\frac{\vec{q}^{\,2}}{2m_N}\right| \ ,
\end{aligned}$$

where $\mathrm{Im}\,\mathcal{U}_N^D(\vec{q},q^0,T)$ and $\mathrm{Im}\,\mathcal{U}_N^C(\vec{q},q^0,T)$ are the imaginary parts of the direct and crossed contributions (first and second terms on the r.h.s. of Eq. (3.15), respectively).

The real part of $\mathcal{U}_N(\vec{q},q^0,T)$ is obtained via the dispersion relation

$$\mathrm{Re}\,\mathcal{U}_N(\vec{q},q^0,T)=-\frac{1}{\pi}P\int d\omega'\ \frac{\mathrm{Im}\,\mathcal{U}_N^D(\vec{q},\omega',T)}{q^0-\omega'}-\frac{1}{\pi}P\int d\omega'\ \frac{\mathrm{Im}\,\mathcal{U}_N^C(\vec{q},\omega',T)}{-q^0+\omega'} \qquad (3.19)$$

or, in a more compact form,

$$\mathrm{Re}\,\mathcal{U}_N(\vec{q},q^0,T)=-\frac{1}{\pi}P\int d\omega'\ \frac{\mathrm{Im}\,\mathcal{U}_N(\vec{q},\omega',T)\ \tanh\left(\frac{\omega'}{2T}\right)}{q^0-\omega'} \ . \qquad (3.20)$$

Eqs. (3.18) and (3.20) define the nucleon Lindhard function at finite T.

As mentioned in the appendix of Ref. [Ose90], the $1\Delta-1h$ Lindhard function at $T=0$, $\mathcal{U}_\Delta(\vec{q},q^0)$, can be derived analytically by neglecting the difference of $\vec{k}^2$ terms in

$$E_N(\vec{k})-E_\Delta(\vec{k}\pm\vec{q})=\frac{\vec{k}^2}{2m_N}-\frac{\vec{k}^2}{2m_\Delta}-\frac{\vec{q}^{\,2}}{2m_\Delta}\mp\frac{\vec{k}\vec{q}}{m_\Delta}+m_N-m_\Delta \ , \qquad (3.21)$$

and assuming that the Δ width only depends on the external variables. We perform the same approximations at finite T. Redefining $\vec{k} + \vec{q} \to -\vec{k}$ in the second term on the r.h.s of Eq. (3.16), such that it becomes the same as the first one but changing $q^0 \to -q^0$, we finally arrive at

$$\begin{aligned} \mathcal{U}_\Delta(\vec{q}, q^0, T) &= \frac{2}{3}\left(\frac{f^*_\Delta}{f_N}\right)^2 \frac{m_\Delta\ \rho}{q\ k_F^3} \int dk\, k\, n(k,T) \\ &\quad \times \left[\ln\left(\frac{z^+ + 1}{z^+ - 1}\right) + \ln\left(\frac{z^- + 1}{z^- - 1}\right)\right] \\ z^\pm &= \frac{m_\Delta}{q\ k}\left(\pm q^0 - \frac{\vec{q}^{\,2}}{2m_\Delta} - (m_\Delta - m_N) + i\frac{\Gamma(\pm q^0, \vec{q})}{2}\right) . \end{aligned} \tag{3.22}$$

The expression for the pion p-wave self-energy at finite temperature reads

$$\begin{aligned} \Pi(\vec{q}, q^0, T) &= F(\vec{q}, q^0)\ \left(\frac{f_N}{m_\pi}\right)^2 \vec{q}^{\,2} \frac{\mathcal{U}(\vec{q}, q^0, T)}{1 - (\frac{f_N}{m_\pi})^2 g' \mathcal{U}(\vec{q}, q^0, T)} \\ \mathcal{U}(\vec{q}, q^0, T) &= \mathcal{U}_N(\vec{q}, q^0, T) + \mathcal{U}_\Delta(\vec{q}, q^0, T) , \end{aligned} \tag{3.23}$$

where $F(\vec{q}, q^0)$ is the form factor,

$$\begin{aligned} F(\vec{q}, q^0) &= \left(\frac{\Lambda^2 - m_\pi^2}{\Lambda^2 - (q^{02} - \vec{q}^{\,2})}\right)^2 \\ \Lambda &= 1200 \text{ MeV} , \end{aligned} \tag{3.24}$$

and g' is the Landau-Migdal parameter described in Ref. [Ose82a]. Eq. (3.23) is equivalent to Eqs. (2.46) obtained at $T = 0$. The total pion self-energy also includes a s-wave piece, as it was done for $T = 0$ [see Eqs. (2.48) and (2.49)].

As for the $T = 0$ case, we can define a pion optical potential, $U_\pi(k_\pi, \omega, T)$, from

the complete π self-energy using the relation

$$U_\pi(k_\pi,\omega,T) = \sqrt{k_\pi^2 + m_\pi^2 + \Pi_\pi(k_\pi,\omega,T)} - \sqrt{k_\pi^2 + m_\pi^2}\ , \qquad (3.25)$$

where we have redefined $\omega \equiv q^0$ and $\vec{k}_\pi \equiv \vec{q}$. The spectral density for π is calculated from Eqs. (3.12) and (3.13), by replacing the $\bar{K}$ properties for those of the π.

- **Nucleon**

In the case of nucleons, we have introduced temperature effects following the Walecka $\sigma - \omega$ model [Ser86], using the density dependent scalar g_s and vector g_v coupling constants at $T = 0$ given in Ref. [Mac89], which mimic Dirac-Brueckner-Hartree-Fock results. In this model, the interaction between nucleons is considered as the result of the exchange of attractive scalar (σ) and repulsive vector (ω) bosons. The Lagrangian density built using this model leads to a series of coupled equations that are solved in a mean-field approximation in nuclear symmetric matter using the Hartree approximation. Solving the meson-field equations in this approach, the vector field Σ^0 turns out to be associated to the baryonic nuclear density $\rho \equiv \langle \Psi\overline{\Psi}\rangle$ of the system while the scalar field Σ^s is related to the so-called scalar density $\rho_s \equiv \langle \Psi^+\Psi\rangle$

$$\Sigma^0 = -\left(\frac{g_v}{m_v}\right)^2 \rho, \qquad \Sigma^s = -\left(\frac{g_s}{m_s}\right)^2 \rho_s$$
$$\rho \equiv \langle \Psi\overline{\Psi}\rangle = \frac{\nu}{(2\pi)^3}\int_0^{k_F} d^3k = \frac{\nu}{6\pi^2}\,k_F^3, \qquad \rho_s \equiv \langle \Psi^+\Psi\rangle\ . \qquad (3.26)$$

The quantities m_v and m_s are the masses of the ω and σ bosons, respectively, ν

is the spin-isospin degeneracy factor of nuclear symmetric matter and Ψ is the nucleon field. The solution of the Dirac equation for nucleons with the scalar and vector fields calculated in this approach gives the following set of relations

$$\begin{aligned} m^* &= m_N + \Sigma^s \ , \\ E_N(k) &= E^*(k) - \Sigma^0 \ , \\ E^*(k) &= \sqrt{k_N^2 + m^{*2}} \ , \end{aligned} \tag{3.27}$$

where m^* and $E_N(k)$ are the Dirac effective mass and the energy spectrum for nucleons, respectively. It is seen that once the Dirac equation is solved, the scalar density ρ_s can be obtained straightforwardly

$$\rho_s = \frac{\nu}{(2\pi)^3} \int_0^{k_F} d^3k \frac{m^*}{E^*(k)} \ . \tag{3.28}$$

In order to obtain the effective mass m^*, a self-consistent process is needed. Using the expressions for the effective mass m^*, the scalar field Σ^s and the scalar density ρ_s, one sees that m^* can be calculated self-consistently according to

$$\begin{aligned} m^* = \quad & m_N - \left(\frac{g_s}{m_s}\right)^2 \frac{\nu}{(2\pi)^3} \int_0^{k_F} d^3k \frac{m^*}{E^*(k)} \\ = \quad & m_N - \left(\frac{g_s}{m_s}\right)^2 \frac{\nu \ m^*}{4 \ \pi^2} \left(k_F E_F^* - (m^*)^2 \ln\left(\frac{k_F + E_F^*}{m^*}\right)\right) \ . \end{aligned} \tag{3.29}$$

The determination of m^* allows us to calculate the quantities that describe the system, such as energy and pressure.

When temperature effects are introduced, a new parameter, the baryonic chemical potentical μ appears. The baryonic chemical potential, μ, the effective mass,

$m^*(T)$, and the vector potential, $\Sigma^0(T)$, should be obtained simultaneously fixing the temperature and the density. The value of μ is defined via the baryonic density, ρ, [see Eqs. (3.5) and (3.6)], where $E_N(k_N, T)$ is the nucleonic energy spectrum at finite temperature

$$E_N(k_N, T) = \sqrt{k_N^2 + m^*(T)^2} - \Sigma^0(T) \ , \tag{3.30}$$

and $\Sigma^0(T)$ and $m^*(T)$ are defined as

$$\begin{aligned} \Sigma^0(T) &= -\left(\frac{g_v}{m_v}\right)^2 \rho \\ m^*(T) &= m - \left(\frac{g_s}{m_s}\right)^2 \frac{\nu}{(2\pi)^3} \int d^3k_N \ n(k_N, T) \ \frac{m^*(T)}{\sqrt{k_N^2 + m^*(T)^2}} \ . \end{aligned} \tag{3.31}$$

These expressions are equivalent to Eqs. (3.26), (3.27) ,(3.28) and (3.29) for the $T = 0$ case. One clearly sees that, given g_s, g_v and a fixed ρ, $\Sigma^0(T)$ is easily obtained. On the other hand, a simultaneous solution of μ and $m^*(T)$ is now needed to determine the nucleonic spectrum. We note that the antiparticle contribution to the density ρ has been proven to be negligible, so it is not considered here.

- **Hyperons Σ and Λ**

  For the hyperons Σ and Λ, we have not considered changes in their properties induced by the use of a given temperature. We have checked, in a schematic Skyrme-Hartree-Fock calculation, that the changes due to the temperature effects are small within the temperature range explored in this work. Hence, the parametrization of the hyperon optical potential in terms of density of Eq. (2.54) is kept.

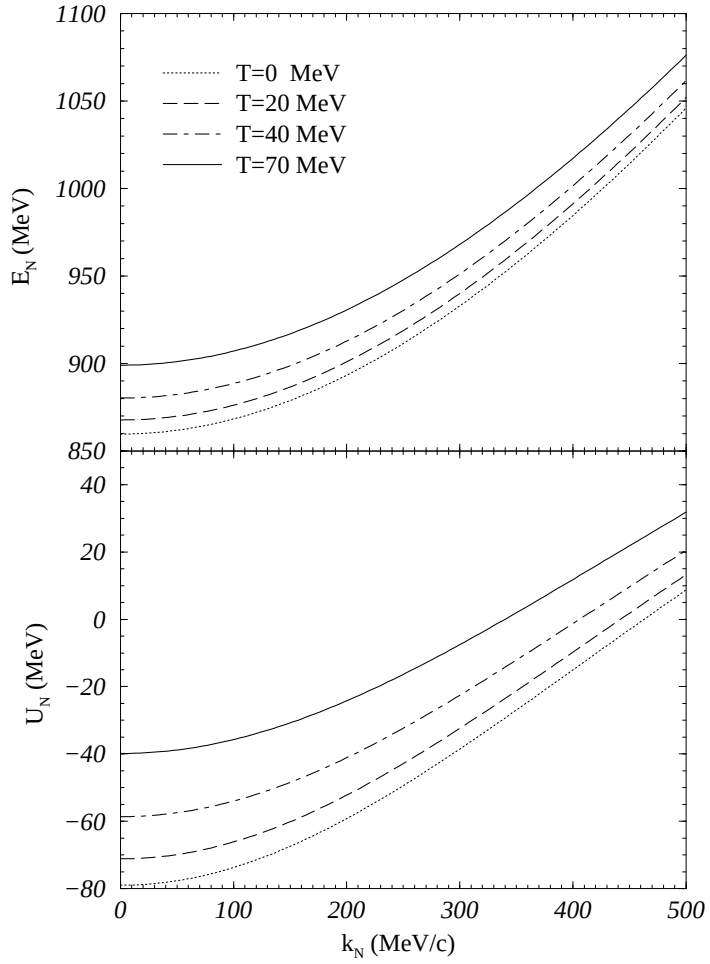

Figure 3.1: Nucleon energy spectrum and nucleon potential at $\rho = 0.17$ fm^{-3} as function of the nucleon momentum for different temperatures.

3.2 Finite temperature results for the $\bar{K}$ optical potential

The starting-point of this section is the study of the effect of the temperature on the nucleon spectrum and the pion self-energy, both of them crucial ingredients for the calculation of $U_{\bar{K}}$. In Fig. 3.1, the nucleon spectrum and the nucleon potential, defined

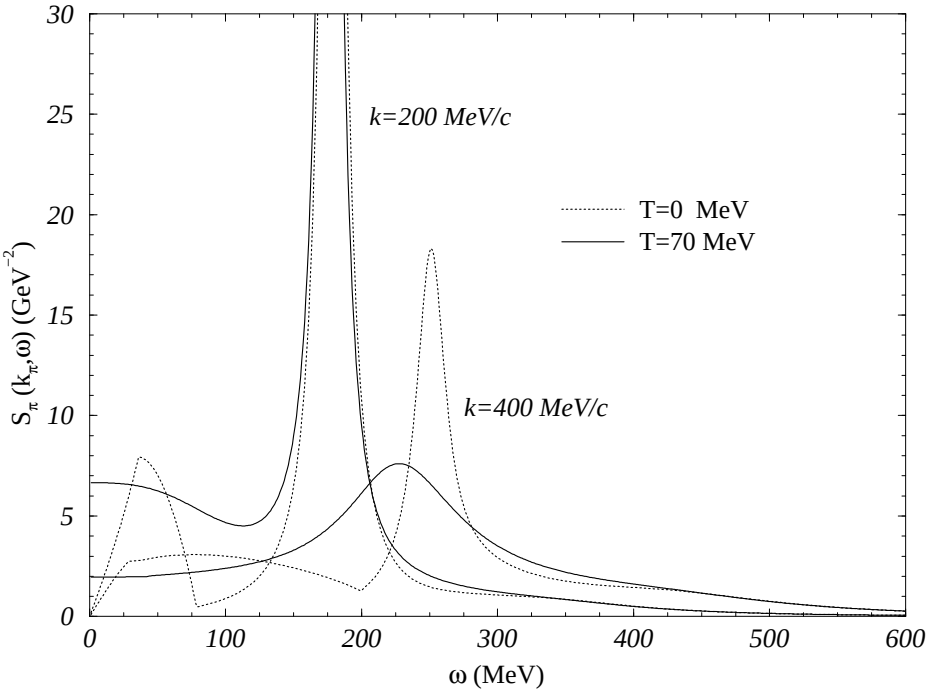

Figure 3.2: Spectral density of the pion at $\rho = 0.17$ fm^{-3} as a function of energy for $k_\pi = 200$ MeV/c and $k_\pi = 400$ MeV/c, and for $T = 0$ MeV and $T = 70$ MeV.

as $U_N = E_N - \sqrt{k_N^2 + m_N^2}$, are given as functions of the nucleon momentum for various temperatures at the nuclear saturation density $\rho_0 = 0.17$ fm^{-3}. The lowest curves in both graphs correspond to $T = 0$ and, as the value of the temperature increases up to $T = 70$ MeV (solid lines), the attractive potential gets reduced from around -80 MeV to -40 MeV at $k_N = 0$. Consequently, the energy spectrum for $k_N = 0$ goes from 860 MeV to 900 MeV. A similar trend is observed for higher values of the nucleon momentum. This behavior is well known for the $\sigma - \omega$ models, as it is reported in Ref. [Ser86].

The next two figures give us information about the pion self-energy and how it is modified by temperature. Figure 3.2 displays the spectral density of the pion as a function of energy at nuclear saturation density, $\rho_0 = 0.17$ fm^{-3}, for two pion momenta,

$k_\pi = 200, 400$ MeV, and two different temperatures, $T = 0$ MeV (dotted lines) and $T = 70$ MeV (solid lines). At $T = 0$, the structure of the $1p - 1h$ excitations can be seen very clearly on the left side of the quasiparticle peak. This structure smooths out as temperature increases. The effect of $1\Delta - 1h$ excitations is more difficult to be identified for these two momenta. It is only somewhat appreciated at $T = 0$ by a slower fall of the spectral function to the right of the quasiparticle peak. The effect of temperature is to move the quasiparticle peak slightly away from the $T = 0$ position towards lower energies, making it noticeably wider.

In Fig. 3.3 we show the pion optical potential as defined in Eqs. (2.51) and (3.25). The real and imaginary parts of the pion optical potential at nuclear saturation density are displayed as functions of the pion momentum, k_π, for different temperatures. The dotted lines correspond to $T = 0$, and the results for the highest temperature studied, $T = 70$ MeV, are represented by the solid ones. In the region of pion momenta explored here, the imaginary part shows a stronger dependence on the temperature than the real part, which is practically T-independent. Note that the quasiparticle energy, which defines the position of the quasiparticle peak in the spectral function, is determined through the real part of the pion self-energy [see Eq. (3.4)], and it is not directly obtained from $\mathrm{Re}\, U_\pi$, where U_π is given in Eq. (2.51) and (3.25). This explains that, while $\mathrm{Re}\, U_\pi$ at $k_\pi = 400$ MeV is practically the same for $T = 0$ and 70 MeV, the location of the peak differs more markedly. Similarly, the width (or height) of the peak for the different temperatures cannot be directly calculated from $\mathrm{Im}\, U_\pi$, but has to be obtained from $\mathrm{Im}\, \Pi_\pi$ at the quasiparticle energy.

Once the pion self-energy is introduced in the calculation of the $\bar{K}$ optical potential, its effects can be studied by comparing the results obtained by dressing only

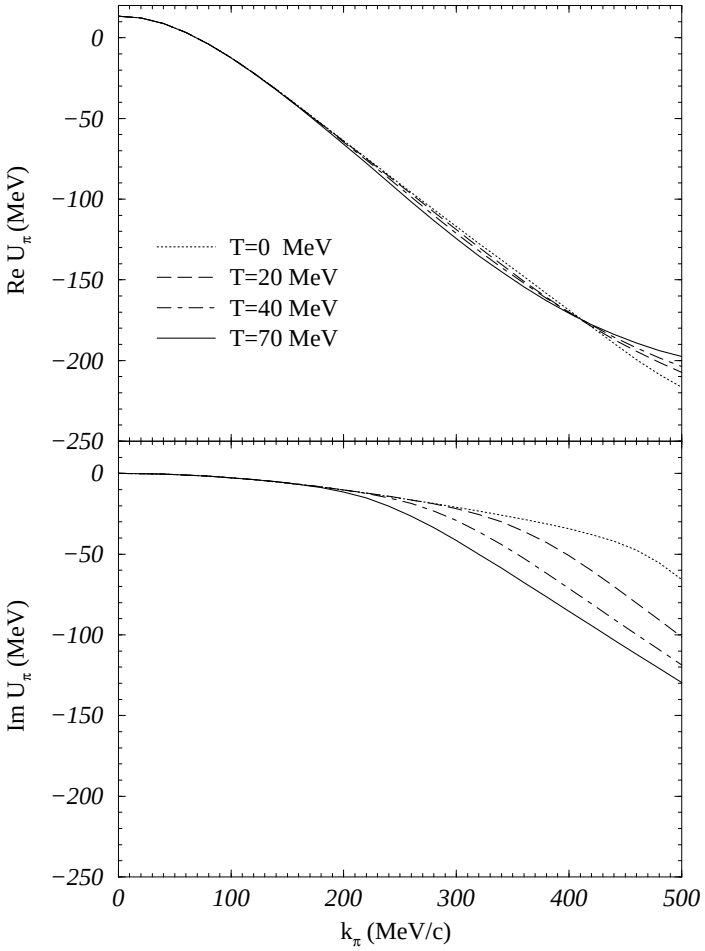

Figure 3.3: Real and imaginary parts of U_π at $\rho = 0.17$ fm^{-3} as functions of the pion momentum for various temperatures.

the $\bar{K}$ mesons with those in which not only the $\bar{K}$ mesons but also the pions in the intermediate meson-baryon states are dressed.

In Fig. 3.4, the real and imaginary parts of the $\bar{K}$ optical potential at nuclear saturation density are shown as functions of the antikaon momentum, $k_{\bar{K}}$, for different temperatures. On the left panels, only the $\bar{K}$ mesons have been dressed, while the results on the right panels incorporate, in addition, the dressing of the pions. Dotted lines correspond to $T = 0$ and solid lines to $T = 70$ MeV. At $T = 0$ we find the same

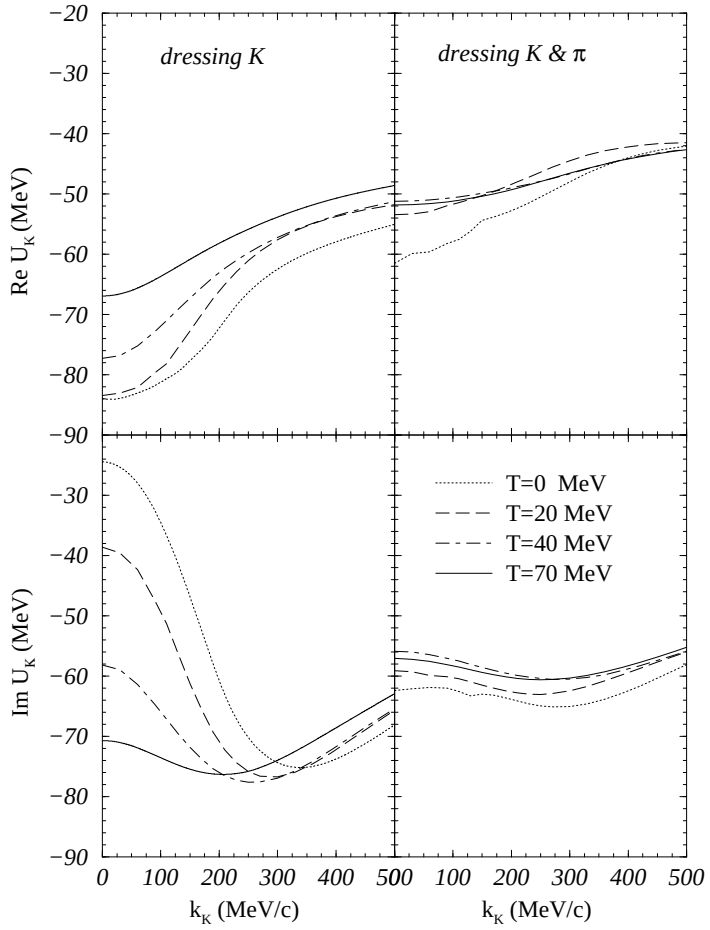

Figure 3.4: Real and imaginary parts of $U_{\bar{K}}$ at $\rho = 0.17$ fm^{-3} as functions of the antikaon momentum for several temperatures, dressing only $\bar{K}$ (left panels) and dressing both $\bar{K}$ and π (right panels).

qualitative effects from dressing the pions as those found by the chiral model [Ram00] shown in Ref. [Ram01a] [see comments in Sec. 2.4].

When temperature increases, we can see on the right panels of Fig. 3.4 that the optical potential loses attraction and absorptive power, although the effect is moderate. The reason is obvious: as it can be seen from Eq. (3.9), and assuming a weak dependence of the effective interaction $G_{\bar{K}N}$ on temperature, at a finite T one is averaging over higher momentum states, where this interaction is weaker. Nevertheless, at suffi-

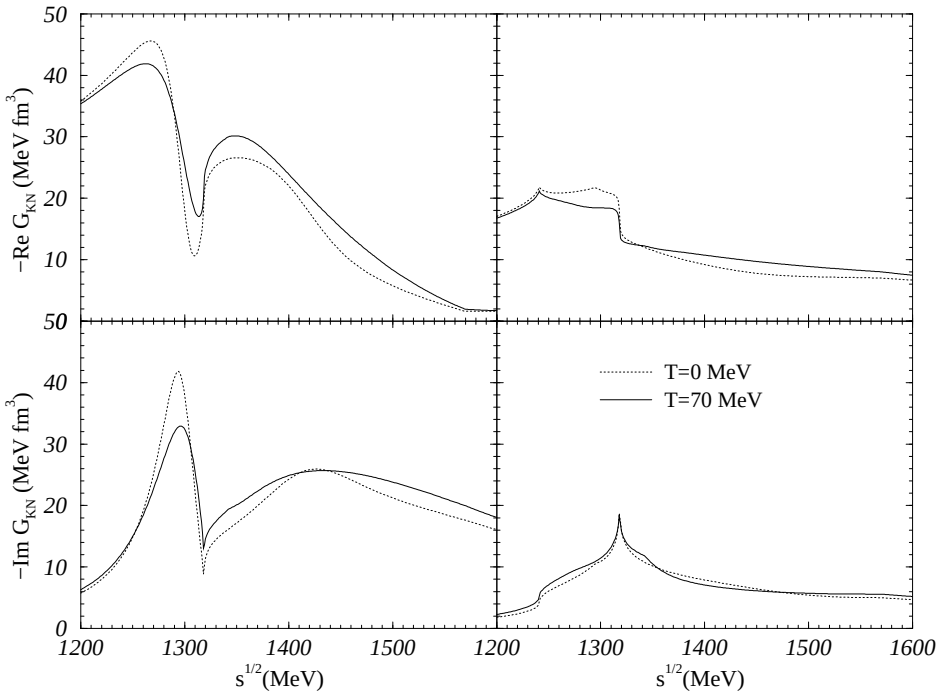

Figure 3.5: Real and imaginary parts of the $\bar{K}N$ amplitude in the $I = 0$, $L = 0$ channel (left panels) and the $I = 1$, $L = 0$ channel (right panels) at $\rho = 0.17$ fm^{-3} as functions of the center-of-mass energy at total momentum $|\vec{k}_{\bar{K}} + \vec{k}_N| = 0$ for $T = 0$ MeV and $T = 70$ MeV.

cient high T [see the 70 MeV results on the right panels of Fig. 3.4], one starts to gain some attraction and absorption. Evidently, this is a consequence of the T-dependence of the effective interaction. To visualize this additional dependence on T, we show in Fig. 3.5, the $\bar{K}N$ amplitude for the channels $L = 0$, $I = 0$ and $L = 0$, $I = 1$, at zero center-of-mass momentum, for two different temperatures, $T = 0$ (dotted lines) and $T = 70$ MeV (solid lines). The general trends of the $\bar{K}N$ amplitude at these two temperatures are similar but there are small differences that explain the behavior observed in the previous figure for the $\bar{K}$ optical potential. Indeed, the $\bar{K}N$ amplitudes involved in the construction of the $\bar{K}$ optical potential correspond to energies above 1300 MeV and, in that region, the magnitude of the real part of the amplitudes at $T = 70$ MeV is larger than the $T = 0$ one, thereby compensating the loss of attraction induced by

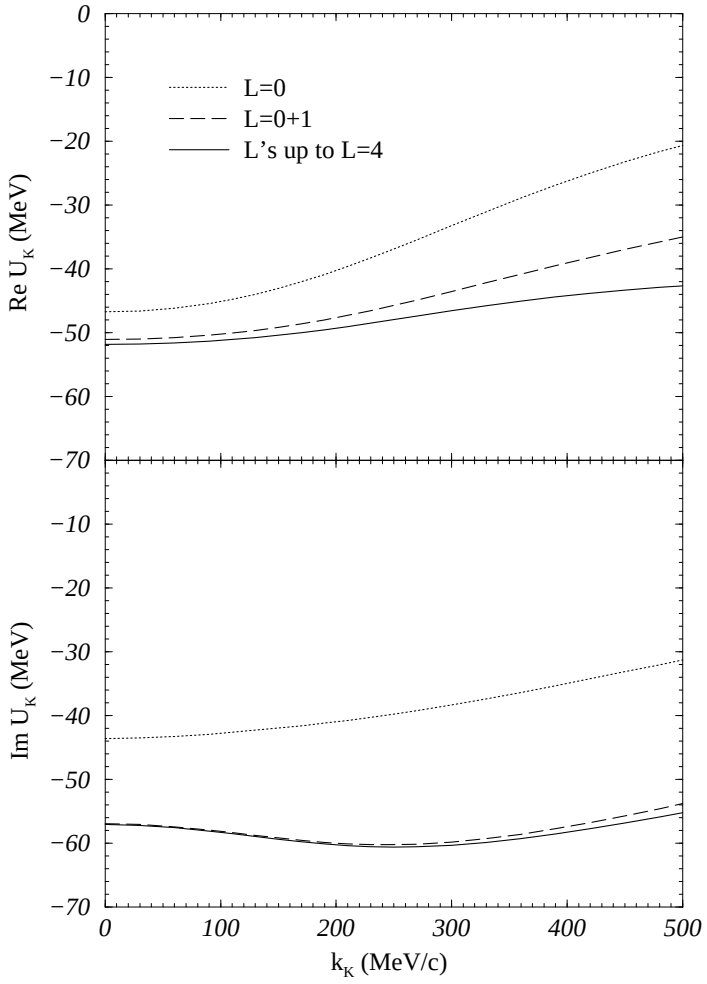

Figure 3.6: Partial wave contributions to the real and imaginary parts of the $\bar{K}$ optical potential at $\rho = 0.17$ fm^{-3} as functions of the antikaon momentum for $T = 70$ MeV.

the higher relative momentum components present in the $\bar{K}$ optical potential at finite T. The structure in the $I = 0$ amplitude below the $\pi\Sigma$ threshold, already commented in Sec. 2.4, is still present even when temperature effects are included.

We have also studied the contributions of angular momentum components larger than $L = 0$ to the antikaon optical potential, as we did for the $T = 0$ case in Chapter 2. In Fig. 3.6 we display the contribution of the different partial waves to the real and imaginary parts of the $\bar{K}$ optical potential at nuclear saturation density and a

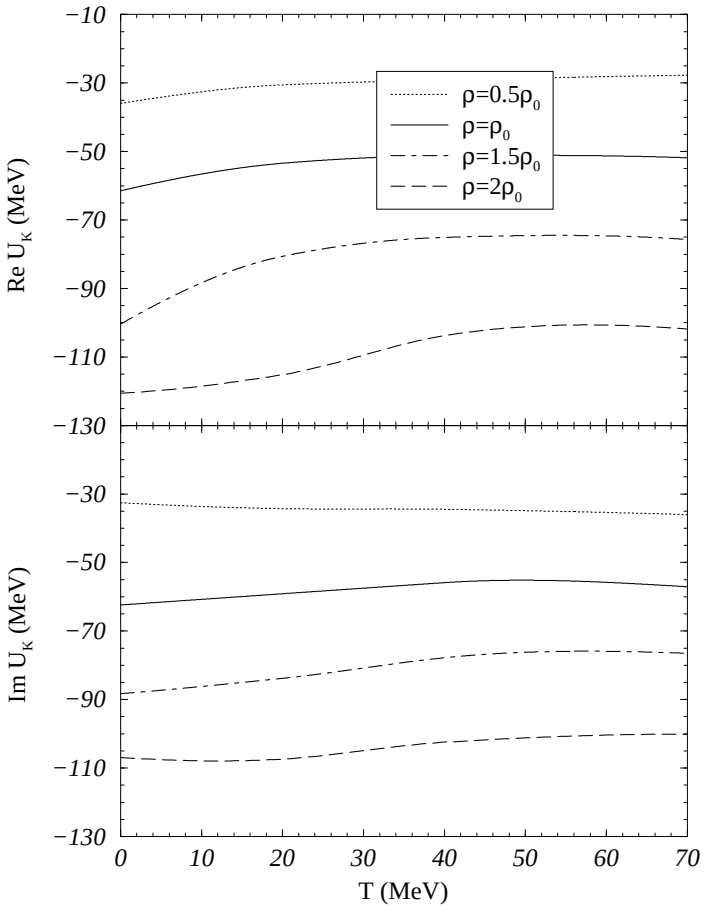

Figure 3.7: Real and imaginary parts of the $\bar{K}$ optical potential as functions of the temperature for different densities.

temperature of $T = 70$ MeV. We observe that adding the higher partial waves to the $L = 0$ contribution up to $L = 4$ produces significant changes. The momentum dependence of the $\bar{K}$ optical potential becomes smoother, the real part becomes more attractive, and the imaginary part increases by about 25% at $k_{\bar{K}} = 0$ and by 50% at momenta around 500 MeV/c.

In Fig. 3.7 we plot the real and imaginary parts of $U_{\bar{K}}$ as functions of temperature for different densities. It is interesting to observe that $U_{\bar{K}}$ depends very weakly on temperature and stays attractive over the whole range of temperatures explored. This

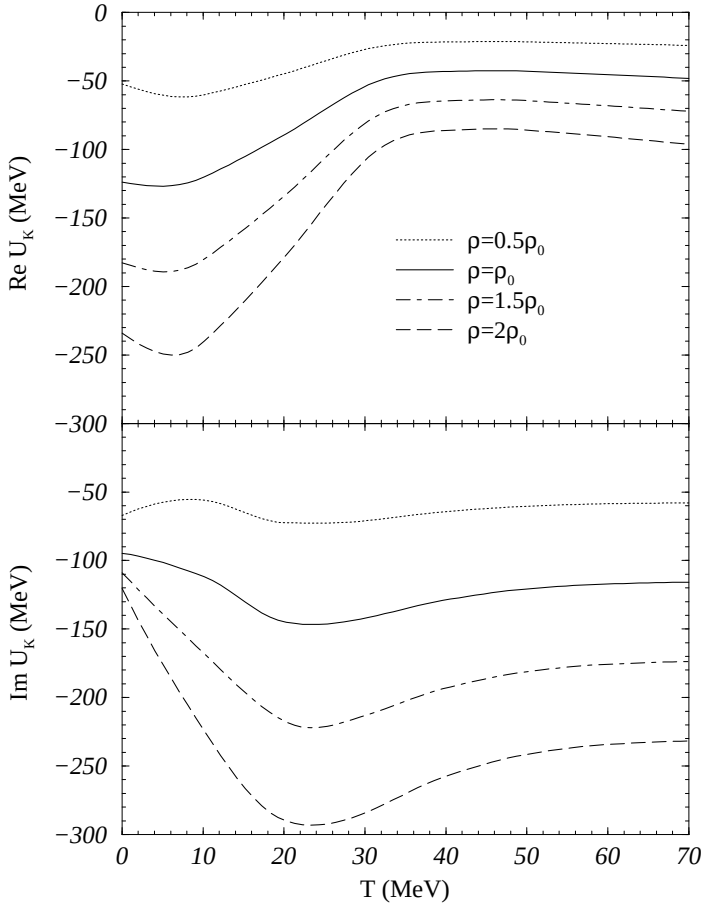

Figure 3.8: Real and imaginary parts of the $\bar{K}$ optical potential as functions of the temperature for different densities only including the Pauli blocking on the nucleons

is qualitatively different from the results shown in Fig. 2 of Ref. [Scha00], where the potential becomes repulsive at a finite temperature of $T = 30$ MeV for $\rho = \rho_0$. We note that, although in that work a self-consistent scheme was also applied, the only source of medium effects in their Fig. 2 was the Pauli blocking of the nucleons in the intermediate states. If only the Pauli blocking is considered, Fig. 3.7 transforms into Fig. 3.8. In this figure, the temperature dependence is not as smooth as seen before in Fig. 3.7 and the potential is still attractive even for $\rho = 2\rho_0$ in the range of temperatures studied. Furthermore, it is observed a tendency to remain attractive

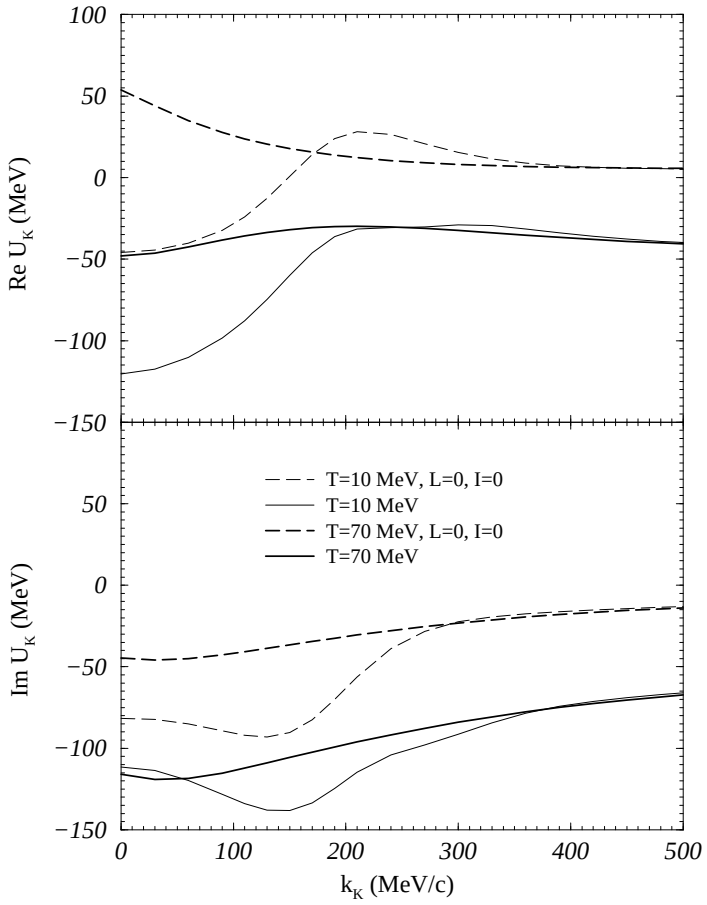

Figure 3.9: Real and imaginary parts of the $\bar{K}$ optical potential as functions of the $\bar{K}$ momentum for $T = 10$ MeV and $T = 70$ MeV at $\rho = \rho_0$ with only Pauli blocking effects, including the $L = 0$, $I = 0$ component separately.

even when the temperature increases. In Ref. [Scha00], the transition from attraction at $T = 0$ to repulsion at finite T is explained by means of the weakened Pauli blocking effects associated to a thermal smearing of the Fermi surface, such that eventually one is recovering the $\rho = 0$ repulsive behavior. To investigate this effect, we plot in Fig. 3.9, the real and imaginary parts of the antikaon optical potential at $\rho = \rho_0$ for $T = 10$ MeV (thin lines) and $T = 70$ MeV (thick lines) as functions of the antikaon momentum, showing explicitly the $L = 0$, $I = 0$ component for those temperatures (dashed lines). We indeed see that the Pauli effects are weaker as temperature increases since for the

$L = 0$, $I = 0$ component of the interaction, the $\bar{K}$ optical potential at $k = 0$ changes from being attractive at $T = 10$ MeV (thin dashed line) to being repulsive at $T = 70$ MeV (thick dashed line) because of recovering the repulsive behaviour of the $\Lambda(1405)$ resonance at $\rho = 0$. However, the features of the complete Jülich $\bar{K}N$ interaction contained in the solid lines make the antikaon optical potential remain attractive for the temperatures and momenta explored, even if only Pauli blocking medium effects have been considered.

The results shown in Fig. 3.7 demonstrate that self-consistency effects have a tremendous influence on the behavior of the $\bar{K}$ optical potential with temperature. In particular, for temperatures as high as 70 MeV, the real part of $U_{\bar{K}}(k_{\bar{K}} = 0)$ at ρ_0 is very similar to that at $T = 0$, having lost only about 10 MeV of attraction. The attraction found here for the $\bar{K}$ optical potential at finite ρ and T, together with enhanced in-medium K^- production cross sections [Ohn97, Scha00], may help to explain the enhanced K^-/K^+ ratio measured at GSI by the KaoS collaboration [Kao90s].

Finally, in Fig. 3.10 we present the $\bar{K}$ spectral function as a function of energy for two momentum values, $k_{\bar{K}} = 0$ and 400 MeV/c, at $T = 0$ (dotted lines) and $T = 70$ MeV (solid lines). The structures observed on the left hand side of the peaks, especially visible for the $T = 0$ spectral functions, are due to the excitation of hyperon-hole states with $\bar{K}$ quantum numbers that are present when the $L = 1$ components of the $\bar{K}N$ interaction are incorporated. We note, however, that the highest peak observed in the $T = 0$ spectral function for $k_{\bar{K}} = 0$ corresponds to the enhancement observed in the $I = 0$ $\bar{K}N$ amplitude below the $\pi\Sigma$ threshold. The inclusion of a finite T washes most of these structures out, and the resulting spectral functions show basically a single pronounced peak. Note that the spectral function at $\rho = \rho_0$ for $T = 0$ in

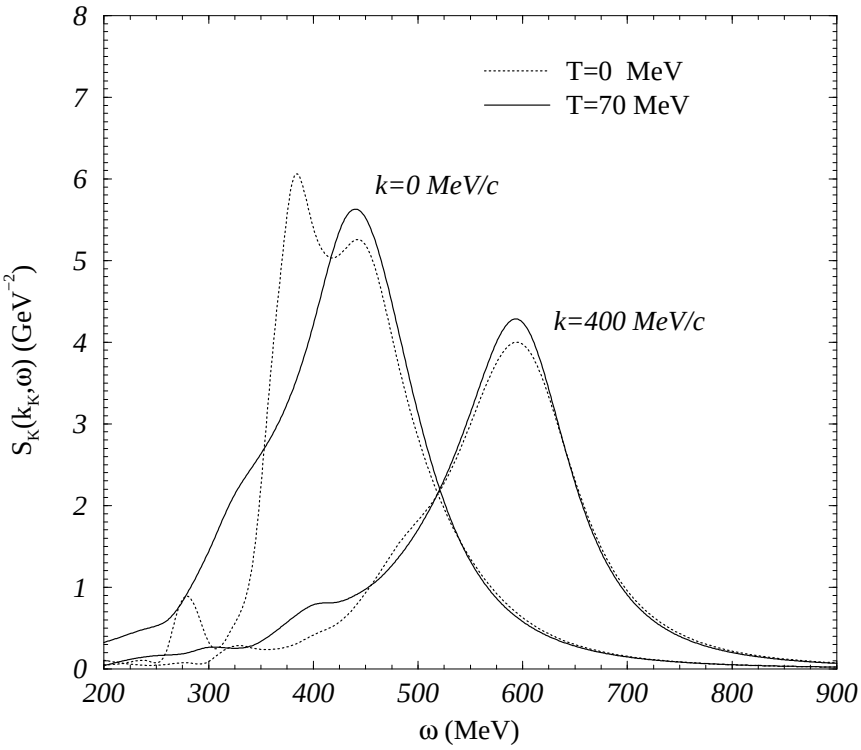

Figure 3.10: Spectral density of the antikaon at $\rho = 0.17$ fm^{-3} as a function of energy for antikaon momenta $k_{\bar{K}} = 0$ and $k_{\bar{K}} = 400$ MeV/c and for $T = 0$ MeV and $T = 70$ MeV.

Fig. 3.10 differs from the spectral function of Fig. 2.9 under the same conditions. This is due to the inclusion of the pion dressing in the $\bar{K}$ self-energy and, therefore, denotes the importance of considering the pion properties with the corresponding in-medium modifications.

Chapter 4

K^-/K^+ ratio at GSI in hot and dense matter

In this chapter the K^-/K^+ ratio produced in heavy-ion collisions at GSI energies is studied including the in-medium properties at finite temperature of the hadrons involved. Particular attention is paid to the in-medium properties of the antikaons, which determine the chemical potential and temperature at freeze-out conditions for a given experimental K^-/K^+ value. The chapter is organized in the following way: the experimental ratio K^-/K^+ is presented in Sec. 4.1 while thermal models are introduced in Sec. 4.2 in order to define the K^-/K^+ ratio in the context of these statistical models. Sec. 4.3 is dedicated to include the antikaon self-energy at finite temperature in the calculation of the K^-/K^+ ratio. The discussion of the effects of dressing the K^- meson on this ratio is left for Sec. 4.4.

4.1 The experimental K^-/K^+ ratio at GSI

Heavy-ion collisions at energies around $1-2$ AGeV offer the possibility of studying experimentally the properties of hadrons in a dense and hot nuclear system [Oes02, Sen01, Stu02]. In particular, a considerable amount of information about antikaons is available. Within the different experimental programs developed, the Kaon Spectrometer (KaoS) of the SIS heavy-ion synchrotron at GSI (Darmstadt) has investigated the production and propagation of kaons and antikaons under extreme conditions of density, around 2-3 nuclear saturation density, and temperature, with values of the order of $T = 70$ MeV. The experiments have been performed with Au+Au, Ni+Ni, C+C at energies between 0.6 and 2.0 AGeV [Ahn97, Bes97, Cro00, Kao90s, Men00, Mis94, Rit95, Shi98, Stu01].

One astonishing observation in C+C and Ni+Ni collisions [Kao90s, Men00] is that, as a function of the energy difference $\sqrt{s} - \sqrt{s}_{th}$, where $\sqrt{s}_{th}$ is the minimum energy to produce the particle (2.5 GeV for K^+ via $pp \to \Lambda K^+ p$ and 2.9 GeV for K^- via $pp \to ppK^-K^+$), the number of K^- balanced the number of K^+ for equivalent energies in spite of the fact that in pp collisions the production cross-sections close to threshold are 2-3 orders of magnitude different. This observation could be explained in terms of an attractive optical potential for K^- meson, although another complementary explanation in terms of an increased production of K^- meson through the πY collisions has also been advocated [Scha00].

On the other hand, equal centrality dependence for K^+ and K^- and, hence, independence of centrality for the K^-/K^+ ratio is also been observed in Au+Au and Pb+Pb reactions between 1.5 AGeV and RHIC energies [Ahl90s, Dun00, For02, Har01, Men00,

Ogi01]. The centrality independence of the K^-/K^+ ratio has often been considered as signaling the lack of in-medium effects. However, Brown et al. [Bro01a, Bro01b] introduced the concept of "broad-band equilibration" according to which the K^- mesons and the hyperons are produced in an essentially constant ratio independent of density. The idea is that the increase in density and hence, the baryonic chemical potential, is compensated by the attraction felt by the antikaon. Therefore, the centrality independence of the K^-/K^+ ratio could also be explained including in-medium effects.

In summary, there is a strong debate about how in-medium effects come into play on the production and propagation of antikaons in heavy-ion collisions, especially at energies of GSI. This chapter is devoted to study the influence of the different ways of dressing the antikaons on the experimental K^-/K^+ ratio, the value of which is 0.031 ± 0.005 for Ni+Ni collisions at GSI [Men00], with the aim of bringing new insight into this problem.

4.2 Thermal Models: the K^-/K^+ ratio

In this section we present a brief description of the thermal models to account for strangeness production in heavy-ion collisions. The basic hypothesis is to assume that the relative abundance of kaons and antikaons in the final state of relativistic nucleus-nucleus collisions is determined by imposing thermal and chemical equilibrium, although only chemical equilibrium is fully justified [Cle98a, Cle99a, Cle98b, Cle99b, Cle99c, Cle00, Hag85]. The fact that the number of strange particles in the final state is small requires a strict treatment of the strangeness conservation and, for this quantum number, one has to work in the canonical scheme. Other conservation laws must also

be imposed, like baryon number and electric charge conservation. Since the number of baryons and charged particles is large, they can be treated in the grand-canonical ensemble. In this way, the conservation laws associated to these other quantum numbers are satisfied on average, allowing for fluctuations around the corresponding mean values.

To restrict the ensemble according to the exact strangeness conservation law, as done in Refs. [Cle98a, Cle99a, Cle98b, Cle99b, Cle99c, Cle00], one has to project the grand-canonical partition function, $\bar{Z}(T, V, \lambda_B, \lambda_S, \lambda_Q)$, onto a fixed value of strangeness S,

$$Z_S(T, V, \lambda_B, \lambda_Q) = \frac{1}{2\pi} \int_0^{2\pi} d\phi \; e^{-iS\phi} \; \bar{Z}(T, V, \lambda_B, \lambda_S, \lambda_Q) \; , \tag{4.1}$$

where $\lambda_B, \lambda_S, \lambda_Q$ are the baryon, strangeness and charge fugacities, respectively, and where λ_S stands explicitly for $\lambda_S = e^{i\phi}$. The exact treatment of the strangeness in statistical mechanics by projecting the partition function onto the desired value of strangeness comes from the application of group theoretical methods (see references [Mul85, Red80s]).

Only particles with $S = 0, \pm 1$ are included in the grand-canonical partition function because, in the range of energies achieved at GSI, they are produced with a higher probability than particles with $S = \pm 2, \pm 3$. The grand-canonical partition function is calculated assuming an independent particle behavior and the Boltzmann approximation for the one-particle partition function of the different particle species. In principle, one deals with a dilute system, so the independent particle model seems justified. However, medium effects on the particle properties can be relevant. As mentioned

previously, the aim of this paper is to study how the dressing of the hadrons present in the gas, especially the antikaons, affects the observables such as the ratio of kaon and antikaon particle multiplicities, in particular for the conditions of the heavy-ion collisions at SIS/GSI energies.

Within the approximations mentioned above, the grand-canonical partition function reads as follows,

$$\bar{Z}(T,V,\lambda_B,\lambda_S,\lambda_Q) = \exp(N_{S=0} + N_{S=-1}e^{-i\phi} + N_{S=1}e^{i\phi}) \ , \tag{4.2}$$

where $N_{S=0,\pm1}$ is the sum over one-particle partition functions of all particles and resonances with strangeness $S = 0, \pm 1$,

$$N_{S=0,\pm1} = \sum_{B_i} Z^1_{B_i} + \sum_{M_j} Z^1_{M_j} + \sum_{R_k} Z^1_{R_k} \ , \tag{4.3}$$

$$Z^1_{B_i} = g_{B_i}\, V \int \frac{d^3k}{(2\pi)^3}\, e^{\frac{-E_{B_i}}{T}}\, e^{\frac{\mu_{B_i}}{T}}\, e^{\frac{\mu_{Q(B_i)}}{T}} \ , \tag{4.4}$$

$$Z^1_{M_j} = g_{M_j}\, V \int \frac{d^3k}{(2\pi)^3}\, e^{\frac{-E_{M_j}}{T}}\, e^{\frac{\mu_{Q(M_j)}}{T}} \ ,$$

$$Z^1_{R_k} = g_{R_k}\, V \int \frac{d^3k}{(2\pi)^3} \int_{m-2\Gamma}^{m+2\Gamma} ds\, e^{\frac{-\sqrt{k^2+s}}{T}} \frac{1}{\pi} \frac{m\Gamma}{(s-m^2)^2 + m^2\Gamma^2} \left(e^{\frac{\mu_B(R_k)}{T}}\right)\, e^{\frac{\mu_Q(R_k)}{T}} \ .$$

The expressions $Z^1_{B_i}$ and $Z^1_{M_j}$ of Eq. (4.4) indicate the one-particle partition function for baryons and mesons respectively, while $Z^1_{R_k}$ is the one-particle partition function associated to a baryonic or mesonic resonance. In this latter case, however, the factor $e^{\frac{\mu_B(R_k)}{T}}$ would not be present. Notice that the resonance is described by means of a Breit-Wigner parameterization. The quantity V is the interacting volume of the system, g_B, g_M and g_R are the spin-isospin degeneracy factors and μ_B and μ_Q are the baryonic and charge chemical potentials of the system. For Ni+Ni system at SIS energies, μ_Q

can be omitted because it is associated to the isospin-asymmetry of the system and, in this case, the deviation from the isospin-symmetric case is only 4% (see Ref. [Cle98b]). On the other hand, μ_B will be fixed to the nucleonic chemical potential, μ_N, because the abundance of nucleons is larger than the one for the other baryons produced. The energies E_B, E_M refer to the in-medium single-particle energies of the hadrons present in the system at a given temperature.

Following Ref. [Cle98b], the canonical partition function for total strangeness $S = 0$ is

$$Z_{S=0}(T, V, \lambda_B) = \frac{1}{2\pi} \int_0^{2\pi} d\phi \, \exp(N_{S=0} + N_{S=-1} e^{-i\phi} + N_{S=1} e^{i\phi}) \; . \tag{4.5}$$

In that work, as well as in Ref. [Cle99b], the small and large volume limits of the particle abundances were studied. These limits were performed to show that the canonical treatment of strangeness for obtaining the particle abundances gives completely different results in comparison to the grand-canonical scheme, demonstrating at the same time that, for the volume considered, the canonical scheme is the appropriate one. The aim of going through these limits again in the following is to remind the reader that, for the specific case of the ratio K^-/K^+, the result is independent of the size of the system and is the same for both the canonical and grand-canonical treatments.

According to statistical mechanics, to compute the number of kaons and antikaons [Hag85] one has to differentiate the partition function with respect to the particle

fugacity

$$N_{K^-(K^+)} \equiv \left(\lambda_{K^-(K^+)} \frac{\partial}{\partial \lambda_{K^-(K^+)}} \ln Z_{S=0}(\lambda_{K^-(K^+)}) \right)_{\lambda_{K^-(K^+)}=1} . \tag{4.6}$$

Expanding $Z_{S=0}$ in the small volume limit, N_{K^-} and N_{K^+} are given by

$$\begin{aligned} N_{K^+} &= g_{K^+} V \int \frac{d^3k}{(2\pi)^3} e^{\frac{-E_{K^+}}{T}} \times \\ &\left\{ \sum_i g_i V \int \frac{d^3k}{(2\pi)^3} e^{\frac{-E_{B_i(S=-1)}+\mu_{B_i}}{T}} + \sum_j g_j V \int \frac{d^3k}{(2\pi)^3} e^{\frac{-E_{M_j(S=-1)}}{T}} + \sum_k Z_{R_{k(S=-1)}} \right\} , \\ N_{K^-} &= g_{K^-} V \int \frac{d^3k}{(2\pi)^3} e^{\frac{-E_{K^-}}{T}} \times \\ &\left\{ \sum_j g_j V \int \frac{d^3k}{(2\pi)^3} e^{\frac{-E_{M_j(S=+1)}}{T}} + \sum_k Z_{R_{k(S=+1)}} \right\} . \end{aligned} \tag{4.7}$$

and the ratio reads

$$\frac{N_{K^-}}{N_{K^+}} \equiv \frac{K^-}{K^+} = \frac{Z^1_{K^-}}{Z^1_{K^+}} \frac{Z^1_{K^+} + Z^1_{M,S=+1}}{Z^1_{K^-} + \lambda_B \, Z^1_{B,S=-1} + Z^1_{M,S=-1}} , \tag{4.8}$$

where we have substituted the explicit expression for the $K^-(K^+)$ partition function by the schematic notation $Z^1_{K^-}(Z^1_{K^+})$ and where $Z^1_{B,S=\pm1}(Z^1_{M,S=\pm1})$ is the sum of one-particle partition functions for baryons (mesons) with $S = \pm 1$.

Antibaryons have not been considered here because the ratio $\frac{\bar{B}}{B} = e^{-\frac{2\mu_B}{T}}$ is negligibly small at GSI/SIS colliding energies, where B and $\bar{B}$ represent the number of baryons and antibaryons, respectively. The expression for N_{K^+} (N_{K^-}) indicates that the number of $K^+(K^-)$ has to be balanced with all particles and resonances with $S = -1 (S = 1)$. It can be observed in Eq. (4.8) that the ratio K^-/K^+ for small volume in the canonical ensemble does not depend on the volume because it cancels

out exactly.

At the other extreme, i.e. in the thermodynamic limit (large volumes), since it is known that the canonical treatment is equivalent to the grand canonical one, one can compute the ratio explicitly from the grand-canonical partition function $\bar{Z}(T, V, \lambda_B, \lambda_S)$,

$$\ln \bar{Z}(T, V, \lambda_B, \lambda_S) = \lambda_S Z^1_{K^+} + \frac{1}{\lambda_S} Z^1_{K^-} + \lambda_B \frac{1}{\lambda_S} Z^1_{B,S=-1} + \lambda_S Z^1_{M,S=+1} + \frac{1}{\lambda_S} Z^1_{M,S=-1}, \quad (4.9)$$

Then, by imposing strangeness conservation on average,

$$\langle S \rangle = \lambda_S \frac{\partial}{\partial \lambda_S} \ln \bar{Z} = 0 \ , \quad (4.10)$$

one can easily obtain λ_S,

$$\lambda_S^2 = \frac{Z^1_{K^-} + \lambda_B \ Z^1_{B,S=-1} + Z^1_{M,S=-1}}{Z^1_{K^+} + Z^1_{M,S=+1}} \ . \quad (4.11)$$

Therefore, from

$$\begin{aligned} \langle N_{K^+} \rangle &= \lambda_S \ Z^1_{K^+} \ , \\ \langle N_{K^-} \rangle &= \frac{1}{\lambda_S} \ Z^1_{K^-} \ , \end{aligned} \quad (4.12)$$

one obtains the ratio

$$\frac{K^-}{K^+} = \frac{Z^1_{K^-}}{Z^1_{K^+}} \ \frac{Z^1_{K^+} + Z^1_{M,S=+1}}{Z^1_{K^-} + \lambda_B \ Z^1_{B,S=-1} + Z^1_{M,S=-1}} \ . \quad (4.13)$$

The condition $\langle S \rangle = 0$ dealing with strange particles of $S = 0, \pm 1$ makes the ratio be independent of the volume.

Although the expression obtained is the same as that from the canonical ensemble in the small volume limit, the proof that the ratio K^-/K^+ is independent of the volume has to be obtained from a general intermediate size situation.

This was shown to be the case in Ref. [Cle99c]. The idea is to expand $Z_{S=0}(T,V,\lambda_B)$ of Eq. (4.5) in power series

$$Z_{S=0}(T,V,\lambda_B) = Z_0 \frac{1}{2\pi} \int_0^{2\pi} d\phi \sum_{m=0}^{\infty} \sum_{n=0}^{\infty} \frac{1}{m!} \frac{1}{n!} N_{S=1}^m N_{S=-1}^n \exp(im\phi) \exp(-in\phi), \quad (4.14)$$

where Z_0 is the partition function that includes all particles and resonances with $S = 0$.

Performing the integral over ϕ, we obtain

$$Z_{S=0}(T,V,\lambda_B) = Z_0 \sum_{n=0}^{\infty} \frac{1}{n!^2} \left(N_{S=1}\ N_{S-1}\right)^n , \quad (4.15)$$

where one can recognize the modified Bessel function $I_0(x_1)$ in the form of a series expansion, i.e., $Z_{S=0}(T,V,\lambda_B) = Z_0 I_0(x_1)$ with $x_1 = 2\sqrt{N_{S=1}N_{S=-1}}$. Using Eq. (4.6), the number of kaons and antikaons is given by

$$\begin{aligned} N_{K^+} &= Z^1_{K^+} \frac{N_{S=-1}}{\sqrt{N_{S=1}N_{S-1}}} \frac{I_1(x_1)}{I_0(x_1)} , \\ N_{K^-} &= Z^1_{K^-} \frac{N_{S=1}}{\sqrt{N_{S=1}N_{S=-1}}} \frac{I_1(x_1)}{I_0(x_1)} , \end{aligned} \quad (4.16)$$

so the computed $N_{K^-}/N_{K^+} \equiv K^-/K^+$ ratio gives precisely the same expression as those given here for small [Eq.(4.8)] and large [Eq.(4.13)] volumes. Therefore, as noted in Ref. [Cle99b], the K^-/K^+ ratio is independent of the volume and, consequently, independent on whether it is calculated in the canonical or grand-canonical schemes.

4.3 The influence of the K^- self-energy on the ratio

In this section we study how the in-medium modifications of the properties of the hadrons at finite temperature affect the value of the K^-/K^+ ratio, focusing our attention on the properties of the antikaons in hot and dense matter. For consistency with previous papers, we prefer to compute the inverse ratio K^+/K^-. As it was mentioned before, the number of K^- (K^+) has to be balanced by particles and resonances with $S = +1 (S = -1)$ in order to conserve strangeness exactly. For balancing the number of K^+, the main contribution in the $S = -1$ sector comes from the Λ and Σ hyperons and, in a smaller proportion, from the K^- mesons. In addition, the effect of the $\Sigma^*(1385)$ resonance is also considered because it is comparable to that of the K^- mesons. On the other hand, the number of K^- is only balanced by the presence of K^+. Then, we can write the K^+/K^- ratio as,

$$\frac{K^+}{K^-} = \frac{Z^1_{K^+}(Z^1_{K^-} + Z^1_\Lambda + Z^1_\Sigma + Z^1_{\Sigma^*})}{Z^1_{K^-} Z^1_{K^+}} = 1 + \frac{Z^1_\Lambda + Z^1_\Sigma + Z^1_{\Sigma^*}}{Z^1_{K^-}} \,, \tag{4.17}$$

where the Z's indicate the different one-particle partition functions for K^-, K^+, Λ, Σ and Σ^*, and, for baryons, they now contain the corresponding fugacity. It is clear from Eq. (4.17) that the relative abundance of Λ, Σ and Σ^* baryons with respect to that of K^- mesons determines the value of the ratio.

In order to introduce the in-medium and temperature effects, the particles involved in the calculation of the ratio are dressed according to their properties in the hot and dense medium in which they are embedded. For the Λ and Σ hyperons, the partition

function

$$Z_{\Lambda,\Sigma} = g_{\Lambda,\Sigma} V \int \frac{d^3k_{\Lambda,\Sigma}}{(2\pi)^3} e^{\frac{-E_{\Lambda,\Sigma}+\mu_N}{T}} \ , \tag{4.18}$$

is built using a mean-field dispersion relation for the single-particle energies

$$E_{\Lambda,\Sigma} = \sqrt{k^2_{\Lambda,\Sigma} + m^2_{\Lambda,\Sigma}} + U_{\Lambda,\Sigma}(\rho) \ . \tag{4.19}$$

For $U_\Lambda(\rho)$, we take the parameterization of Ref. [Bal97], $U_\Lambda(\rho) = -340\rho + 1087.5\rho^2$. For $U_\Sigma(\rho)$, we take a repulsive potential, $U_\Sigma(\rho) = 30\rho/\rho_0$, extracted from analysis of Σ-atoms and Σ-nucleus scattering [Mar95, Daw99], where $\rho_0 = 0.17$ fm^{-3} is the saturation density of symmetric nuclear matter. A repulsive Σ potential is compatible with the absence of any bound state or narrow peaks in the continuum in a recent Σ-hypernuclear search done at BNL [Bar99].

On the other hand, the $\Sigma^*(1385)$ resonance is described by a Breit-Wigner shape,

$$Z_{\Sigma*} = g_{\Sigma^*} V \int \frac{d^3k_{\Sigma^*}}{(2\pi)^3} \int_{m_{\Sigma^*}-2\Gamma}^{m_{\Sigma^*}+2\Gamma} ds \, e^{\frac{-\sqrt{k^2_{\Sigma^*}+s}}{T}} \frac{1}{\pi} \frac{m_{\Sigma^*}\Gamma}{(s-m^2_{\Sigma^*})^2 + m^2_{\Sigma^*}\Gamma^2} \, e^{\frac{\mu_N}{T}} \ , \tag{4.20}$$

with $m_{\Sigma^*} = 1385$ MeV and $\Gamma = 37$ MeV.

In the case of K^+ we take

$$Z_{K^+} = g_{K^+} V \int \frac{d^3k_{K^+}}{(2\pi)^3} e^{\frac{-E_{K^+}}{T}} \ , \tag{4.21}$$

$$E_{K^+} = \sqrt{k^2_{K^+} + m^2_{K^+}} + U_{K^+}(\rho) \ , \tag{4.22}$$

where $U_{K^+}(\rho) = 32\rho/\rho_0$ is obtained from a $t\rho$ approximation, as discussed in Refs.[Kai95,

Ose01].

A particular effort has been invested in studying the antikaon properties in the medium since the $\bar{K}N$ has a particularly rich structure due to the presence of the $\Lambda(1405)$ resonance [Lut98a, Ram00, Scha00, Tol01a]. The antikaon optical potential in hot and dense nuclear matter has recently been obtained [Tol02] within the framework of a coupled-channel self-consistent calculation taking, as bare meson-baryon interaction, the meson-exchange potential of the Jülich group [Mul90]. In order to understand the influence of the in-medium antikaon properties on the K^+/K^- ratio, two different prescriptions for the single-particle energy of the antikaons have been considered.

First, it has been used the so-called on-shell or mean-field approximation to the antikaon single-particle energy. The antikaon partition function in this approach reads

$$\begin{aligned} Z_{K^-} &= g_{K^-} V \int \frac{d^3k_{K^-}}{(2\pi)^3} e^{\frac{-E_{K^-}}{T}} \ , \\ E_{K^-} &= \sqrt{k^2_{K^-} + m^2_{K^-}} + U_{K^-}(k_{K^-}, E_{K^-}, \rho, T) \ , \end{aligned} \tag{4.23}$$

where $U_{K^-}(k_{K^-}, E_{K^-}, \rho, T)$ is the K^- single-particle potential in the Brueckner-Hartree-Fock approach given by

$$U_{K^-}(k_{K^-}, E_{K^-}, \rho, T) = \mathrm{Re} \int d^3k \ n(k,T) \langle \bar{K}N \mid G_{\bar{K}N \to \bar{K}N}(\Omega = E_N + E_{\bar{K}}, T) \mid \bar{K}N \rangle \ , \tag{4.24}$$

which is built from a self-consistent effective $\bar{K}N$ interaction in nuclear symmetric matter, averaging over the occupied nucleonic states according to the Fermi distribution at a given temperature, $n(k,T)$.

The second approach incorporates the complete energy-and-momentum dependent

K^- self-energy

$$\Pi_{K^-}(k_{K^-},\omega,\rho,T) = 2\,\sqrt{k^2_{K^-}+m^2_{\bar{K}}}\;U_{K^-}(k_{K^-},\omega,\rho,T)\;, \tag{4.25}$$

via the corresponding $\bar{K}$ spectral density

$$S_{K^-}(k_{K^-},\omega,\rho,T) = -\frac{1}{\pi}\mathrm{Im}\,D_{K^-}(k_{K^-},\omega,\rho,T)\;, \tag{4.26}$$

where

$$D_{K^-}(k_{K^-},\omega,\rho,T) = \frac{1}{\omega^2 - k^2_{K^-} - m^2_{K^-} - \Pi_{K^-}(k_{K^-},\omega,\rho,T)}\;, \tag{4.27}$$

stands for the K^- propagator. In this case, the K^- partition function reads

$$Z_{K^-} \;=\; g_{K^-}V\int\frac{d^3k_{K^-}}{(2\pi)^3}\int ds\;S_{K^-}(k_{K^-},\sqrt{s},\rho,T)\;e^{\frac{-\sqrt{s}}{T}} \tag{4.28}$$

where $s=\omega^2$.

We note, however, that only the s-wave contribution of the Jülich $\bar{K}N$ interaction has been kept. The reason is that the $\bar{K}N$ potential presents some short-comings in the $L=1$ partial wave, which manifest especially in the low energy region of the K^- self-energy, as already pointed out in Chapter 1. Specifically, the Λ and Σ poles of the $\bar{K}N$ T-matrix come out by about 100 MeV lower than the physical values and, consequently, the corresponding strength in the antikaon spectral function due to hyperon-hole excitations appears at too low energies, a region very important for the calculation we are conducting here. In addition, the role of the $\Sigma^*(1385)$ pole, which lies below the $\bar{K}N$ threshold, is not included in the Jülich $\bar{K}N$ interaction. In order to overcome these problems, we have added to our s-wave K^- self-energy the

p-wave contribution as calculated in Ref. [Ose01]. In this model, the p-wave self-energy comes from the coupling of the K^- meson to hyperon-hole (YN^{-1}) excitations, where Y stands for Λ, Σ and Σ^*. In symmetric nuclear matter at $T = 0$, this self-energy is

$$\begin{aligned}
\Pi_{K^-}^{p-wave}(\vec{k},\omega,\rho) &= \frac{1}{2}\left(\frac{g_{\bar{K}N\Lambda}}{2M}\right)^2 \vec{k}^{\,2} f_\Lambda^2\, \mathcal{U}_\Lambda(\vec{k},\omega,\rho) \\
&+ \frac{3}{2}\left(\frac{g_{\bar{K}N\Sigma}}{2M}\right)^2 \vec{k}^{\,2} f_\Sigma^2\, \mathcal{U}_\Sigma(\vec{k},\omega,\rho) \\
&+ \frac{1}{2}\left(\frac{g_{\bar{K}N\Sigma^*}}{2M}\right)^2 \vec{k}^{\,2} f_{\Sigma^*}^2\, \mathcal{U}_{\Sigma^*}(\vec{k},\omega,\rho) \qquad (4.29)
\end{aligned}$$

The quantities $g_{\bar{K}N\Lambda}$, $g_{\bar{K}N\Sigma}$ and $g_{\bar{K}N\Sigma^*}$ are the $\bar{K}N\Lambda$, $\bar{K}N\Sigma$ and $\bar{K}N\Sigma^*$ coupling constants, while f_Λ, f_Σ, f_{Σ^*} are the Λ, Σ, Σ^* relativistic recoil vertex corrections and $\mathcal{U}_\Lambda$, $\mathcal{U}_\Sigma$, $\mathcal{U}_{\Sigma^*}$ the Lindhard functions at $T = 0$. Following Ref.[Ose01], the Lindhard function for $Y = \Lambda$, Σ or Σ^* is obtained from

$$\mathcal{U}_Y(\vec{k}_Y,\omega,\rho) = \nu_Y \int \frac{d^3k}{(2\pi)^3} \frac{\theta(k_F - k)}{\omega + E_N(\vec{k}) - E_Y(\vec{k}+\vec{k}_Y) + i\eta} \qquad (4.30)$$

where ν_Y contains the sum over spin-isospin degrees of freedom in symmetric nuclear matter. The final expression for $T = 0$, given in Ref.[Ose90, Ose01], is

$$\begin{aligned}
\mathcal{U}_Y(\vec{k}_Y,\omega,\rho) &= \mathrm{Re}\,\mathcal{U}_Y(\vec{k}_Y,\omega,\rho) + i\,\mathrm{Im}\,\mathcal{U}_Y(\vec{k}_Y,\omega,\rho)\ , \\
\mathrm{Re}\,\mathcal{U}_Y(\vec{k}_Y,\omega,\rho) &= \frac{3}{2}\rho\frac{m_Y}{k_Y k_F}\left\{ z + \frac{1}{2}(1-z^2)\ln\frac{|z+1|}{|z-1|}\right\}\ , \\
\mathrm{Im}\,\mathcal{U}_Y(\vec{k}_Y,\omega,\rho) &= -\frac{3}{4}\pi\rho\frac{m_Y}{k_Y k_F}\{(1-z^2)\theta(1-|z|)\}\ , \qquad (4.31)
\end{aligned}$$

with

$$z = \frac{m_Y}{k_Y k_F}\left\{\omega - \frac{\vec{k}_Y{}^2}{2m_Y} - (m_Y - m_N)\right\}\ , \qquad (4.32)$$

where m_Y and m_N are the masses of the hyperon and nucleon, respectively. Actually,

Eq. (4.30) can be obtained from Eq. (2.43) by ignoring, due to strangeness conservation, the crossed-term contribution and making the width $\Gamma = 0$ not only in the case of the stable Λ and Σ hyperons but also, for simplicity, in the case of the Σ^* hyperon. Moreover, the spin-isospin degeneracy factor in Eq. (2.43) has to be changed accordingly.

The relevance of this low energy region makes advisable to extend this p-wave contribution to finite temperature. In this case, the function $\theta(k_F - k)$ in Eq. (4.30) should be substituted by the corresponding Fermi distribution, $n(k,T)$ and one obtains

$$\begin{aligned}
\mathcal{U}_Y(\vec{k}_Y,\omega,\rho,T) &= \mathrm{Re}\,\mathcal{U}_Y(\vec{k}_Y,\omega,\rho,T) + i\,\mathrm{Im}\,\mathcal{U}_Y(\vec{k}_Y,\omega,\rho,T)\ , \\
\mathrm{Re}\,\mathcal{U}_Y(\vec{k}_Y,\omega,\rho,T) &= \frac{3}{2}\rho\frac{m_Y}{k_Y k_F^3}\int dk\ k\ n(k,T)\ \ln\frac{|z+1|}{|z-1|}\ , \\
\mathrm{Im}\,\mathcal{U}_Y(\vec{k}_Y,\omega,\rho,T) &= -\frac{3}{2}\pi\rho\, m_N\, T\frac{m_Y}{k_Y k_F^3}\ \ln\frac{1}{1-n(k_m)}\ ,
\end{aligned} \tag{4.33}$$

with

$$\begin{aligned}
z &= \frac{m_Y}{k_Y k}\left\{\omega - \frac{\vec{k}_Y{}^2}{2m_Y} - (m_Y - m_N)\right\}\ , \\
k_m &= \frac{m_Y}{k_Y}\left|\omega - (m_Y - m_N) - \frac{\vec{k}_Y{}^2}{2m_Y}\right|\ .
\end{aligned} \tag{4.34}$$

This expression can also be directly obtained from the the Δ Lindhard function at finite temperature of Eq. (3.22), taking the width Γ zero, which allows to obtain the imaginary part of $\mathcal{U}_Y$ analytically. The crossed term is again ignored due to strangeness conservation and the spin-isospin degeneracy factors and coupling constants need to be accomodated to the notation used in Eq. (4.29), which amounts to replace $2f^*_\Delta/3f_N$ in Eq. (3.22) by 3/2.

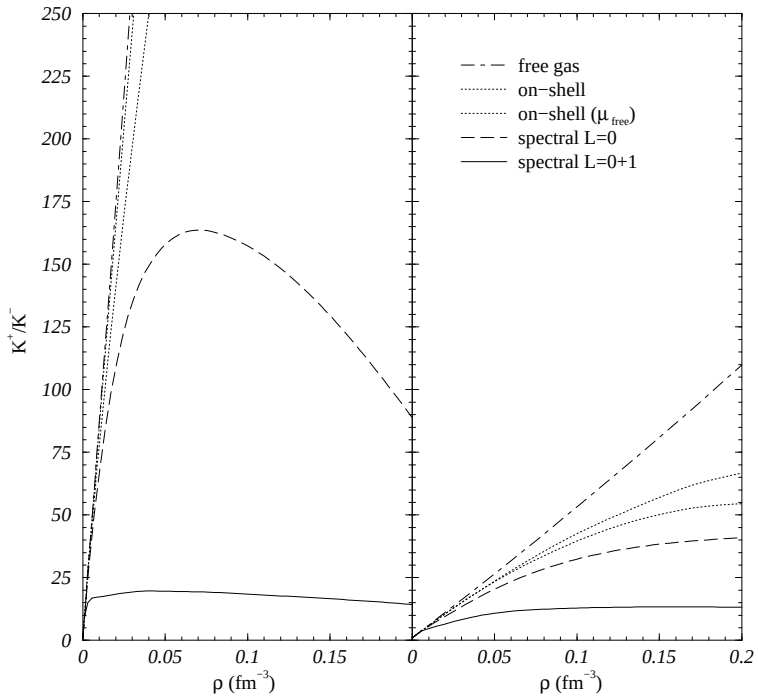

Figure 4.1: K^+/K^- ratio as a function of the density for $T = 50$ MeV (left panel) and $T = 80$ MeV (right panel) calculated in different approaches: the free Fermi gas (dot-dashed line), on-shell self-energies (dotted line), on-shell self-energies with μ from a free (non-interacting) Fermi gas (thin dotted line), dressing the K^- with its single particle spectral function, with the $L = 0$ contribution (long-dashed line) and taking into account the additional $L = 1$ partial wave (solid line).

4.4 Results for the K^-/K^+ ratio

In this section we discuss the effects of dressing the K^- mesons in hot and dense nuclear matter on the K^-/K^+ ratio around the value $K^-/K^+ = 0.031 \pm 0.005$ [Men00] found in Ni+Ni collisions at an energy of 1.93 AGeV. A preliminary study was already reported in Ref. [Tol01b]. As previously mentioned, we prefer to discuss the results for the inverted ratio $K^+/K^- \approx 30$.

The K^+/K^- ratio is shown in Fig. 4.1 as a function of density at two given temperatures, T= 50 and 80 MeV, calculated for the three ways of dressing the K^-: free

(dot-dashed lines), the on-shell or mean-field approximation of Eqs. (4.23) and (4.24) (dotted lines), and using the $\bar{K}$ spectral density including s-wave (long-dashed lines) or both s-wave and p-wave contributions (solid lines). The two chosen temperatures roughly delimit the range of temperatures which have been claimed to reproduce, in the framework of the thermal model, not only the K^+/K^- ratio but also all the other particle ratios involved in the Ni+Ni collisions at SIS energies [Cle98b, Cle99b].

Since the baryonic chemical potential μ_B grows with density, the factor $e^{\mu_B/T}$ in the partition functions of Eqs. (4.18), (4.20) allows one to understand why the ratio increases so strongly with density in the free gas approximation (dot-dashed lines). The same is true when the particles are dressed. In this case, however, the K^- feels an increasing attraction with density which tends to compensate the variation of μ_B and the curves bend down after the initial increase. This effect is particularly notorious when the full K^- spectral density is used. The results are in qualitative agreement with the "broad-band equilibration" notion introduced by Brown et al. [Bro01a, Bro01b], which was established, in the context of a mean-field picture, through a compensation between the increased attraction of the mean-field K^- potential as density grows with the increase in the baryon chemical potential μ_B. However, in this present model, the dotted lines in Fig. 4.1 show that the gain in binding energy in the on-shell approximation for K^- (thick dotted line in Fig. 4.1) when the density grows does not completely compensate the increase of μ_B, as was the case in Ref. [Bro01a, Bro01b]. To illustrate this fact we note that the variation of the K^- single particle energy at zero momentum at $T = 70$ MeV changes in our model from 434 MeV to 375 MeV when the density grows from $1.2\rho_0$ to $2.1\rho_0$, while μ_B changes from 873 MeV to 962 MeV. Therefore the relevant quantity to understand the behaviour of the K^+/K^- ratio with density in the on-shell approximation, i.e. the sum of μ_B and E_{K^-} (see Eq. (6) of

Ref. [Bro01a, Bro01b]), suffers in our model a variation of about 30 MeV. On the other hand, the model of Ref.[Bro01a, Bro01b] assumed a slower variation of μ_B, from 860 MeV to 905 MeV, which was almost cancelled by the change of E_{K^-} from 380 MeV to 332 MeV, giving therefore a practically density independent ratio.

The results displayed in Fig. 4.1 show that the "broad-band equilibration" only shows up clearly when the full spectral function is used (solid line in Fig. 4.1). After an increase at low densities, the K^+/K^- ratio remains constant at intermediate and high densities. The use of the spectral density implicitly amounts to an additional gain in binding energy for the antikaons and, as density increases, it compensates rather well the variation of μ_B.

To understand the origin of this additional effective attraction when the full spectral density is used, we show in Fig. 4.2 the two functions that contribute to the integral over the energy in the definition of the K^- partition function [Eq.(4.28)], namely the Boltzmann factor $e^{-\sqrt{s}/T}$ and the K^- spectral function including $L = 0$ (long-dashed line) and $L = 0 + 1$ (solid line) components of the $\bar{K}N$ interaction for a momentum $q = 500$ MeV at $\rho = 0.17$ fm^{-3} and T= 80 MeV. As it is clearly seen in the figure, the overlap of the Boltzmann factor with the quasi-particle peak of the K^- spectral function is small for this momentum. It is precisely the overlap with the strength in the low energy region that acts as a source of attraction in the contribution to the K^- partition function. This effect is particularly pronounced when the p-waves are included, due to the additional low-energy components in the spectral function coming from the coupling of the K^- meson to hyperon-hole (YN^{-1}) excitations, where Y stands for Λ, Σ and Σ^*. Assigning these low energy components to real antikaons in the medium is not clear, since one should interpret them as representing the production of hyperons through

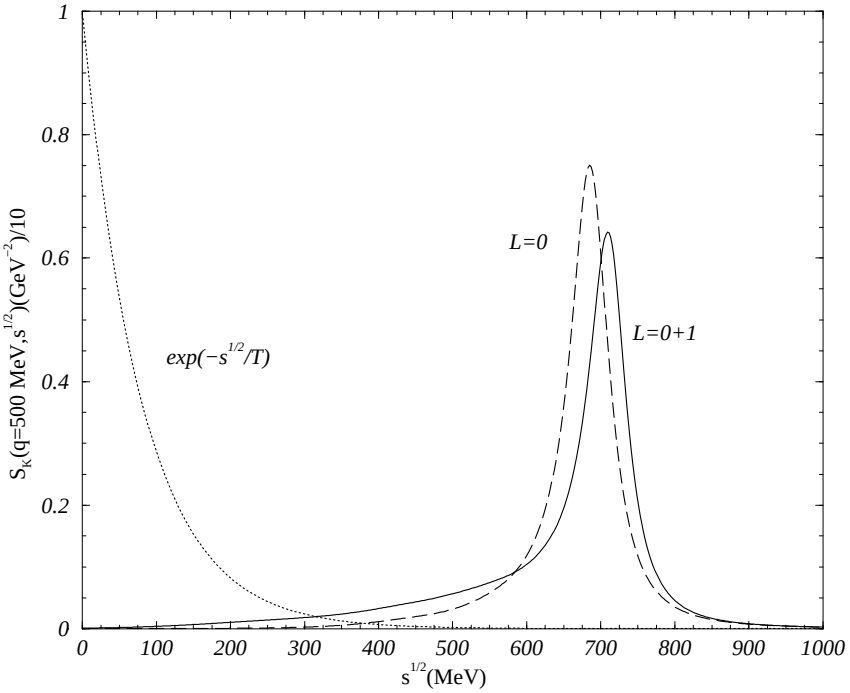

Figure 4.2: The Boltzmann factor (dotted line) and the K^- spectral function, including s-wave (long-dashed line) or s- and p-wave (solid line) components of the $\bar{K}N$ interaction, as functions of the energy, for a momentum $q = 500$ MeV at saturation density and temperature $T = 80$ MeV.

$\bar{K}N \to Y$ conversion. While this is certainly true, it may also happen that, once these additional hyperons are present in the system, they can subsequently interact with fast non-strange particles (pions, nucleons) to create new antikaons. A clean interpretation on what fraction of the low energy strength will emerge as antikaons at freeze-out is certainly an interesting question and its investigation will be left here for forthcoming work.

Once the integral over the energy is performed, the determination of the K^- partition function still requires an integral over the momentum. The integrand as a function of momentum is plotted in Fig. 4.3 for the same density and temperature than in the previous figure. As expected, the integrand is larger when the full spectral density

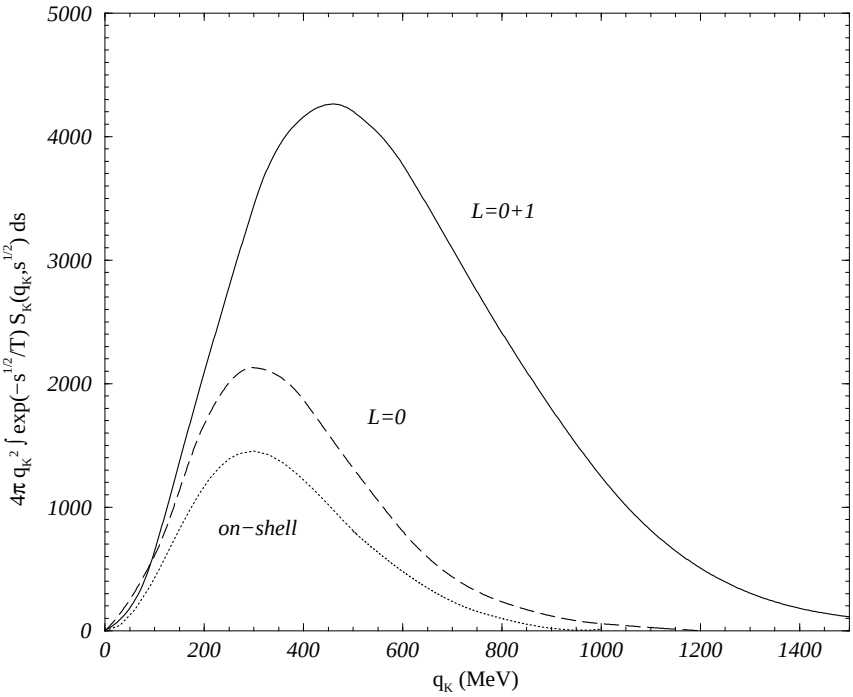

Figure 4.3: The integrand which defines the K^- partition function [Eq. (4.28)] as a function of momentum, at saturation density and $T = 80$ MeV, for different approaches: on-shell prescription (dotted line), using the K^- spectral function with the $L = 0$ components of the $\bar{K}N$ interaction (long-dashed line) and including also the $L = 1$ partial waves (solid line).

is considered. Therefore, the K^- partition function is enhanced making the K^+/K^- ratio smaller than in the on-shell approximation as well as in the case where only the $L = 0$ contributions to the spectral density are used. Notice the behaviour at large q, which decays very quickly in the on-shell approximation but has a long tail for the $L = 0 + 1$ spectral density originated from the coupling of the K^- meson to YN^{-1} configurations.

Another aspect that we want to consider is how the dressing of the Σ hyperon affects the value of the ratio. In Fig. 4.4 the value of the K^+/K^- ratio at $T = 50$ MeV is shown as a function of density for different situations. In all calculations displayed in the figure, the partition function associated to K^- has been obtained

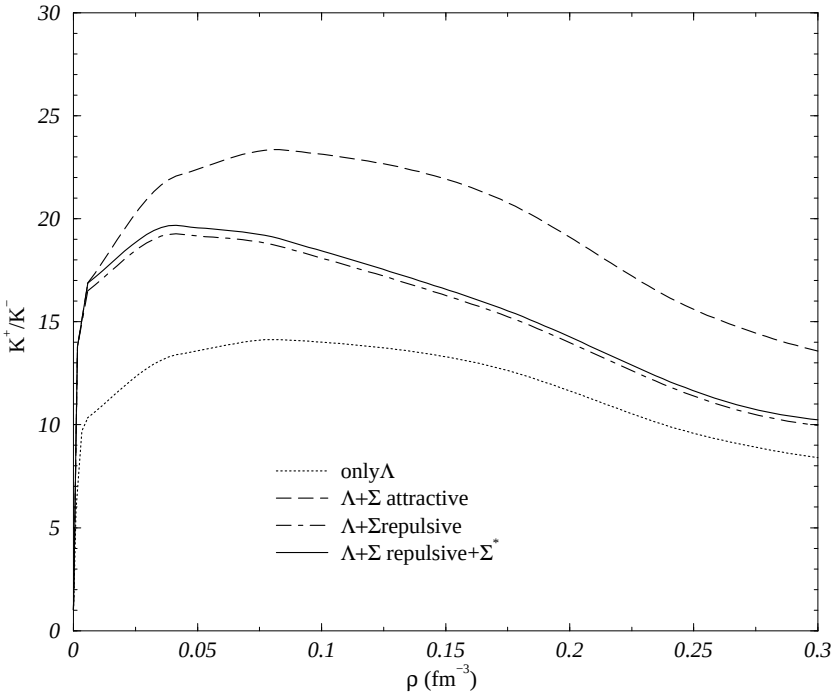

Figure 4.4: The K^+/K^- ratio as a function of density at T=50 MeV. The dotted line shows the results when only the Λ hyperons are considered in the determination of the ratio. The dashed (dot-dashed) line includes also the contribution of the Σ hyperon dressed with an attractive (repulsive) mean-field potential. The solid line includes the effect of the Σ^* resonance.

using the full K^- spectral density. The dotted line corresponds to the case where only the Λ hyperons, dressed with the attractive mean-field potential given in the previous section, are included to balance strangeness. When the Σ hyperon is incorporated with a moderately attractive potential of the type $U_\Sigma = -30\rho/\rho_0$ MeV, the K^+/K^- ratio is enhanced substantially (dashed line). This enhancement is more moderate when one uses the repulsive potential $U_\Sigma = +30\rho/\rho_0$ instead (dot-dashed line). Finally, the additional contribution of the Σ^* resonance produces only a small increase of the ratio (solid line) due to its higher mass. We have checked that heavier strange baryonic or mesonic resonances do not produce visible changes in our results. Notice also that, although the ratios obtained with both prescriptions for the mean-field potential of the

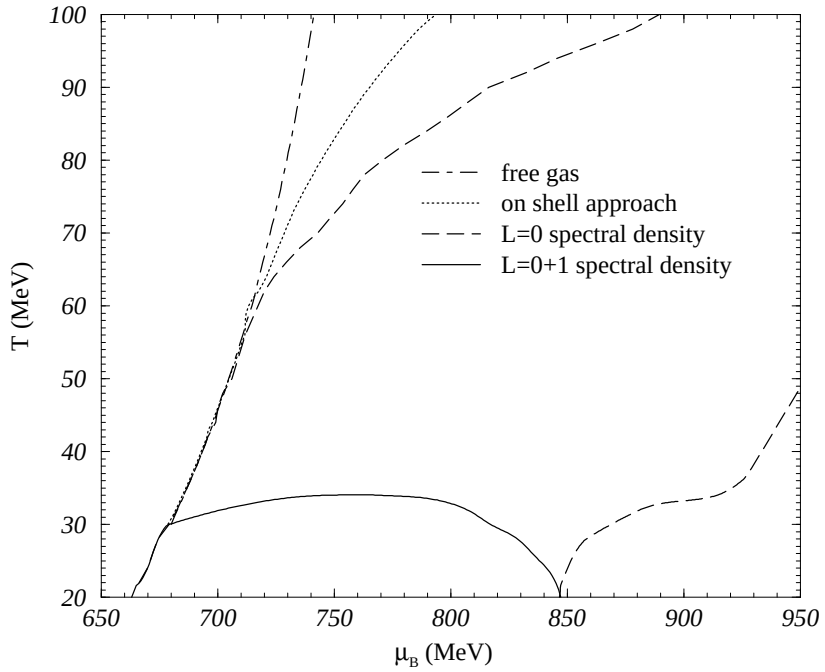

Figure 4.5: Relation between the temperature and the baryochemical potential of hadronic matter produced in heavy-ion collisions for fixed K^+/K^- ratio of 30, calculated within different approaches as discussed in the text.

Σ meson differ appreciably, the present uncertainties in the ratio would not permit to discriminate between them.

In the framework of the statistical model, one obtains a relation between the temperature and the chemical potential of the hadronic matter produced in the heavy-ion collisions by fixing the value of the K^-/K^+ ratio which was measured for Ni+Ni collisions at GSI to be on the average $K^-/K^+ = 0.031 \pm 0.005$ [Men00]. We compare our results with a corresponding inverse ratio of $K^+/K^- = 30$ in the following. The temperatures and chemical potentials compatible with that ratio are shown in Fig. 4.5 for different approaches. The dot-dashed line stands for a free gas of hadrons, similar to the calculations reported in Refs. [Cle98b, Cle99b]. The dotted line shows the $T(\mu)$ curve obtained with the on-shell or mean-field approximation [see Eqs.(4.23) and

(4.24)], while the dashed and solid lines correspond to the inclusion of the off-shell properties of the K^- self-energy by using its spectral density [Eqs. (4.25),(4.26) and (4.28)], including $L = 0$ or $L = 0 + 1$ components, respectively.

In the free gas limit, the temperatures compatible with a ratio $K^+/K^- = 30$ imply a narrow range of values for the baryonic chemical potentials, namely $\mu_B \in [665, 740]$ MeV for temperatures in the range of 20 to 100 MeV. These values translate into density ranges of $\rho \in [6 \times 10^{-7}\rho_0, 0.9\rho_0]$.

As it can be seen from the dotted line in Fig. 4.5, the attractive mean-field potential of the antikaons compensates the effect of increasing baryochemical potential μ_B. As a consequence, the density at which the freeze-out temperature compatible with the measured ratio takes place also grows. But this attraction is not enough to get the same K^+/K^- ratio for a substantially broader range of density compared to the free case. So we do not see a clear indication of "broad-band equilibration" in our self-consistent mean-field calculation in contrast to the results of Brown, Rho, and Song [Bro01a, Bro01b].

The influence of the antikaon dressing on the ratio is much more evident when the spectral density is employed (dashed and solid lines). From the preceding discussions, it is easy to understand that the low energy behaviour of the spectral density enhances the K^- contribution to the ratio, having a similar role as an attractive potential and, hence, the value of μ_B compatible with a ratio at a given temperature increases. Moreover, due to the bending of the K^+/K^- ratio with density and its evolution with temperature observed in Fig. 4.1, it is clear that there will be a maximum value of T compatible with a given value of the ratio. Below this maximum temperature, there will be two densities or, equivalently, two chemical potentials compatible with the ratio. For example, the

ratio K^+/K^-=30 will in fact not be realized neither with $T = 80$ MeV nor $T = 50$ MeV, the two temperatures displayed in Fig. 4.1, if the antikaon is dressed with the spectral density containing $L = 0$ and $L = 1$ components. As shown in Fig. 4.5, only temperatures lower than 34 MeV are compatible with ratio values of 30!

We note that the flat regions depicted by the solid lines in Fig. 4.5 could be considered to be in correspondence with the notion of "broad-band equilibration" of Brown et al. [Bro01a, Bro01b], in the sense that a narrow range of temperatures and a wide range of densities are compatible with a particular value of the K^+/K^- ratio. Nevertheless, the temperature range is too low to be compatible with the measured one. Explicitly, for K^+/K^-=30, we observe a nearly constant ratio in the range of $30 - 34$ MeV covering a range of chemical potentials in between $680 - 815$ MeV which translates into a density range $\rho \in [1.5 \times 10^{-4}\rho_0, 0.02\rho_0]$. Note that in this case, we can hardly speak of a broad-band equilibration in the sense of that introduced by Brown, Rho and Song in Ref. [Bro01a, Bro01b], where a ratio K^+/K^-=30 holds over a large range of densities in between $\frac{1}{4}\rho_0$ and $2\rho_0$ for $T = 70$ MeV. However, as we indicated at the beginning of this section, this result was obtained in the framework of a mean-field model and our equivalent on-shell results (dotted lines in Figs. 4.1, 4.5), based on a stronger variation of the μ_B with density and on a less attractive $U_{\bar{K}}$, seem to be very far from producing the broad-band equilibration behaviour.

As pointed out before, our nucleon chemical potential is obtained in the framework of a relativistic model and varies with density more strongly than that used in Ref. [Bro01a, Bro01b], which shows values close to those for a free Fermi gas. If we now calculate the K^+/K^- ratio using a $\mu_B(\rho, T)$ for a free (non-interacting) system in the on-shell approximation, we obtain the thin dotted line in Fig. 4.1. At $T = 80$

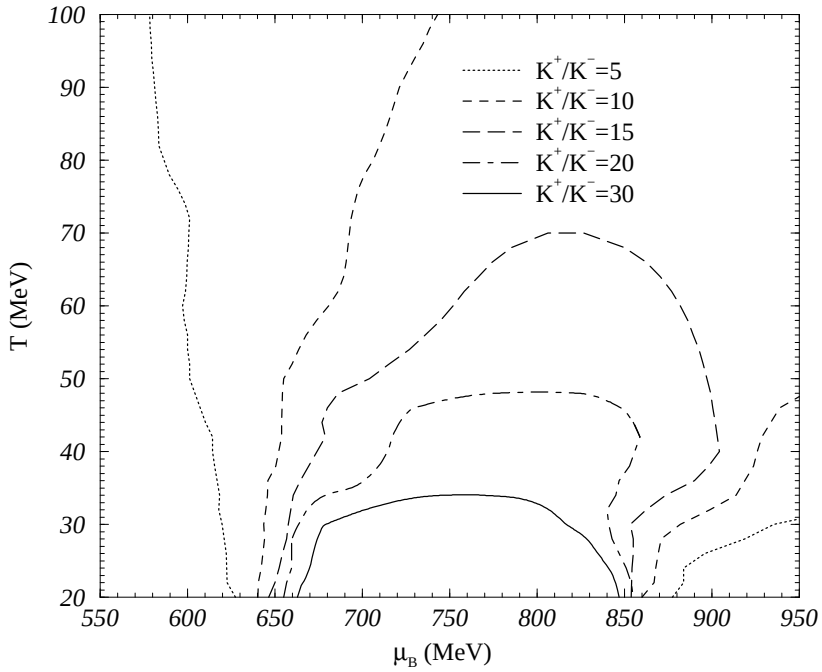

Figure 4.6: The K^+/K^- ratio plotted for the full spectral density of the K^- as a contour plot for different temperatures and baryochemical potentials.

MeV, we now observe a tendency of a broad-band equilibration but for ratios higher than 30, of around 50. This is connected to the particular on-shell potential of the antikaon which, in our self-consistent procedure, turns to be moderately attractive. Only if the attraction was larger would the broad band be realized in this on-shell picture for smaller values of the ratio as found by Brown et al. [Bro01a, Bro01b].

Fig. 4.6 shows the K^+/K^- ratio for the full model calculation as a contour plot for different temperatures and baryochemical potentials. We note, that the ratio is substantially lower at the temperature and density range of interest, being more likely around 15 or so for a moderately large region of baryochemical potential. Note that this reduced ratio translates into an overall enhanced production of K^- by a factor of two compared to the experimentally measured value. At pion freeze-out, the medium

can hold twice as many K^- as needed to explain the measured enhanced production of K^- if one considers the full spectral features of the K^- in the medium. We stress again that this enhancement is not due to an increased attraction in the sense of a mean-field calculation. It is a consequence of the additional strength of the spectral function at low energies which emerges when taking into account p-wave hyperon-hole excitations. The Boltzmann factor amplifies the contribution of the low-energy region of the spectral function so that these excitations are becoming the main reason for the overall enhanced production of the K^- in the medium. However, in order to determine the real number of antikaons that will emerge at freeze-out, it is necessary to use sophisticated dynamical models, and this is precisely one of our future research lines.

Conclusions

The purpose of this thesis has been to study the properties of the $\bar{K}$ meson in hot and dense matter, within the framework of a coupled-channel self-consistent calculation based on a meson-exchange potential, and to investigate the possible implications on the K^-/K^+ ratio in heavy-ion collisions at GSI energies.

The bare meson-baryon interaction of the Jülich group [Mul90] is the starting-point of our calculations. The scattering theory for the $\bar{K}N$ interaction performed by solving numerically the Bethe-Salpeter equation for the Jülich meson-exchange potential has been presented in Chapter 1. Although the experimental values for the s-wave $\bar{K}N$ scattering amplitude in the $I = 1$ sector and some other branching ratios differ significantly from the calculated ones, the experimental K^-p cross-sections at energies around the K^-p threshold are well-reproduced. In addition, the s-wave $\Lambda(1405)$ resonance, that governs the behavior of the $\bar{K}N$ interaction, is generated dynamically. In the $L = 1$ channel, the Jülich $\bar{K}N$ interaction contains the contribution of the Λ and Σ pole diagrams but the $\Sigma^*(1385)$ is omitted. However, in some of the results pre-

sented in this thesis, the effect of the $\Sigma^*(1385)$ has been included through the explicit coupling of the antikaons to the Σ^*-hole configurations. Clearly, a more accurate $\bar{K}N$ bare interaction in all partial waves is needed, which, nevertheless, goes beyond the scope of this thesis.

In Chapter 2 we have performed a microscopic self-consistent calculation of the single-particle potential of a $\bar{K}$ meson embedded in symmetric nuclear matter reviewing the basic ideas of the BHF theory. The conclusions of this chapter are the following:

- Due to the strong energy dependence of the $\bar{K}N$ G-matrix it becomes crucial to follow a self-consistent procedure to evaluate the $\bar{K}$ self-energy. We have analyzed two self-consistent schemes which produce substantial different results. When only the real part of the $\bar{K}$ optical potential is retained in the self-consistent procedure, one obtains an attraction of about -100 MeV at zero momentum and a very small imaginary part of around -3 MeV. This optical potential would lead to extremely narrow deeply bound kaonic states in nuclei. However, when the complete complex optical potential is self-consistently determined, the real part becomes 15% less attractive and the imaginary part increases to around -25 MeV, as a consequence of the opening of new decay channels which widens the antikaon strength producing a $\bar{K}N$ amplitude smoother and more spread out over energies.

- We have obtained the kaon optical potential as a function of the $\bar{K}$ momentum, up to regions that are relevant in the analysis of heavy-ion collisions where antikaons are created with a finite momentum. Our results for the optical potential show a momentum dependence which is moderate for the real part and significantly more relevant for the imaginary part, which is especially important for densities

around the saturation density.

- We have also studied the effect of including higher partial waves of the $\bar{K}N$ interaction than $L = 0$. Some influence is already seen at zero $\bar{K}$ momentum but the largest effects appear clearly at large momenta, where the inclusion of the $L > 0$ partial waves of the $\bar{K}N$ interaction can practically double the size of the optical potential. At a $\bar{K}$ momentum of 500 MeV/c the complex optical potential changes from the $L = 0$ value of $(-28, -39)$ MeV to $(-52, -61)$ MeV when all partial waves are included.

- The inclusion of the pion dressing in the intermediate πY states changes substantially the results for the $\bar{K}$ optical potential. When pions are dressed, the $\bar{K}$ optical potential becomes less attractive and the imaginary part loses structure significantly. At zero antikaon momentum, the optical potential varies from $(-84, -24)$ MeV to $(-62, -62)$ MeV when pions are dressed.

In Chapter 3 we have studied the $\bar{K}N$ interaction in hot and dense matter by extending to finite T our previous $T = 0$ model. We conclude that

- Although more moderate than in the $T = 0$ case, we have also found at finite temperature that dressing the pions has a strong influence on the $\bar{K}N$ amplitudes and, consequently, on the $\bar{K}$ optical potential.

- Partial waves higher than the $L = 0$ component of the $\bar{K}N$ effective interaction also contribute significantly to the antikaon optical potential at finite temperature. The real part gains attraction and the imaginary part becomes more absorptive. As in the $T = 0$ case, at a momentum of 500 MeV/c, the contribution of the $L > 0$ components is as large as that of the $L = 0$ one.

- We have found that self-consistency effects have a tremendous influence on the behavior of the antikaon optical potential with temperature. At normal saturation density, the antikaon optical potential stays attractive, of the order of -50 MeV, for temperatures as large as 70 MeV. If only Pauli blocking medium effects were considered, the temperature dependence of the antikaon optical potential would be much more important still remaining attractive for the temperatures studied. Other interaction models including only Pauli blocking effects even give a repulsive optical potential at these high temperatures.

- In general, temperature effects smear out the different observables with respect to the $T = 0$ case. For instance, the antikaon spectral function at finite temperature shows much less structure than that at $T = 0$, reducing its shape basically to a single peak located at the quasiparticle energy.

- The attractive potential found here for finite density, finite temperature and finite momentum is especially interesting to understand the enhanced K^-/K^+ ratio measured by the KaoS collaboration at GSI, together with other mechanisms that have been already suggested in the literature, such as an enhanced production of K^- through πY collisions.

Finally, we have studied in Chapter 4, within the framework of thermal models, the influence of the properties of the $\bar{K}$ meson in hot and dense matter on the K^-/K^+ ratio in heavy-ion collisions at SIS/GSI. We have considered the effects of the previously obtained antikaon self-energy for the s-wave adding the p-wave components from the Y-hole excitations, with $Y = \Lambda, \Sigma, \Sigma^*$. The main conclusions are summarized as follows:

- It is found that the determination of the temperature and chemical potential

at freeze-out conditions compatible with the ratio K^-/K^+ is very delicate and depends very strongly on the approximation adopted for the antikaon self-energy. For instance, compared to what is obtained for a non-interacting hadronic gas, the effect of dressing the K^- with an spectral function including both s- and p-wave components of the $\bar{K}N$ interaction lowers considerably the region of temperature to values around 35 MeV and increases the value of the chemical potential up to 850 MeV, compatible with the experimental value of the $K^+/K^- \approx 30$.

- When the free or on-shell properties of the antikaon are considered, the ratio at a given temperature shows a strong dependence with the density. This is in contrast with the "broad-band equilibration" advocated in the literature, which was established, in the context of a mean-field picture, through a compensation between the increased attraction of the mean-field $\bar{K}$ potential as density grows with the increase in the baryon chemical potential. Our mean-field properties do not achieve such a compensation due to a stronger increase of the nucleon chemical potential with density.

- When taking into account the full features of the spectral function of the K^-, we find that the K^-/K^+ ratio exhibits "broad-band equilibration". Nevertheless, the ratio is even in excess of the measured ratio at experimental temperatures. One can argue in principle, that dynamical non-equilibrium effects can reduce the number of K^- by virtue of annihilation with nucleons to hyperons and pions at freeze-out. What needs to be clarified is how the particles get on-shell at freeze-out, a question previously posed e.g. for antiproton and antihyperon production at the GSI and which should be addressed in dynamical models.

Appendix A: Pauli blocking

In this appendix we show how to compute the angular average of the Pauli operator, $Q_{\bar{K}N}(\vec{k},\vec{P})$. Defining $\vec{P}$ and $\vec{k}$ as the total and relative momenta of the $\bar{K}N$ pair, respectively

$$\vec{P} = \vec{k}_{\bar{K}} + \vec{k}_N, \qquad \vec{k} = \frac{m_N \vec{k}_{\bar{K}} - m_{\bar{K}} \vec{k}_N}{m_{\bar{K}} + m_N} \ , \tag{A.1}$$

we can rewrite the nucleon and antikaon momenta in the laboratory system, $\vec{k}_N$ and $\vec{k}_{\bar{K}}$, as

$$\vec{k}_N = -\vec{k} + \frac{\xi}{1+\xi}\vec{P}, \qquad \vec{k}_{\bar{K}} = \vec{k} + \frac{1}{1+\xi}\vec{P} \ , \tag{A.2}$$

where a galilean transformation has been used and $\xi = \dfrac{m_N}{m_{\bar{K}}}$.

The Pauli operator acts only on the nucleonic line and, in symmetric nuclear matter, it reads

$$Q_{\bar{K}N}(\vec{k},\vec{P}) = \theta\left(\left|\frac{\xi}{1+\xi}\vec{P} - \vec{k}\right| - k_F\right) \ , \tag{A.3}$$

which depends on the angle between $\vec{P}$ and $\vec{k}$. In order to eliminate this dependence, we introduce an angle average

$$\overline{Q}_{\bar{K}N}(k,P) = \frac{1}{2}\int_0^{\pi} d\theta \sin\theta\, Q(\vec{k},\vec{P}) \ . \tag{A.4}$$

The Pauli blocking factor is only different from zero in the case where

$$\left|\frac{\xi}{1+\xi}\vec{P} - \vec{k}\right| > k_F \ . \tag{A.5}$$

Therefore, we can define two regions depending if $\xi/(1+\xi)\ P > k_F$ (A region) or $\xi/(1+\xi)\ P < k_F$ (B region). The magnitude of $\vec{k}$ determines the value of the Pauli blocking factor afterwards.

For the A region, the Pauli blocking will give

$$\overline{Q}^{A}_{\bar{K}N}(k,P) = \begin{cases} \frac{1}{2}\left[1 + \dfrac{k^2 + \left(\frac{\xi}{1+\xi}\right)^2 P^2 - {k_F}^2}{2kP\frac{\xi}{1+\xi}}\right] & \text{for } \frac{\xi}{1+\xi}P - k_F < k < \frac{\xi}{1+\xi}P + k_F, \\ 1 & \text{for } k > \frac{\xi}{1+\xi}P + k_F \text{ or } k < \frac{\xi}{1+\xi}P - k_F, \\ 0 & \text{otherwise} \end{cases} , \tag{A.6}$$

while for the B region

$$\overline{Q}^{B}_{\bar{K}N}(k,P) = \begin{cases} \frac{1}{2}\left[1 + \dfrac{k^2 + \left(\frac{\xi}{1+\xi}\right)^2 P^2 - {k_F}^2}{2kP\frac{\xi}{1+\xi}}\right] & \text{for } k_F - \frac{\xi}{1+\xi}P < k < \frac{\xi}{1+\xi}P + k_F, \\ 1 & \text{for } k > \frac{\xi}{1+\xi}P + k_F \ , \\ 0 & \text{otherwise} \end{cases} , \tag{A.7}$$

Then, the resulting function is given by

$$\overline{Q}_{\bar{K}N}(k,P) = \begin{cases} \frac{1}{2}\left[1 + \dfrac{k^2 + \left(\frac{\xi}{1+\xi}\right)^2 P^2 - {k_F}^2}{2kP\frac{\xi}{1+\xi}}\right] & \text{for } \mid \frac{\xi}{1+\xi}P - k_F \mid < k < \frac{\xi}{1+\xi}P + k_F, \\ 1 & \text{for } k > \frac{\xi}{1+\xi}P + k_F \text{ or } k < \frac{\xi}{1+\xi}P - k_F, \\ 0 & \text{otherwise} \end{cases} , \tag{A.8}$$

which depends only on the modulus of the relative and total momenta of the $\bar{K}N$ state.

Appendix B: $\bar{K}$ single-particle potential

The single-particle potential of the $\bar{K}$ meson embedded in symmetric nuclear matter is given by

$$U_{\bar{K}}(k_{\bar{K}}, E^{qp}_{\bar{K}}) = \sum_{N \leq F} \langle \bar{K}N \mid G_{\bar{K}N \to \bar{K}N}(\Omega = E^{qp}_N + E^{qp}_{\bar{K}}) \mid \bar{K}N \rangle \ , \tag{B.1}$$

where the sum runs over the nucleon Fermi sea. More precisely, displaying the dependence on the particle momentum, spin and isospin and omitting the energy dependence

$$U_{\tau_{\bar{K}}}(\vec{k}_{\bar{K}}) = \sum_{\vec{k}_N \sigma_N \tau_N} \theta(k_F - |\vec{k}_N|) \ \langle \vec{k}_{\bar{K}} \tau_{\bar{K}}; \vec{k}_N \sigma_N \tau_N \mid G \mid \vec{k}_{\bar{K}} \tau_{\bar{K}}; \vec{k}_N \sigma_N \tau_N \rangle \ . \tag{B.2}$$

In order to express $U_{\tau_{\bar{K}}}(\vec{k}_{\bar{K}})$ in the partial wave basis, we should first use the expressions

for $\vec{k}_N$ and $\vec{k}_{\bar{K}}$ of Appendix A and rewrite them in terms of the total $\vec{P}$ and the relative momenta $\vec{k}$ of the $\bar{K}N$ system. The next step is to transform the physical basis into the partial wave one introducing the coupled isospin basis and the partial wave decomposition of a plane wave [see Eqs. (1.18) and (1.19)] to finally couple to the total angular momentum J. As a final product we get

$$\begin{aligned} U_{\tau_{\bar{K}}}(\vec{k}_{\bar{K}}) = & \sum_{\vec{k}_N \sigma_N \tau_N} \theta(k_F - |\vec{k}_N|) \sum_{\substack{LM_L L'M'_L \\ IM_I I'M'_I \\ JMJ'M'}} Y^*_{LM_L}(\widehat{k})\; Y_{L'M'_L}(\widehat{k}) \\ & \times \langle IM_I | t_{\bar{K}} \tau_{\bar{K}} t_N \tau_N \rangle \langle I'M'_I | t_{\bar{K}} \tau_{\bar{K}} t_N \tau_N \rangle \langle JM | LM_L \tfrac{1}{2} \sigma_N \rangle \; \langle J'M' | L'M'_L \tfrac{1}{2} \sigma_N \rangle \\ & \times \langle \vec{P}\,' k L' \tfrac{1}{2} J'M' I'M'_I | G | \vec{P} k L \tfrac{1}{2} JMIM_I \rangle \; , \end{aligned} \tag{B.3}$$

where we have used the fact that the total spin is $S = 1/2$ and its third component $M_S = \sigma_N$. The G-matrix element can be rewritten as

$$G \to \delta_{JJ'} \delta_{MM'} \delta_{II'} \delta_{M_I M'_I} \delta_{LL'} \delta_{\vec{P}\vec{P}\,'} \langle \vec{P}\; k | G^{L \frac{1}{2} JIM_I} | \vec{P}\; k \rangle \; . \tag{B.4}$$

We note that G doesn't depend on M because of space isotropy. Therefore, Eq. (B.3) can be simplified

$$\begin{aligned} U_{\tau_{\bar{K}}}(\vec{k}_{\bar{K}}) = & \sum_{\vec{k}_N \sigma_N \tau_N} \theta(k_F - |\vec{k}_N|) \sum_{\substack{LM_L L'M'_L \\ IM_I JM}} Y^*_{LM_L}(\widehat{k})\; Y_{L'M'_L}(\widehat{k}) |\langle IM_I | t_{\bar{K}} \tau_{\bar{K}} t_N \tau_N \rangle|^2 \\ & \times \langle JM | LM_L \tfrac{1}{2} \sigma_N \rangle \; \langle JM | L'M'_L \tfrac{1}{2} \sigma_N \rangle \; \delta_{LL'} \; \langle \vec{P}\; k | G^{L \frac{1}{2} JIM_I} | \vec{P}\; k \rangle \; . \end{aligned} \tag{B.5}$$

Using the following property of the Clebsch-Gordan

$$\langle j_1 m_1 j_2 m_2 | j m \rangle = (-1)^{j_1 - j + m_2} \sqrt{\frac{2j+1}{2j_1+1}} \langle j \; m \; j_2 - m_2 | j_1 \; m_1 \rangle \; , \tag{B.6}$$

we can perform the summation over M and σ_N together with M_I and τ_N

$$\sum_{M\sigma_N} \langle JM|LM_L\tfrac{1}{2}\sigma_N\rangle \ \langle JM|L'M'_L\tfrac{1}{2}\sigma_N\rangle = \frac{2J+1}{2L+1}\ \delta_{LL'}\ \delta_{M_L M'_L}\ ,$$
$$\sum_{M_I\tau_N} |\langle IM_I|t_{\bar{K}}\tau_{\bar{K}}t_N\tau_N\rangle|^2 = \frac{2I+1}{2t_{\bar{K}}+1}\ , \tag{B.7}$$

where we have used the independence on M_I of the G-matrix for symmetric nuclear matter. Moreover,

$$\sum_{M_L} Y^*_{LM_L}(\widehat{k})Y_{LM_L}(\widehat{k}) = \frac{2L+1}{4\pi}\ . \tag{B.8}$$

Therefore, the final expression for $U_{\tau_{\bar{K}}}(k_{\bar{K}})$ reads

$$U_{\tau_{\bar{K}}}(\vec{k}_{\bar{K}}) = \frac{1}{4\pi}\sum_{\vec{k}_N}\theta(k_F - |\vec{k}_N|)\ \sum_{LJI}\frac{(2J+1)(2I+1)}{2t_{\bar{K}}+1}\ \langle\vec{P}\ k|G^{L\frac{1}{2}JI}|\vec{P}\ k\rangle\ . \tag{B.9}$$

In order to perform the sum over $\vec{k}_N$ one should transform it into an integral over $\vec{k}$

$$\sum_{\vec{k}_N} \to \int d^3k_N \to \int (1+\xi)^3 d^3k\ . \tag{B.10}$$

with $\xi = m_N/m_{\bar{K}}$.

At this point one approximation is done. We will perform an angular average over the G-matrix in such way that it will depend on an average center-of-mass momentum, $\overline{P^2}$, and average hole one, $\overline{k_N^2}$. This last dependence comes through the energy dependence of the G-matrix. These averaged quantitities are calculated according to the limit of integration $|\vec{k}_N| < k_F$ [see Appendix C, D for more details]. The final

expression for $U_{\bar{K}}(\vec{k}_{\bar{K}})$, including all dependences, reads

$$U_{\bar{K}}(k_{\bar{K}}, E^{qp}_{\bar{K}}(k_{\bar{K}})) = \frac{1}{2}\sum_{LJI}(2J+1)(2I+1)(1+\xi)^3 \int_0^{k_{max}} k^2\ dk\ f(k,k_{\bar{K}}) \times\langle(\bar{K}N);k|G^{LJI}(\overline{P^2}, E^{qp}_{\bar{K}}(k_{\bar{K}}) + E^{qp}_{N}(\overline{k^2_N}))|(\bar{K}N);k\rangle\ , \quad \text{(B.11)}$$

where $t_{\bar{K}} = 1/2$ and $\vec{k}_{\bar{K}} \to k_{\bar{K}}$. The angular integral has been performed with the aid of the weight function $f(k, k_{\vec{K}})$ defined in Appendix C.

Appendix C: Angular integration

In the construction of the $\bar{K}$ single-particle potential of Appendix C, the integral over $\cos\theta$ has been replaced by a weight function that reads

$$f(k, k_{\bar{K}}) = \frac{1}{2}\int_{-1}^{1} d(\cos\theta)\ f(\vec{k}, \vec{k}_{\bar{K}}, \theta)\ , \tag{C.1}$$

after having introduced an average center-of-mass and average hole momenta on the calculation of the G-matrix. The integration is restricted to a certain range of angles according to whether the nucleon is inside or outside the Fermi sphere. In this appendix we show the regions of integration compatible with this previous condition, together with the corresponding value of the weight function. Moreover, the values of the average center-of-mass and average hole momenta also depend on the region studied. This calculation will be performed in Appendix D.

As it can be seen in Fig. C.1, two regions of integration are defined, $\xi k_{\bar{K}} < k_F$ or

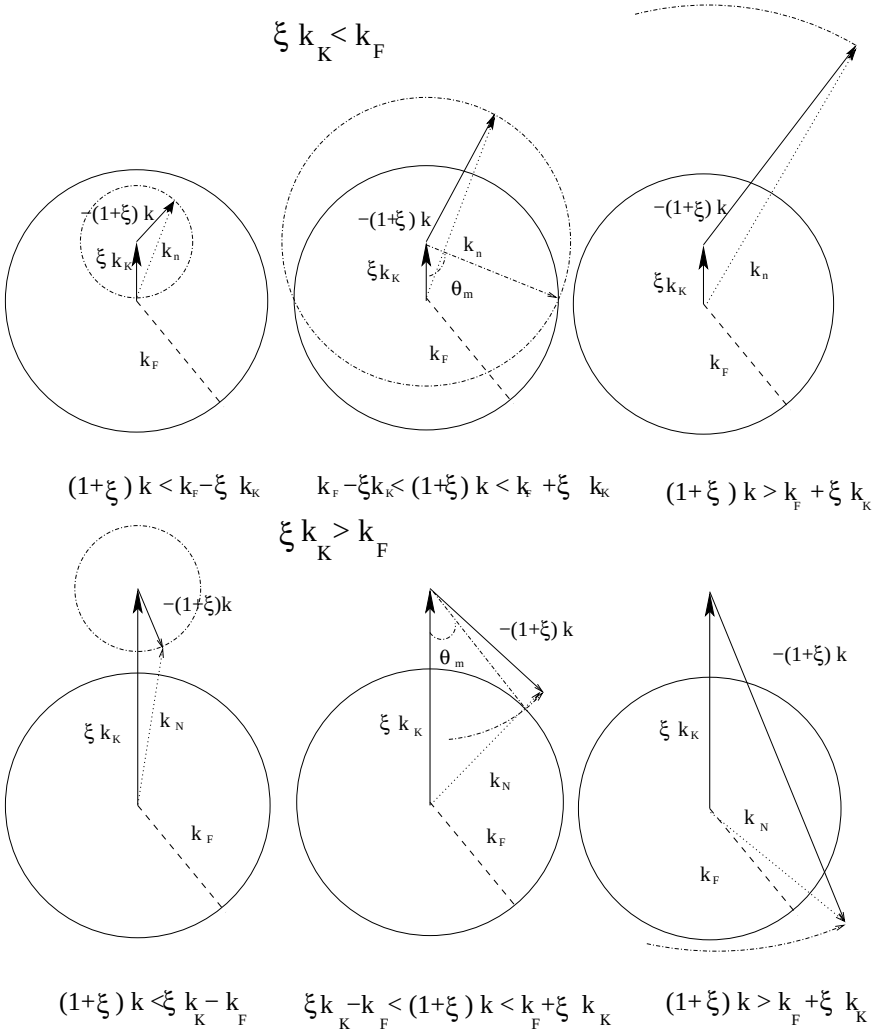

Figure C.1: Regions determined by $|\vec{k}_N| \leq k_F$, discussed in the text.

$\xi k_{\bar{K}} > k_F$, with $\xi = m_N/m_{\bar{K}}$ and k_F the Fermi momentum.

Case 1: $\xi k_{\bar{K}} < k_F$

- $(1+\xi)k < k_F - \xi k_{\bar{K}}$: k_N always lies inside the Fermi sphere and therefore, all angles are possible, i.e., $f(k, k_{\bar{K}}) = 1$

- $(1+\xi)k > k_F + \xi k_{\bar{K}}$: k_N always lies outside the Fermi sphere and therefore, no

angles are possible, i.e., $f(k, k_{\bar{K}}) = 0$

- $k_F - \xi k_{\bar{K}} < (1+\xi)k < k_F + \xi k_{\bar{K}}$: k_N can lie inside or outside the Fermi sphere. The integration runs from a minimum $\cos(\theta_m)$ [see Fig. C.1]

$$\cos\theta_m = \frac{(\xi k_{\bar{K}})^2 + (1+\xi)^2 k^2 - k_F^2}{2\xi k_{\bar{K}}(1+\xi)k}$$

to 1, with the result

$$f(k, k_{\bar{K}}) = \frac{{k_F}^2 - [\xi k_{\bar{K}} - (1+\xi)k]^2}{4\xi(1+\xi)k_{\bar{K}}k} \ .$$

Case 2: $\xi k_{\bar{K}} > k_F$

- $(1+\xi)k < \xi k_{\bar{K}} - k_F$: k_N always lies outside the Fermi sphere and therefore, no angles are possible, i.e., $f(k, k_{\bar{K}}) = 0$

- $(1+\xi)k > k_F + \xi k_{\bar{K}}$: k_N always lies outside the Fermi sphere and therefore, no angles are possible, i.e., $f(k, k_{\bar{K}}) = 0$

- $\xi k_{\bar{K}} - k_F < (1+\xi)k < k_F + \xi k_{\bar{K}}$: k_N can lie inside or outside the Fermi sphere. The integration runs from a minimum $\cos(\theta_m)$ [see Fig. C.1]

$$\cos\theta_m = \frac{(\xi k_{\bar{K}})^2 + (1+\xi)^2 k^2 - k_F^2}{2\xi k_{\bar{K}}(1+\xi)k} \ ,$$

to 1, with the result

$$f(k, k_{\bar{K}}) = \frac{{k_F}^2 - [\xi k_{\bar{K}} - (1+\xi)k]^2}{4\xi(1+\xi)k_{\bar{K}}k} \ .$$

Therefore, the final expression for the weight function is

$$f(k,k_{\bar{K}}) = \begin{cases} 1 & \text{for } k \leq \frac{k_F - \xi k_{\bar{K}}}{1+\xi}, \\ 0 & \text{for } |\xi k_{\bar{K}} - (1+\xi)k| > k_F, \\ \dfrac{{k_F}^2 - [\xi k_{\bar{K}} - (1+\xi)k]^2}{4\xi(1+\xi)k_{\bar{K}}k} & \text{otherwise,} \end{cases} \tag{C.2}$$

which implicitly defines a maximum $k_{max} = \frac{k_F + \xi k_{\bar{K}}}{1+\xi}$ in the integral over k.

Appendix D: C.M. and hole momenta angular average

In this appendix we show how to compute an appropiate average of the $\bar{K}N$ center-of-mass momentum, $\vec{P}$, and the nucleon momentum, $\vec{k}_N$, given an external antikaon momentum, $\vec{k_{\bar{K}}}$, and a relative $\bar{K}N$ momentum, $\vec{k}$, used as integration variable in Eq. (2.23). From Eqs. (A.1) and (A.2) one obtains

$$\vec{P} = (1+\xi)(\vec{k}_{\bar{K}} - \vec{k}), \quad \vec{k}_N = \xi\vec{k}_{\bar{K}} - (1+\xi)\vec{k}\ . \tag{D.1}$$

The angle average of the center-of-mass momentum is defined as

$$\overline{P^2}(k_{\bar{K}}, k) \;=\; \frac{\displaystyle\int d(\cos\theta)\, P^2(k_{\bar{K}}, k, \cos\theta)}{\displaystyle\int d(\cos\theta)}, \tag{D.2}$$

where $P^2(k_{\bar{K}}, k, \cos\theta) = (1+\xi)^2(k_{\bar{K}}^2 + k^2 - 2k_{\bar{K}}k\cos\theta)$, with θ being the angle between $\vec{k}_{\bar{K}}$ and $\vec{k}$. Similarly, for $\overline{k_N^2}$ we have

$$\overline{k_N^2}(k_{\bar{K}}, k) = \frac{\int d(\cos\theta)\, k_N^2(k_{\bar{K}}, k, \cos\theta)}{\int d(\cos\theta)}, \tag{D.3}$$

where $k_N^2(k_{\bar{K}}, k, \cos\theta) = \xi^2 k_{\bar{K}}^2 + (1+\xi)^2 k^2 - 2\xi(1+\xi)k_{\bar{K}}k\cos\theta$.

In both cases, the integration runs from $\cos\theta_m$ to 1, where the expression for $\cos\theta_m$ depends on two regions of integration, according to the restrictions imposed by Pauli blocking [see Fig. C.1], and is given by

$$\cos\theta_m = \begin{cases} \dfrac{\xi^2 k_{\bar{K}}^2 + (1+\xi)^2 k^2 - k_F^2}{2\xi k_{\bar{K}}(1+\xi)k} & \text{for } \frac{|k_F - \xi k_{\bar{K}}|}{1+\xi} \le k \le \frac{k_F + \xi k_{\bar{K}}}{1+\xi}, \\ -1 & \text{for } k \le \frac{k_F - \xi k_{\bar{K}}}{1+\xi} \end{cases} \tag{D.4}$$

The resulting angle averages for $\vec{P}$ and $\vec{k}_N$ are given by

$$\overline{P^2}(k_{\bar{K}}, k) = \begin{cases} (1+\xi)^2 \left[(k_{\bar{K}}^2 + k^2) - \dfrac{[\xi k_{\bar{K}} + (1+\xi)k]^2 - k_F^2}{2\xi(1+\xi)} \right] & \text{for } \frac{|k_F - \xi k_{\bar{K}}|}{1+\xi} \le k \le \frac{k_F + \xi k_{\bar{K}}}{1+\xi}, \\ (1+\xi)^2(k_{\bar{K}}^2 + k^2) & \text{for } k \le \frac{k_F - \xi k_{\bar{K}}}{1+\xi} \end{cases} \tag{D.5}$$

$$\overline{k_N^2}(k_{\bar{K}}, k) = \begin{cases} \xi^2 k_{\bar{K}}^2 + (1+\xi)^2 k^2 - \dfrac{[\xi k_{\bar{K}} + (1+\xi)k]^2 - k_F^2}{2} & \text{for } \frac{|k_F - \xi k_{\bar{K}}|}{1+\xi} \le k \le \frac{k_F + \xi k_{\bar{K}}}{1+\xi}, \\ \xi^2 k_{\bar{K}}^2 + (1+\xi)^2 k^2 & \text{for } k \le \frac{k_F - \xi k_{\bar{K}}}{1+\xi} \end{cases} \tag{D.6}$$

Bibliography

[Ahl90s] L. Ahle et al., (E802 Collaboration) Phys. Rev. C58 (1998) 3523; Phys. Rev. C60 (1999) 0044904; (E866/E917 Collaboration), Phys. Lett. B476 (2000) 1; Phys. Lett. B490 (2000) 53.

[Ahn97] W. Ahner et al, Phys. Lett. B31 (1997) 393.

[Aka02] Y. Akaishi, and T. Yamazaki, Phys. Rev. C65 (2002) 044005.

[Alb76] M. Alberg, E. M. Henley, and L. Wilets, Ann. Phys. 96 (1976) 43.

[Bac00] A. Baca, C. García-Recio, and J. Nieves, Nucl. Phys. A673 (2000) 335.

[Bal97] S. Balberg, and A. Gal, Nucl. Phys. A625 (1997) 435.

[Bar99] S. Bart et al., Phys. Rev. Lett. 83 (1999) 5238.

[Ber95] V. Bernard, N. Kaiser, and U. G. Meissner, Int. J. Mod. Phys. E4 (1995) 193.

[Bes97] D. Best et al., Nucl. Phys. A625 (1997) 307.

[Bra00] E. L. Bratkovskaya, W. Cassing, C. Greiner, M. Effenberger, U. Mosel, and A. Sibirtsev, Nucl. Phys. A675 (2000) 661.

[Bra97] E.L. Bratkovskaya, W. Cassing, and U. Mosel, Nucl. Phys. A622 (1997) 593.

[Bro01a] G. E. Brown, M. Rho, and C. Song, Nucl. Phys. A690 (2001) 184c.

[Bro01b] G. E. Brown, M. Rho, and C. Song, Nucl. Phys. A698 (2002) 483c.

[Bro02] G. E. Brown, and M. Rho, Phys. Rep. 363 (2002) 85.

[Bro94] G. E. Brown, and H. A. Bethe, Astrophys. Jour. 423 (1994) 659; Nucl. Phys. A567 (1994) 937.

[Brw84] H. H. Brouwer, J. W. de Maag, and L. P. Kok, Z. Phys. A318 (1984) 199.

[Bru50s] K. A. Brueckner, Phys. Rev. 96 (1954) 508; K. A. Brueckner, and C. A. Levinson, Phys. Rev. 97 (1955) 1344; K. A. Brueckner, Phys. Rev. 97 (1955) 1353; K. A. Brueckner, C. A. Levinson, and H. M. Mahmoud, Phys. Rev. 95 (1957) 217.

[But90] R. Büttgen, K. Holinde, A. Müller-Groeling, J. Speth, and P. Wyborny, Nucl. Phys. A506 (1990) 586.

[Cab01] D. Cabrera , *El mesón rho en el medio nuclear - una descripción en el marco de la Teoría Quiral Unitaria*-; Trabajo de Investigación, September 2001.

[Car00] J. Caro-Ramon, N. Kaiser, S. Wetzel, and W. Weise, Nucl. Phys. A672 (2000) 249.

[Cas03] W. Cassing, L.Tolós, E. Bratkovskaya, A. Ramos, and A. Polls, submitted to Nucl. Phys. A.

[Cas97] W. Cassing, E.L. Bratkovskaya, U. Mosel, S. Teis, and A. Sibirtsev, Nucl. Phys. A614 (1997) 415.

[Cas99] W. Cassing, and E. Bratkovskaya, Phys. Rep. 308 (1999) 65.

[Cib82] J. Ciborowski et al., J. Phys. G8 (1982) 13.

[Cie01] A. Cieplý, E. Friedman, A. Gal, and J. Mareš, Nucl. Phys. A696 (2001) 173.

[Cle00] J. Cleymans, H. Oeschler, and K. Redlich, Phys. Lett. 485 (2000) 27.

[Cle98a] J. Cleymans, and K. Redlich, Phys. Rev. Lett. 81 (1998) 5284.

[Cle98b] J. Cleymans, D. Elliot, A. Keränen, and E. Suhonen, Phys. Rev. C57 (1998) 3319.

[Cle99a] J. Cleymans, and H. Oeschler, J. Phys. G25 (1999) 281.

[Cle99b] J. Cleymans, H. Oeschler, and K. Redlich, Phys. Rev. C59 (1999) 1663.

[Cle99c] J. Cleymans, and K. Redlich, Phys. Rev. C60 (1999) 054908.

[Cro00] P. Crochet et al., Phys. Lett. B486 (2000) 6.

[Dal82] R. H. Dalitz, J. McGinley, C. Belyea and S. Anthony, *Proc. Int. Conf. on hypernuclear and kaon physics*, (Heidelberg, 1982) 201.

[Daw99] J. Dabrowski, Phys. Rev. C60 (1999) 025205.

[Day67] B. D. Day, Rev. Mod. Phys. 39 (1967) 719.

[Dov71] C. B. Dover, J. Hüfner, and R. H. Lemmer, Ann. Phys. 66 (1971) 248.

[Dun00] J. C. Dunlop, and C. A. Ogilvie, Phys. Rev. C61, (2000) 031901 and references therein; J. C. Dunlop, Ph.D. Thesis, MIT, 1999.

[Eck95] G. Ecker, Prog. Part. Nucl. Phys. 35 (1995) 1.

[Eff99] M. Effenberger, E. L. Bratkovskaya, W. Cassing, and U. Mosel, Phys. Rev. C60 (1999) 027601.

[Eri88] T. E. Ericson, and W. Weise, *The International Series of Monographs on Physics*, 74 (Clarendon, Oxford, UK, 1988), 479p.

[Eva83] D. Evans et al., J. Phys. G9 (1983) 885.

[Exp00s] See state-of-the-art experimental information on the web sites: `www.gsi.de, www.cern.ch, www.bnl.gov/rhic`.

[Fet71] A. L. Fetter, and J. D. Walecka, *Quantum Theory of Many-Particle Systems* (International Series in Pure and Applied Physics, Mc Graw-Hill, NY, USA, 1971).

[Fla76] S. M. Flatté, Phys. Lett. B63 (1976) 224.

[For02] A. Förster, Ph.D. Thesis in preparation, TU Darmstad.

[Fri94] E. Friedman, A. Gal, and C.J. Batty, Nucl. Phys. A579 (1994) 518.

[Fri99a] E. Friedman, A. Gal, J. Mareš, and A. Cieplý, Phys. Rev. C60 (1999) 024314.

[Fri99b] E. Friedman, and A. Gal, Phys. Lett. B459 (1999) 43.

[Fuc01] C. Fuchs, A. Faessler, E. Zabrodin, and Y. M. Zheng, Phys. Rev. Lett. 86 (2001) 1974.

[Gar02] C. García-Recio, A. J. Melgarejo, and J. Nieves, nucl-th/0210030, Phys. Rev. C in print.

[Gar03] C. García-Recio, J. Nieves, E. Ruiz Arriola, and M. J. Vicente-Vacas, hep-ph/0210311, Phys. Rev. D in print.

[Gas85] J. Gasser, and H. Leutwyler, Nucl. Phys. B250 (1985) 465.

[Gol57] J. Goldstone, Proc. Roy. Soc. A239 (London, 1957) 267.

[Hag85] R. Hagedorn, and K. Redlich, Z. Phys C27 (1985) 541.

[Har01] J. Harris, (STAR Collaboration), Nucl. Phys. A698 (2001) 64.

[Har03] C. Hartnack, H. Oeschler, and J. Aichelin, nucl-th/0109016, Phys. Rev. Lett. in print.

[Har98] C. Hartnack et al., Eur. Phys. J. A1 (1998) 151.

[Hei00] H. Heiselberg, and M. Hjorth-Jensen, Phys. Rep. 328 (2000) 237.

[Hem85] R. J. Hemingway, Nucl. Phys. B253 (1985) 742.

[Hen80] E. M. Henley, M. A. Alberg, and L. Wilets, Nukleonika 25 (1980) 567.

[Hir00] S. Hirenzaki, Y. Okumura, H. Toki, E. Oset, and A. Ramos, Phys. Rev. C61 (2000) 055205.

[Huf72] J. Hüfner, and C. Mahaux, Ann. Phys. 73 (1972) 525.

[Huf75] J. Hüfner, Phys. Rep. 21 (1975) 1.

[Hum62] W. E. Humphrey, and R. R. Ross, Phys. Rev. 127 (1962) 1305.

[Itz80] C. Itzykson and J. B. Zuber, *Quantum Field Theory* (Mc Graw-Hill, New York, 1980).

[Jid02] D. Jido, E. Oset, and A. Ramos, Phys. Rev. C66 (2002) 055203.

[Joa75] C. J. Joachain, *Quantum Collision Theory* (Elsevier Science Publishers B. V., North Holland, Netherlands, 1975).

[Kai95] N. Kaiser, P. B. Siegel, and W. Weise, Nucl. Phys. A594 (1995) 325.

[Kai97] N. Kaiser, T. Waas, and W. Weise, Nucl. Phys. A612 (1997) 297.

[Kao90s] R. Barth et al., Phys. Rev. Lett. 78 (1997) 4007; F. Laue et al., Phys. Rev. Lett. 82 (1999) 1640.

[Kap86] D. B. Kaplan, and A.E. Nelson, Phys. Lett. B175 (1986) 57; *ibid.* B179 (1986) 409(E).

[Kim65] J. K. Kim, Phys. Rev. Lett. 14 (1965) 29.

[Kim66] J. K. Kim, Columbia University Report, Nevis 149 (1966).

[Kit66] W. Kittel, G. Otter, and I. Wacek, Phys. Lett. 21 (1966) 349.

[Ko87] C. M. Ko, Q. Li, and R. Wang, Phys. Rev. Lett. 59 (1987) 1084.

[Koc86] P. Koch, B. Müller, and J. Rafelski, Phys. Rep. 142 (1986) 167.

[Koc94] V. Koch, Phys. Lett. B337 (1994) 7.

[Kol02] E. E. Kolomeitsev, and D. N. Voskresensky, nucl-th/0211052.

[Kub96] K. Kubota et al., Nucl. Phys. A602 (1996) 327.

[Lee94] C. -H. Lee, G. E. Brown, and M. Rho, Phys. Lett. B335 (1994) 266.

[Lee95] C. -H. Lee, G. E. Brown, D. P. Min, and M. Rho, Nucl. Phys. A585 (1995) 401.

[Lee96] C.-H. Lee, Phys. Rep. 275 (1996) 255.

[Lee98] T. S. H. Lee, J. A. Oller, E. Oset, and A. Ramos, Nucl. Phys. A643 (1998) 402.

[Li97] G.Q. Li, C.-H. Lee, and G.Brown, Nucl. Phys. A625 (1997) 372; *ibid*, Phys. Rev. Lett. 79 (1997) 5214.

[Li98] G.Q. Li, and G.Brown, Phys. Rev. C58 (1998) 1698.

[Lut02a] M. Lutz, and E. E. Kolomeitsev, Nucl. Phys. A700 (2002) 193.

[Lut02b] M. F. M. Lutz, and C. L. Korpa, Nucl. Phys. A700 (2002) 309.

[Lut98a] M. Lutz, Phys. Lett. B426 (1998) 12.

[Lut98b] M. F. M. Lutz, nucl-th/9802033. Talk dedicated to M.Rho on the occasion of his 60th birthday.

[Mac87] R. Machleidt, K. Holinde, and Ch. Elster, Phys. Rep. 149 (1987) 1.

[Mac89] R. Machleidt, Adv. Nucl. Phys. 19 (1989) 189.

[Man84] F. Mandl, and G. Shaw, *Quantum Field Theory* (John Wiley and Sons Ltd, Great Britain, 1984).

[Mao99] G. Mao, P. Papazoglou, S. Hofmann, S. Schramm, H. Stöcker, and W. Greiner, Phys. Rev. C59 (1999) 3381.

[Mar69] B. Martin, and M. Sakitt, Phys. Rev. 183 (1969) 1345.

[Mar76] A. D. Martin, Phys. Lett. B65 (1976) 346.

[Mar81] A. D. Martin, Nucl. Phys. B179 (1981) 33.

[Mar95] J. Mareš, E. Friedman, A. Gal, and B. K. Jennings, Nucl. Phys. A594 (1995) 311.

[Mei89] O. Meirav, E. Friedman, R. R. Johnson, R. Olszewski, and P. Weber, Phys. Rev. C40 (1989) 1843.

[Mei93] U. G. Meissner, Rep. Prog. Phys. 56 (1993) 903.

[Men00] M. Menzel et al., Phys. Lett. B495 (2000) 26; Ph.D. Thesis, Universität Marburg, 2000.

[Mis94] D. Miśkowiec et al, Phys. Rev. Lett. 72, (1994) 3650.

[Mos99] U. Mosel, Prog. Part. Nucl. Phys. 42 (1999) 163.

[Mui65] H. Muirhead, *The physics of elementary particles* (Pergamon Press, Oxford, 1965).

[Mul85] B. Müller, *The Physics of the Quark-Gluon Plasma*, Lecture Notes in Physics Vol. 225 (Springer-Verlag, Berlin, 1985), pp. 91-104.

[Mul90] A. Müller-Groeling, K. Holinde, and J. Speth, Nucl. Phys. A513 (1990) 557.

[Nag73] M. M. Nagels, Th. A. Rijken, and J. J. de Swart, Phys. Rev. Lett. 31 (1973) 569.

[Now78] R. J. Nowak et al., Nucl. Phys. B139 (1978) 61.

[Oes02] H. Oeschler, J. Phys. G28 (2002) 1787.

[Ogi01] C. A. Ogilvie, Nucl. Phys. A698 (2001) 39.

[Ohn97] A. Ohnishi, Y. Nara, and V. Koch, Phys. Rev. C56 (1997) 2767.

[Oll01] J. A. Oller, and U. Meissner, Phys. Lett. B500 (2001) 263.

[Ose01] E. Oset, and A. Ramos, Nucl. Phys. A679 (2001) 616.

[Ose82a] E. Oset, H. Toki, and W. Weise, Phys. Rep. 83 (1982) 28.

[Ose82b] E. Oset, *Proceedings: Quarks, Mesons and Isobars in Nuclei*, Motril (1982) 1-60.

[Ose90] E. Oset, P. Fernández de Córdoba, L.L. Salcedo, and R. Brockmann, Phys. Rep. 188 (1990) 79.

[Ose98] E. Oset, and A. Ramos, Nucl. Phys A635 (1998) 99.

[Pic95] A. Pich, Rep. Prog. Phys. 58 (1995) 563.

[Raj60s] R. Rajamaran, Phys. Rev. 131 (1963) 1244; H. A. Bethe, Phys. Rev. 138 (1965) B804; R. Rajamaran, and H. A. Bethe, Rev. Mod. Phys. 39 (1967) 745.

[Ram00] A. Ramos, and E. Oset, Nucl. Phys. A671 (2000) 481.

[Ram01a] A. Ramos, S. Hirenzaki, S.S. Kamalov, T.T.S. Kuo, Y. Okumura, E. Oset, A. Polls, H. Toki, and L. Tolós, Nucl. Phys. A691 (2001) 258c.

[Ram01b] A. Ramos, J. Schaffner-Bielich, and J. Wambach in *Physics of Neutron Star Interiors*, edited by D. Blaschke, N. K. Glendenning, and A. Sedrakian, Lecture Notes in Physics Vol. 578, (Springer,New York, 2001), p.175 and references therein.

[Ram94] A. Ramos, E. Oset, and L.L. Salcedo, Phys. Rev. C50 (1994) 2314.

[Red80s] K. Redlich and L.Turko, Z. Phys. C5 (1980) 201; L. Turko, Phys. Lett. B104 (1981) 361.

[Rit95] J. Ritman et al., Z. Phys. A352 (1995) 355.

[Sak65] M. Sakitt et al., Phys. Rev. B139 (1965) 719.

[Scha00] J. Schaffner-Bielich, V.Koch, and M. Effenberg, Nucl. Phys. A669 (2000) 153.

[Scha97] J. Schaffner-Bielich, I. N. Mishustin, and J. Bondorf, Nucl. Phys. A625 (1997) 325.

[Sch87] J. Schnick, and R. H. Landau, Phys. Rev. Lett. 58 (1987) 1719.

[Sek83] R. Seki and K. Masutani, Phys. Rev. C27 (1983) 2799.

[Sen01] P. Senger, Acta Phys. Polon. B31 (2000) 2313; Nucl. Phys. A685 (2001) 312.

[Ser86] B.D. Serot, and J.D. Walecka, Adv. Nucl. Phys. 16 (Plenum Press, New York, 1986).

[Shi98] Y. Shin et al, Phys. Rev. Lett. 81 (1998) 1576.

[Sib98] A. Sibirtsev, and W. Cassing, Nucl. Phys. A641 (1998) 476.

[Sie88] P. B. Siegel, and W. Weise, Phys. Rev. C38 (1988) 2221.

[Sta87] L. R. Staronski, and S. Wycech, J. Phys. G13 (1987) 1361.

[Stu01] C. Sturm et al., Phys. Rev. Lett. 86 (2001) 39.

[Stu02] C. Sturm et al., J. Phys. G28 (2002) 1895.

[Tam89] H. Tamura et al., Phys Rev. C40 (1989) R479.

[Tei97] S. Teis, W. Cassing, M. Effenberger, A. Hombach, U. Mosel, and G. Wolf, Z. Phys. A356 (1997) 421.

[Tho73] D. W. Thomas, A. Engler, H. E. Fisk, and R. W. Kraemer, Nucl. Phys. B56 (1973) 15.

[Tol01a] L. Tolós, A. Ramos, A. Polls, and T.T.S. Kuo, Nucl. Phys. A690 (2001) 547.

[Tol01b] L. Tolós, A. Polls, A. Ramos in *Proceedings of Mesons and Light Nuclei*, Prague, Czech Republic, July 2001. Published in Prague 2001, Mesons and Light Nuclei, 485-488.

[Tol02] L. Tolós, A. Ramos, and A. Polls, Phys. Rev. C65 (2002) 054907.

[Tol03] L. Tolós, A. Polls, A. Ramos, and J.Schaffner-Bielich, nucl-th/0302082, submitted to Phys. Rev. C.

[Tov71] D. N. Tovee et al., Nucl. Phys. B33 (1971) 493.

[Tsu98] K. Tsushima, K. Saito, A. W. Thomas, and S. V. Wright, Phys. Lett. B 429 (1998) 239.

[Vid00] I. Vidaña, *Description of hyperonic matter and hypernuclei within the Brueckner-Hartree-Fock theory*; Ph.D Thesis, Barcelona, 2001.

[Waa96a] T. Waas, N. Kaiser, and W. Weise, Phys. Lett. B365 (1996) 12.

[Waa96b] T. Waas, N. Kaiser, and W. Weise, Phys. Lett. B379 (1996) 34.

[Waa97] T. Waas, and W. Weise, Nucl. Phys. A625 (1997) 287.

[Wam02] J. Wambach, Nucl. Phys. A699 (2002) 10.

[Wir88] R. Wiringa, Phys. Rev. C38 (1988) 2967.